Methods for Characterizing Multiphase Magnetocaloric Materials

PhD Thesis

Programa de Doctorado en Ciencia y Tecnología de Nuevos Materiales

Álvaro Díaz García

Supervisors:

Prof. Victorino Franco García

Dr. Jia Yan Law

Departamento de Física de la Materia Condensada

Facultad de Física, Universidad de Sevilla

To my parents, sister, brother, and especially to Loli

Acknowledgements

A mis directores de tesis Victorino y Jia Yan por todo su esfuerzo y por la confianza puesta en mí. Me siento muy afortunado de haber podido aprender tanto de ellos durante la tesis y de poder seguir haciéndolo.

A cada uno de los miembros del grupo de Sólidos no Cristalinos de la Universidad de Sevilla. A los miembros seniors del grupo por su ayuda y sus consejos. A cada uno de los estudiantes con los que he coincidido, por su compañerismo y los buenos momentos tanto en la facultad como fuera de ella. Agradecer en especial a Luis por su ayuda y por las colaboraciones realizadas.

To the group of Magnetic Microstructures of IFW-Dresden for their hospitality, making me feel like one of the group from the first moment. To Prof. Schäfer, head of the group, for his help from the preparation of the research proposal to the last moment in Dresden. To the German Academic Exchange Service (DAAD) that financed my research stay in Germany through the Short-Term Grants program.

A mi familia y amigos por su apoyo y cariño. A mis padres Joaquín y Elena y hermanos Elena y Joaquín por lo mucho que me han ayudado en esta etapa. Quiero agradecer especialmente a Loli por su amor, apoyo y sacrificio.

A las diferentes entidades públicas y privadas que han hecho posible la realización de esta tesis a través de diferentes contratos: FEDER 2014-2020 y Consejería de Economía y Conocimiento de la Junta de Andalucía (US-1260179), and Plan Andaluz de Investigación, Desarrollo e Innovación (P18-RT-746), US Army Research Laboratory (W911NF-19–2–0212), ArcelorMittal y ThyssenKrupp con proyectos industriales a través de FIUS.

Contents

Abstract

This thesis is aimed to study the characteristics of thermomagnetic phase transitions and the resulting magnetocaloric effect in multiphase magnetocaloric materials, which is a very common scenario in the research of the magnetocaloric effect and can lead to complex situations that need to be properly approached.

On the one hand, composites that combine various phases with Curie transitions close to each other are interesting and highly studied as they can lead to an enhanced refrigerant capacity with respect to the pure phases while keeping a large enough response. In this thesis, newly developed Gd + Gd_7Pd_3 composites are presented as a case in which the mentioned improvement of the refrigerant capacity is achieved. This intentional situation of overlapping Curie transitions has been used for the development of a method for the deconvolution of the magnetocaloric responses by means of the scaling laws of the magnetocaloric effect. On the other hand, materials exhibiting magnetostructural transformation (first-order phase transition) can also show the Curie transitions of the phases (second-order phase transition), where the phase transitions of different type can be concurrent. This situation is approached using Heusler alloys undergoing magnetostructural transformation located close to the Curie transitions of the martensitic and austenitic phases. The competing effect of both types of phase transitions in this case is investigated by experimental and analytical methods. The deconvolution method used for the composites is successfully applied here, enabling the subtraction of the Curie transition to the total response. It has to be noted that these situations of overlapping phase transitions can also occur unintentionally (i.e., due to the presence of impurities during synthesis). Therefore, the developed methods can also be used in these situations to know the effect of additional phase transitions and to gauge the actual response of the desired phase.

Additionally, it has also been shown how the overlapping Curie transitions of the phases affect the hysteretic signature of the alloys undergoing magnetostructural transformation. This study is addressed through the emerging Temperature first-order reversal curves (TFORC) method for the study of magnetocaloric materials, using again Heusler alloys as a model case. This part combines experimental results with results from the modelling of the thermomagnetic behavior of the material. This has enabled a direct correlation between the characteristics of the thermomagnetic behavior of the alloys and the features of the TFORC distributions.

Finally, the emerging topic of using polymer-based composites for the 3D printing of functional parts is addressed. Here, the main existing problem lies in the fabrication of uniform composite materials that allow the 3D printing of parts with predictable and repeatable functionality without relying on industrial techniques. A novel manufacturing method of polymer-based filaments containing functional fillers is proposed. Soft-magnetic steel particles have been used to manufacture polymer-based magnetic composites as proof of concept of the validity of the method. Once validated, the method is used to manufacture polymer-based magnetocaloric composites for additive manufacturing. The relatively simple method provides highly homogeneous filaments that preserve the magnetic functionality of the fillers. However, the property of the polymeric matrix is significantly affected by the addition of the metallic fillers, which has an important influence on the processability parameters both for the extrusion and printing.

Nomenclature

Acronyms

AM	Additive manufacturing
BSE	Backscatter electrons
DSC	Differential scanning calorimetry
EDX	Energy dispersive X-rays
EIA	U.S. Energy Information Administration.
FDM	Fused deposition modeling
FFF	Fused filament fabrication
FOPT	First-order phase transition
FORC	First-order reversal curves
FWHM	Full width at half maximum
LVR	Linear viscoelastic region
MCE	Magnetocaloric effect
MOKE	Magneto-optical Kerr effect
MSM	Magnetic shape memory
PLA	Polylactic acid
RE	Rare-earth
SAOS	Small amplitude oscillatory shear
SEM	Scanning electron microscopy
SOPT	Second-order phase transition
TFORC	Temperature first-order reversal curves
TGA	Thermogravimetric analysis
VSM	Vibrating sample magnetometer
XRD	X-ray diffraction

Symbols

a, b	Parameters for the Arrott-Noakes equation of state
α	Skewness factor

β, γ	Critical exponents for the Arrott-Noakes equation of state
$\dot{\gamma}$	(Shear rheology) Shear rate
$c_{p,H}$	Specific heat at constant pressure and field
C_p	Heat capacity at constant pressure
d	Mean particle diameter
d_{hkl}	Spacing of the {hkl} planes of a crystal
$\Delta H_{cc}, \Delta H_m$	Enthalpies related to the cold crystallization and melting of a polymer
ΔS_{iso}	Isothermal entropy change per unit mass
ΔS_{iso}^{dec}	Deconvoluted ΔS_{iso}
ΔS_{iso}^{pk}	Peak value of ΔS_{iso}
ΔT_{ad}	Adiabatic temperature change
ΔT_{hys}	Thermal hysteresis
erf	Error function
ϵ	(Shear rheology) Applied oscillatory stress
e/a	Electron per atom ratio
f_m	Mass fraction
f_{Aus}, f_{Mar}	Austenite and martensite fractions
g	Landé constant
h	(Shear rheology) Gap between the parallel plates
H	H-magnetic field
H_c, H_u	Transformed H-magnetic field for FORC distribution
H_r	Reversal H-magnetic field for FORC
H_{sat}	Saturation H-magnetic field
J	Total moment quantum number
k_B	Boltzmann constant
M	Magnetization per unit mass
M_S	Saturation M
M_{ext}^C, M_{ext}^H	Extended M for cooling and heating TFORC
$M_{T,T_r}, M_{T_r,T}$	Reconstructed M from TFORC distributions
λ_w	X-ray beam wavelength
λ	Exchange constant
μ_0	Magnetic permeability of vacuum
μ_B	Bohr magneton
n	Exponent of the power dependence of ΔS_{iso} with field
ξ	Location of the modeled martensitic transformation
O_T	Owen's T function

P	Pressure
RC	Refrigerant capacity
RCP	Relative cooling power
ρ	FORC distribution
η, η^*	Apparent and complex viscosities
η', η''	Real and imaginary components of complex viscosity
S	Surface
σ	(Shear rheology) Oscillatory strain
σ	Scale of the normal distribution
t	Time
T	Temperature
T_C	Curie temperature
T_{cc}	Cold crystallization temperature of a polymer
T_{center}	Central temperature of the TFORC distributions
T_g	Glass transition temperature
T_h, T_u	Transformed temperatures for TFORC distributions
T_m	Melting temperature
T_M	Temperature of the martensitic transformation
T_{pk}	Peak temperature
T_r	(TFORC) Reversal temperature
T_r	(Universal scaling) Reference temperature
T_{sat}^C, T_{sat}^H	Saturation temperatures for cooling and heating TFORC
θ	(Universal scaling) Rescaled temperature axis
θ	Half angle between incident and diffracted X-rays
v	(Shear rheology) Velocity of the moving plate
V	Volume
χ	Susceptibility
χ', χ''	Real and imaginary components of AC susceptibility
χ_c	Degree of crystallinity of a polymer
ω	Angular frequency

1 Introduction

New energy efficient and environmentally friendly technologies can help to rectify the global energy wastage and to mitigate current environmental issues. In this sense, the magnetocaloric effect receives high attention as it can be used as working mechanism of magnetic refrigerators, which are more energy efficient than the conventional ones based on gas compression/expansion. This effect is referred as the temperature change that a magnetic material experiences when magnetized and demagnetized in the vicinity of a thermomagnetic phase transition. This chapter introduces the basic concepts that will be necessary to set up the research carried out. As the research is focused on the study of multiphase magnetocaloric materials, the concept of magnetocaloric effect and thermomagnetic phase transitions are introduced first. Materials in this thesis have been chosen mainly to correspond to appropriate model cases for the application of the developed methods while being considered state-of-the-art materials. Therefore, a current view of the different trends regarding magnetocaloric materials is included, that serves to put in context those that have been used for the studies. In addition, the upcoming additive manufacturing is briefly introduced, focusing on the use of polymer-based composites for being a promising method for producing magnetocaloric materials in the e complex shapes that optimize their functionality.

1.1 Magnetocaloric effect

The magnetocaloric effect (MCE) is defined as the reversible adiabatic temperature change (or isothermal entropy change) that a magnetic material exhibit when adiabatically (or isothermally) magnetized and demagnetized [1–5]. This effect allows for the development of magnetic refrigerators with a relevant energy efficiency improvement with respect to the conventional ones based on gas compression/expansion [6,7]. The best commercial conventional refrigerator has an energy efficiency of 40 % of the Carnot cycle while magnetic refrigerator prototypes can reach 60 % [4], indicating an improvement of 50 %. This technological possibility, motivated by the urgent need to reduce energy consumption, has given a great attention to the MCE topic in the recent years.

Nowadays, our daily livelihood and industries are highly dependent on electricity, in which the global raise in consumption evolves faster than world population, according to the data collected from U.S. Energy Information Administration (EIA) [8]. The estimated U.S energy consumption reported by Lawrence Livermore National Laboratory reveals that in 2020, 35.6 % of the total energy was used for electricity production, an amount which surpasses that used directly for any other destination (e.g., 24.3 % for transportation and 22.1 % for industry). A similar observation is found in the report for Spain in 2017, in which 37 % of the total energy was destinated to the electricity production [9]. Looking in detail, it is evident that a high percentage of electricity is used for refrigeration and space conditioning since our way of living is largely dependent on refrigerating food and regulating the temperature of the residential and working environments. Recent reports of the EIA estimate that around 75 % of the electricity in 2018 of USA was distributed almost equally between the residential and commercial sectors. In the residential sector, 22 % of the electricity consumption was due to the space cooling and refrigeration, whereas 25.8 % was destinated to these uses in the commercial sector [10]. In addition, the capabilities of gas liquefaction have experienced an increasing demand in every sector, with the main representative of the natural gas liquefaction, that also requires refrigeration mechanisms [11,12].

Therefore, more efficient alternatives to the conventional refrigeration methods, especially those working in the vicinity of room temperature, will lead to remarkable energy savings. Magnetic refrigeration offers great benefits in favor of a more sustainable world because it does not need large compressor and refrigerant gases that affect the ozone layer (such as CFCs) as well as those related to the greenhouse effect (e.g., NH_3, HCFCs or HFCs). The MCE also receives attention for medical applications [13,14] and as mechanism for power generation and energy harvesting [15,16].

The characterization of the MCE involves obtaining the adiabatic temperature change, ΔT_{ad}, and/or the isothermal entropy change, ΔS_{iso}, of a material upon its magnetization and demagnetization. These two magnitudes are introduced analytically by applying the principle of energy conservation (first principle of the thermodynamics) to a material undergoing a magnetic work. The final expressions for ΔT_{ad} and ΔS_{iso} are known as the Maxwell relations and they are given by [4]:

$$\Delta T_{ad} = -\mu_0 \int_{H_{initial}}^{H_{final}} \frac{T}{c_{p,H}} \left(\frac{\partial M}{\partial T}\right) \mathrm{d}H, \tag{1.1}$$

and

$$\Delta S_{iso} = \mu_0 \int_{H_{initial}}^{H_{final}} \left(\frac{\partial M}{\partial T}\right)_H \mathrm{d}H, \tag{1.2}$$

where μ_0 is the permeability of the free space, T is temperature, M magnetization per unit mass, H is the magnetic field, and $c_{p,H}$ is the specific heat at constant pressure and field. These equations manifest that the MCE is strongly correlated to magnetization changes with temperature, i.e., $\partial M/\partial T$. This condition can be satisfied in materials by the presence of thermomagnetic phase transitions in the temperature region of interest.

The data regarding the ΔT_{ad} would offer the definitive information to evaluate the performance of a magnetocaloric material in a refrigeration device. However, it is more straightforward to obtain ΔS_{iso} as it can be indirectly determined from **Equation (1.2)** by appropriate measurement of the temperature and field dependence of M, that can be performed in conventional magnetometers. The indirect determination of ΔT_{ad} from

Equation (1.1) requires the additional characterization of the temperature and field dependence of $c_{p,H}$ which involves long measurement time and usually specialized calorimeters. In the same way, the direct measurement of ΔT_{ad} requires the use of additional equipment, apart from magnetometers, which has to be custom-made due to the very specific characteristics of the measurements [17].

The trend of using ΔS_{iso} to characterize the MCE has led to the definition of other figures of merit that relate the performance that a magnetocaloric material would have in a refrigeration device through the knowledge of ΔS_{iso}. The most common one is the refrigerant capacity (*RC*) (also known as relative cooling power, *RCP*), which is the amount of heat that can be transferred between the hot and cold reservoirs with temperatures T_{hot} and T_{cold}, respectively [18]:

$$RC(H) = \mu_0 \int_{T_{cold}}^{T_{hot}} \Delta S_{iso}(T,H)\, \mathrm{d}T. \tag{1.3}$$

This equation admits different approximations, among which the typical consists of considering that the temperature span between the reservoirs is the full width at half maximum (FWHM) of the peak. Then, RC_{FWHM} is calculated as the product of the peak of the entropy change, ΔS_{iso}^{pk}, times FWHM, δT_{FWHM}.

The approach taken in this thesis goes beyond material development and characterization, being the goal different from proposing new magnetocaloric materials as potential candidates for a final application. In this sense, the exclusive use of ΔS_{iso} in this thesis is justified as there are preexisting analysis methods based on it (described in **Chapter 2**) which will serve as starting point for the new ones proposed. Additionally, the extensive character of ΔS_{iso}, unlike ΔT_{ad}, enables to separate the contributions of different magnetocaloric phases.

1.2 Thermomagnetic phase transitions and magnetocaloric materials

The application of the MCE as refrigeration mechanism started in the forties with the attainment of ultralow temperatures by the demagnetization of paramagnetic salts as they exhibit a significant temperature dependence of magnetization near 0 K [19,20].

For magnetic materials to meet the condition of having a significant $\partial M/\partial T$ at any temperature different from the vicinity of absolute zero, the presence of thermomagnetic phase transitions is required. Phase transitions in magnetic materials can be classified according to the Ehrenfest classification [21], i.e., first-order phase transition (FOPT) or second-order phase transition (SOPT). The classification of magnetocaloric materials according to the order of the main thermomagnetic phase transition that they undergo is especially convenient as FOPTs and SOPTs produce magnetocaloric responses of well distinguishable features. In a magnetic FOPT, M shows an abrupt change at the transition temperature. FOPTs involve latent heat, and they show phase coexistence and hysteresis phenomena. On the other hand, M shows a continuous change in SOPTs and thus they are also known as continuous phase transitions. SOPTs do not involve latent heat but just a change of the heat capacity and they do not present hysteresis. For FOPT magnetocaloric materials, their reports are usually with very large MCE due to abrupt magnetization changes that occur in a narrow temperature span accompanied by thermal hysteresis. On the other hand, SOPT magnetocaloric materials show MCE with lower values than those of FOPT candidates in a wider temperature span without hysteresis.

The only pure element undergoing a thermomagnetic phase transition near room temperature is the lanthanide rare-earth (RE) metal Gd, whose Curie transition (SOPT) occurs at a Curie temperature of $T_C = 293\,\mathrm{K}$. This element has been considered as the benchmark magnetocaloric material [5,22,23] since its use in 1976 by G. V. Brown for the development of a magnetic refrigerator [24]. For a magnetic field change of 7 T, pure Gd shows a peak response of $\Delta S_{iso}^{pk} = -13.2\,\mathrm{J\,kg^{-1}\,K^{-1}}$ and $\Delta T_{ad}^{pk} = 14\,\mathrm{K}$ [24]. No other material undergoing SOPT has been found to surpass the response of Gd in the vicinity of room temperature due to the large saturation magnetic moment of 7.63 Bohr magnetons [22]. One widely used approach to improve the MCE performance of SOPT magnetocaloric materials in the community is to include several phases whereby their Curie transitions are appropriately arranged to widen the temperature span and thus increases their RC and RCP [25–28]. Although large refrigerant capacity values are attained, these multiphasic materials will require to maintain an order of magnitude of $\Delta T_{ad}^{pk} > 1\ \mathrm{K}$ for Ericsson refrigeration cycles [25,29].

One of the milestones in MCE was the discovery of giant MCE of $Gd_5(Si_2Ge_2)$ system close to room temperature by V.K. Pecharsky and K.A. Gschneidner in 1997 [30]. The alloy undergoes a thermomagnetic FOPT at 276 K upon heating, transforming from ferromagnetic orthorhombic Sm_5Ge_4-type to ferromagnetic monoclinic $Gd_5(Si_2Ge_2)$ structure of lower magnetization. Despite a lower saturation magnetization than that of Gd, the abrupt magnetization change of $Gd_5(Si_2Ge_2)$ due to the FOPT makes its ΔS_{iso}^{pk} and ΔT_{ad}^{pk} 100 % and 30 % larger than those of Gd, respectively [30]. Since then, many efforts have been put in the development of other materials exhibiting thermomagnetic FOPT. Several other FOPT magnetocaloric materials have been developed, including: Heusler alloys [31–33], $La(Fe,Si)_{13}$ [34], MnFeP(As,Ge,Si) [35], MnTX systems (T = Ni, Co, and X = Si, Ge, Ga) [36,37], or, more recently, high-entropy alloys [38,39].

Among the FOPT magnetocaloric materials, Heusler alloys are considered promising candidates for magnetic refrigeration as their large MCE values do not rely on compositions with critical or RE elements. They are magnetic intermetallic compounds with compositions XYZ (half-Heusler) and X_2YZ (full-Heusler), where X and Y are transition metals and Z is generally an element of the p-block. This type of compounds was discovered in 1903 by Friedrich Heusler, who found ferromagnetism in Cu_2MnAl alloy in which none of the constituents are ferromagnetic themselves. Off-stoichiometric compositions around the half- and full-Heusler stoichiometries are also referred as Heusler alloys. When the Y site is occupied by Mn in full- and off-stoichiometric full-Heusler alloys, the resulting compound is magnetic.

Off-stoichiometric full-Heusler alloys in the family of Ni-Mn-Z (Z = Ga, In, Sn, Sb) can show a giant MCE that arises from a magneto-structural transformation (martensitic type). These systems crystallize in the $L2_1$ cubic structure (austenitic phase), and the structural transformation takes place from the parent austenitic phase to a lower temperature martensitic phase with lower crystallographic symmetry (tetragonal $L1_0$) and lower magnetization. This martensitic transformation is complex and intermartensitic transformations may arise. Presence of modulated or distorted structures for the low temperature phase, such as 5M (or 10M) and 7M (or 14M), can also occur [5]. As the magnetization change due to the transformation has an opposite sign to that of a Curie transition, the resulting MCE is referred as inverse MCE. Therefore, the inverse MCE has an associated positive ΔS_{iso} and negative ΔT_{ad}. The temperature of the martensitic transformation is highly compositional dependent, whereby the phase transition diagrams are usually presented with the electron per atom ratio, e/a, accounting for the average number of electrons in the outer shell per atom. The Curie transition of the austenitic phase also produces a relevant MCE [40]. The temperature of this SOPT is less dependent on the composition, i.e., of the e/a ratio, and it is usually located close to the martensitic transformation.

The magnetostructural transformation in these systems can be driven by either temperature, magnetic field, and stress due to the coupling of the structural and magnetic degrees of freedom. This confers to the martensitic Heusler alloys the property of magnetic shape memory (MSM) effect. The MSM and related properties such as superelasticity, magnetostriction make these systems interesting for development of smart parts as sensors or actuators [41,42]. As the transition can be driven by mechanical stress, they also show elastocaloric and barocaloric effects so that they are candidates for multicaloric refrigeration devices [43–45].

Although these alloys show a large magnetocaloric response due to the FOPT, comparable or even higher than that of Gd at room temperature, the presence of thermal hysteresis is an important limitation for their performance under cyclic conditions [46]. It has been shown that the thermal hysteresis in these Heusler alloys is significantly reduced when moving through the martensitic transition by means of minor loops, i.e., avoiding the completion of the transformation [33,47,48]. However, a better understanding of the $M-T$ minor loops and the hysteresis mechanisms need further research.

The hysteresis can be significantly reduced or even made to vanish by reducing the volume change between the phases involved in a magnetic FOPT. Particularly, if both phases have the same crystallographic structure, the transition can become SOPT, and the hysteresis can be completely suppressed [46]. This may happen when the FOPT is due to a magnetoelastic transition as in the cases of La(Fe,Si)$_{13}$ and MnFeP(As,Ge,Si) systems. These two well studied families of compounds show a gradual change from FOPT to SOPT by compositional tuning or element doping. The composition that satisfies that the transition is right on the limit FOPT-SOPT is known as the tricritical composition [49]. The thermomagnetic transition in materials meeting the tricritical condition show characteristics of both FOPT and SOPT; a large MCE due to abrupt magnetization changes as in the case of FOPTs, with the absent of hysteresis as in SOPTs. Then, both La(Fe,Si)$_{13}$ and MnFeP(As,Ge,Si) systems have been proposed as good candidates for magnetic refrigeration. The case of La(Fe,Si)$_{13}$ has attracted a special attention as it does not incorporate any critical or dangerous element (such as As or P). For the application of La(Fe,Si)$_{13}$ compounds in room temperature magnetic refrigeration, the transition temperature, which is around 200 K, can be shifted to ambient temperature by hydrogenation while keeping the large MCE [50]. However, there are some important issues related to the poor mechanical resistance and material degradation under cyclic conditions of these compounds that have impeded its definitive and extended application in magnetic refrigeration [51].

The relevance of magnetocaloric materials exhibiting multiple phase transitions is justified either because of the relevant cases in which it appears intentionally (SOPT composites) or those in which it is consequence of the magnetostructural transformation undergone by the material ($Gd_5(Si_2Ge_2)$, Heusler alloys, etc.). Additionally, in any of the cases, the multiphase character can happen due to the presence of impurities, situation in which it is even more relevant to be able to discern which is the actual response of the desired phase. Motivated by this, one of the aims of this thesis is to develop methods to characterize the contributions arising from each of the phase transitions in multiphase transition magnetocaloric materials. For this purpose, Gd-based composites showing coexistent SOPT phases and Heusler alloys systems showing the coexistence of FOPT and SOPT have been used as model cases. For the former, an analysis tool for the study of overlapping SOPTs has been developed and applied to Gd-Pd composites with SOPTs with nearby T_C. This developed tool as well as other characterization and analysis protocols have been subsequently applied to the latter case, Heusler alloys, in which the contributions of their various phase transitions (FOPT+SOPT) overlap. The thermal hysteresis in FOPT materials has been considered taking a series of Heusler alloys as model case, showing that the presence of the overlapping SOPT of the phases, although non-hysteretic, produces effects on the hysteretic signature of the materials.

1.3 Additive manufacturing of functional parts

When employing magnetocaloric materials in prototypes or actual devices, their geometric designs have to be carefully considered for the optimization of the heat transfer between the solid refrigerant and fluid. For that, proposed designs consist of high surface to volume ratio geometries, ranging from packed particle beds to stricter geometrical constraints, such as parallel plates (thickness < 0.1 mm) with spacers for separation (~0.075 mm) [52] or microchannel geometries of various cross-sectional shapes (circular or square) along the fluid flow direction [53], etc. With such design constraints, it is challenging to shape magnetocaloric regenerators in their final forms using the traditional manufacturing processes, which are additionally accentuated given the intermetallic character of most of the relevant magnetocaloric materials, with their intrinsic hardness and brittleness.

In contrast to traditional manufacturing processes, based mainly on material removal (machining, carving, etc.), the different additive manufacturing (AM) (or 3D printing) technologies build objects through layer-by-layer deposition of material. Direct consequences of the AM approach are advantages such as material saving, the possibility of building complex structures with virtually no shape limitation, also avoiding the conventional expenses related to tooling and time. Nowadays, AM is a feasible alternative to traditional methods for the manufacturing of final parts using almost any type of material, from thermoplastics, metals or concrete, then applicable in almost every industrial and technological area [54–56]. Therefore, AM is a promising approach to manufacture magnetic and magnetocaloric parts as can overcome the issues related to the processability of these materials by the traditional methods.

Magnetic and magnetocaloric functional parts could be manufactured using some of the AM techniques that allow the direct 3D printing from raw metallic feedstock. Numerous metal AM technologies are currently available, being possible to find a diverse number of equipment depending on the energy/heat source (electron beam, laser, or arc), and how the metallic feedstock is supplied (powder bed systems, powder feed systems, or wire feed systems) [57,58]. All these processes have a common feature that is the raw metallic feedstock is melted to form the layers from which the 3D object will be built. These processes are well studied and optimized for a limited number of metallic alloys, including Ti and Ti-based alloy systems (e.g., Ti-6Al-4V, TiAl), steels, or Inconel. There are precedents of the use of these techniques with magnetocaloric alloys, however it is common to find a reduction in functionality after the 3D printing processes as the new melting can cause a variation of the initial composition or loss of the structural phase of the system, and this is crucial both in Ni_2Mn-based Heusler alloys [59–61] and in $La(Fe,Si)_{13}$ systems [62]. Additionally, in these two cases, the volume changes associated to the FOPT can compromise the reliability of the parts when subjected to repetitive thermal cycles and this issue cannot be overcome by these AM techniques.

The most accessible and extended AM technology is the fused deposition modeling (FDM), also known as fused filament fabrication (FFF). It is based on a melt extrusion technique where a polymer-based filament is fused and extruded through a moving nozzle (x- and y-axis movement) to be deposited in the form of a thin fiber. After every x-y layer, the z position of the platform is readjusted each time to build the object layer-by-layer. This technique is also a popular choice among the scientific community due to the possibility of using composite filaments (polymeric matrix with embedded functional particles) for the manufacture of functional parts [63–65]. Hence there are numerous studies aimed to manufacture functional composite filaments with different types of fillers to obtain additional properties, e.g., magnetic [66–69], electrical [70–72], optical [73,74], etc. Specific fillers, such as glass or carbon fibers, can also be used for the improvement of the mechanical strength of FDM parts [75,76]. The printing quality in FDM is highly dependent on the diameter uniformity of the filaments as the amount of material that is deposited with the extrusion of the filament should be precise. With the addition of a functional property to the filaments by the incorporation of fillers, it is also crucial that they are evenly distributed so that the functionality of the printed part is predictable and uniform. Hence, the main existing problem here lies in obtaining uniform composite filaments. The addition of fillers can significantly modify the properties of the polymer so that achieving a smooth extrusion with a good final shape uniformity can be challenging. A good dispersion of the particles is even more challenging, usually requiring multiple re-extrusion processes or turn to industrial facilities.

A novel manufacturing method has been developed to address the previously mentioned difficulties, allowing filaments with enhanced dimensional uniformity and good dispersion of the functional fillers to be obtained. The developed process has been validated using high performance soft magnetic steel as a proof-of-concept and extended to manufacture magnetocaloric composite filaments of promising magnetocaloric materials: off stoichiometric Ni_2MnGa Heusler alloys and $La(Fe,Si)_{13}$-H.

1.4 Objectives and thesis outline

The study of the MCE is intrinsically related to the study of thermomagnetic phase transitions. This can be seen in the opposite way, i.e., the MCE can be used as a tool for the study of thermomagnetic phase transitions. On the one hand, a first part of the thesis is focused to this end; the use of promising magnetocaloric materials due to their magnetocaloric response that, at the same time, are ideal representatives of the common and complex scenario of overlapping phase transitions. Different cases of multiphase transition materials have been unraveled using different tools, among which is the analysis of the MCE. On the other hand, given the outstanding possibilities of the materials undergoing FOPT, the thesis also addresses the two most important issues that hinder the final use of these materials: the thermal hysteresis and the limitations regarding their shaping into efficient refrigerator beds. The thermal hysteresis in FOPT materials undergoing magnetostructural transformation has been also approached considering and analyzing the effects of the overlapping SOPTs of the structural phases. For the final shaping of these materials, the additive manufacturing using polymer-based composites has been proposed. In this case, the combination of a magnetic or magnetocaloric phase with a non-magnetic one (polymer) make rather different challenges to appear. On the one hand, the manufacturing process has to maintain the properties of the functional fillers and allow a uniform distribution within the polymer matrix. On the other hand, the structural properties of the whole composite, which defines its processing conditions, can be very different to that of the raw polymer and need to be studied and related to the processability.

After this introduction chapter, the thesis is outlined as follows:

In **Chapter 2**, the experimental characterization techniques as well as the standard analysis methods used along this thesis are briefly described.

Chapter 3 presents newly developed magnetocaloric composites combining pure Gd and Gd_3Pd_7 phases, which give rise to a total convoluted response due to the close Curie transitions of the two phases. It is shown that the RC can be improved in composites prepared in this way with respect to that of the pure phases. The situation of overlapping SOPTs has been analyzed by a developed procedure based on the scaling laws of the MCE that allows the deconvolution of the two responses.

Chapter 4 includes the experimental characterization of a series of off-stoichiometric Ni_2MnIn Heusler alloys in which the martensitic transformation appears at different temperatures according to the e/a ratio, while the Curie transition of the austenitic phase is the same for all the alloys. In all the cases there is an appreciable overlap between the two types of phase transitions, which becomes extremely tight in some cases. This produces spikes in ΔS_{iso} that could easily be misinterpreted as artifacts unless the appropriate characterization and analysis methods are used. The determination of the order of the phase transitions in the situation of overlapping FOPT and SOPT by different analysis methods have been performed. Finally, a modification of the developed deconvoluting method presented in previous chapter has been applied to this case of overlapping FOPT and SOPT, enabling the separation of the ΔS_{iso} due to each type of phase transition.

Chapter 5 is dedicated to the study of the thermal hysteresis in FOPT magnetocaloric materials, for which the temperature variant of the first-order reversal curves method is proposed. This method is being recently applied to this type of materials, with results that were essentially limited to fingerprinting the features of the thermal hysteresis. In this thesis, the method has been applied to off-stoichiometry Ni_2MnIn Heusler alloys. The features of the TFORC distributions have been related to the characteristics of the transformation. It has been possible to separate the contributions due to the hysteretic martensitic transformation and the thermomagnetic behavior of the two magnetic phases, with the magnetic transitions located close to the FOPT, by means of a simulation model of the phase transitions in this type of material. The overlapping Curie transitions of the phases, even having a non-hysteretic nature, contribute with specific features to the TFORC distributions.

Chapter 6 and **Chapter 7** are directly connected and dedicated to the manufacturing and characterization of polymer-based composites including magnetic and magnetocaloric fillers. In **Chapter 6** a novel method has been proposed for the manufacturing at laboratory scale of custom composite filaments for FDM. The method has been tested using soft magnetic steel particles, confirming its usefulness for obtaining filaments with dimensional uniformity and enhanced distribution of fillers. The method is then extended in **Chapter 7** to the manufacturing of composite filaments containing magnetocaloric particles of two of the most promising FOPT materials: 1) Heusler alloys, and 2) La(Fe,Si)$_{13}$-H. It is expected that AM using filaments prepared by this method can overcome the major limitations related to the poor machinability and poor structural reliability under cyclic thermal conditions of the relevant FOPT magnetocaloric materials.

Chapter 8 contains the general conclusions of this thesis.

2 Experimental techniques and analysis methods

This chapter presents a brief description of the principles of operation of the different sample fabrication techniques used as well as the standard characterization techniques used throughout the thesis. The chapter also contains the introduction to different standard analysis methods used along the thesis.

In addition to these well-known synthesis, characterization and analysis methods, this thesis proposes a new method for the fabrication of polymer-based composite filaments, novel deconvolution procedures for coexisting phase transitions as well as methods for the interpretation of TFORC distributions. This is the original content of this thesis and will be presented in separate chapters.

2.1 Sample preparation techniques

2.1.1 Arc melting

Arc melting is a common method to produce alloys by melting together different elements or pre-alloys in amounts according to the intended stoichiometry. Metals are melted by an electric arc which is discharged by the application of a large tension between two electrodes: 1) a moving tip-shaped electrode and 2) a copper crucible holding the elements. The melting process can be performed under high vacuum or inert atmosphere to minimize oxidation in the resulting ingots. For compositional homogeneity, the ingots have to be flipped and re-melted several times. The copper crucible is water cooled to avoid its melting while providing a high cooling rate of the final ingots.

2.1.2 Filament extrusion for additive manufacturing

The technique of polymeric-based filament extrusion consists of forcing melted thermoplastic polymer through a nozzle or die of a certain geometry to produce a continuous filament, which will be subsequently used as the starting material for additive manufacturing. In general, the typical extruders consist of: (1) a feed hopper connected to a (2) extruder screw located inside a (3) heated barrel at which its end is (4) the nozzle. The feed is usually in the form of small pellets or powder which it is melted and moved along the extruder to the nozzle by the heated screw.

In the same way, composites can be produced with this technique by combining thermoplastic polymer with fillers. The key point of achieving compositional homogeneity in composite filaments is to be able to mix both components with a constant ratio maintained along the extrusion path to the nozzle. A novel procedure developed during this thesis is presented in **Chapter 6**.

2.2 Characterization techniques

2.2.1 X-ray diffraction

X-ray diffraction (XRD) is a technique commonly used for obtaining information about the underlying crystallographic structure of materials and information on their unit cell dimensions. It is based on the Bragg's condition of diffraction. It occurs when a monochromatic X-ray beam is elastically scattered by the lattice planes of a crystalline material with interatomic distances comparable to λ. The scattered X-rays interfere and produce characteristic XRD patterns that relate the wavelength of the X-ray beam (λ_w), its incidence angle (2θ) and the spacing of the {hkl} planes of the materials (d_{hkl}) by the Bragg's law:

$$\lambda_w = 2d_{hkl} \sin\theta. \tag{2.1}$$

Details about the crystalline phases present in the material can be qualitatively identified or quantified through Rietveld refinement of the XRD patterns. This analysis also offers information on the lattice parameters of the identified crystalline structures.

2.2.2 Micro-computed X-ray tomography

In X-ray tomography, three-dimensional reconstruction of the internal microstructure of the materials can be obtained, though its standard mode cannot provide crystallographic information.

In this thesis, the X-ray tomography method used is based on the different degrees of attenuation that X-rays experience when passing through a material, which depends on the absorption coefficient. The absorption coefficients of X-rays are linked to the density and atomic number of the materials, hence different phases within a composite material can be easily distinguished and quantitatively studied.

During data acquisition, the sample or the X-ray tube is rotated to obtain a series of X-ray measurements of the sample at different angles. The multiple results from the different angles are then processed using reconstructing algorithms to produce 2D slices of the sample. The 2D slices are then stacked using image analysis software to obtain the 3D reconstruction.

2.2.3 Scanning electron microscopy

Scanning electron microscopy (SEM) can provide ultra-high-resolution images of the sample (up to a few nm), revealing its morphology, chemical composition and/or crystal orientation based on the signals from the electron-sample interactions. The electron beam produced by thermionic effect or field emission is accelerated by a large voltage and focused to the surface of the material by means of electromagnetic lenses under high vacuum conditions. From the interaction of the electrons with the sample, different signals are produced and collected by the detectors equipped in the microscope chamber. The emitted signals include secondary electrons, backscattered electrons (BSE), photons (characteristic X-rays for elemental quantification) etc. In this thesis, only the abovementioned are used for the characterization of the samples of study.

The standard imaging of samples for every SEM equipment is obtained through the secondary and backscattered electrons: secondary electrons display the texture and topography while the BSE show atomic contrast of the various phases that can be present in the sample. When the electron beam removes an electron from the inner shell from an atom of the sample, an electron of the atom with higher energy occupies the vacancy and the excess energy is emitted as a photon (in the X-ray spectrum). These X-rays are characteristic of the chemical elements and can be measured through energy-dispersive X-ray spectroscopy (EDX) to quantify the elements present in the sample.

2.2.4 Magneto-optical Kerr microscopy

The Kerr microscopy is based on the magneto-optical Kerr effect (MOKE). This effect describes the process in which polarized light can change its polarization state (rotation of the polarization plane) and intensity when reflected from a magnetized surface. This is due to the Lorentz force experienced by the electrons in magnetized materials.

In MOKE microscope, the light from a controlled light source (usually LED or LASER) is directed through a first polarizer which determines the initial polarization state. The light is then reflected by the sample and passes through a second polarizer (analyzer). The changes in the initial polarization state of the light due to the magnetization of the sample are converted in changes of the light intensity, i.e., changes of the brightness or contrast that can be visualized. Then, upon the application of magnetic field with a defined direction, different contrasts present from the sample surface can be associated to magnetic domains with a magnetization defined by the applied field and the direction of the incident light. Different sensitivities are defined according to the relation between the magnetization vector of the sample and the incidence direction of the polarized light, as represented in **Figure 2.1:**

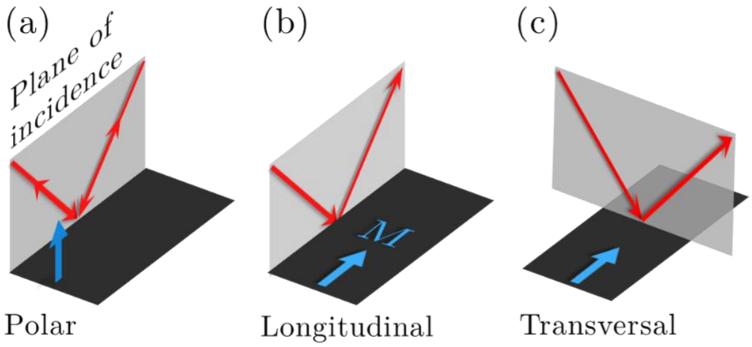

Figure 2.1. Schematic of the different sensitivity modes of MOKE microscopy.

1) Polar sensitivity: the magnetization points perpendicular to the sample surface (out-of-plane magnetization), i.e., it is parallel to the incidence plane of the light. For the polar case, incident light perpendicular to the sample surface can be used as well as light that comes simultaneously from both sides so that the perpendicular component of the reflected light (i.e., parallel to the magnetization vector) is maximized (**Figure 2.1 (a)**).

2) Longitudinal sensitivity: the magnetization vector is parallel to the surface of the sample (in-plane magnetization) and parallel at the same time to the incidence plane (**Figure 2.1 (b)**).

3) Transversal sensitivity: the sample exhibits in-plane magnetization and this is transversal to the plane of incidence of the light (**Figure 2.1 (c)**).

2.2.5 Vibrating sample magnetometry

Vibrating sample magnetometers (VSM) enable the measurement of the magnetic moment of samples based on the Faraday's law of induction. The samples are placed within a uniform magnetic field and made to vibrate at a constant frequency. The vibration of the magnetized sample produces an oscillating magnetic field that causes a change of magnetic flux detected by the pickup coils placed nearby. This magnetic flux change induces an AC electromotive force in the pickup coils that is proportional to the magnetic moment of the sample, with the frequency of the sample vibration. The signal of the pickup coils is then amplified by means of a lock-in amplifier that select the component at the frequency of the sample vibration.

Magnetization measurements in this thesis were performed using: (1) a LakeShore VSM 7407 (with oven and cryostat options, to cover temperature range of liquid nitrogen temperature up to 1273 K) and (2) the VSM option of the Quantum Design Physical Properties Measurement System for magnetic fields up to 9 T.

2.2.6 AC susceptibility

In AC susceptibility measurements, samples are subjected to small-amplitude AC magnetic fields $(H_{AC}(wt) = H_{0,AC}\sin(wt))$ that can be superimposed to a uniform DC magnetic field (H). In this case, the applied AC magnetic field causes an AC magnetic moment in the sample that can be expressed as $M_{AC}(\omega t) = (dM/dH) \cdot H_{0,AC}\sin(\omega t + \varphi)$ where $\chi = dM/dH$ is the magnetic susceptibility corresponding to the $M(H)$ curve that would be recorded upon DC magnetometry (e.g., by using a VSM). This oscillating magnetic moment of the sample is detected by pickup coils so that the susceptibility of the sample is directly obtained. At low frequencies of the applied AC field, the magnetic moment of the sample can follow the field oscillation ($\varphi = 0$) and results similar to those of DC magnetometry are obtained.

At high frequency of the AC field, the oscillating magnetic moment of the sample can show an important phase lag φ due to dynamic effects. Therefore, two components account for the in-phase (χ') and out-of-phase (χ'') components of the AC susceptibility with respect to the applied field:

$$\chi' = \chi \cos\varphi\,, \qquad \chi'' = \chi \sin\varphi. \tag{2.2}$$

This can be thought in terms of the complex plane, in which the in-phase component χ' and the out-of-phase component χ'' correspond to the real and imaginary parts of the susceptibility, respectively. The real part is the slope of the DC $M(H)$ curve, while the imaginary part accounts for the dissipative processes that occur in the sample.

The two components of the AC susceptibility are very sensitive to the changes that the sample undergoes, especially the imaginary part. This technique is a powerful tool to study the phase transitions of magnetocaloric samples as it allows accurate measurements at nearly 0 DC field for performing extensive studies on the influence of the magnetic field on the phase transitions. In this thesis, AC susceptibility has been used for distinguishing overlapping phase transitions.

2.2.7 Differential scanning calorimetry

The differential scanning calorimetry (DSC) is a thermal analysis technique for the measurement of the heat energy transferred to or from a sample while its temperature is controlled. The DSC equipment used along the thesis is classified as heat-flux DSC. During the temperature change, a heat-flux DSC measures the temperature of an empty reference pan (with known heat capacity and mass) and the temperature of an identical pan containing the sample. Both pans are placed on separate thermocouples in a common furnace chamber. Due to the heat capacity (C_p) of the sample, there will be a temperature difference between the empty pan versus that containing the sample from which the heat flow is determined.

The DSC technique provides information on the thermodynamic parameters of phase transitions. The change of the C_p of the materials due to the phase transitions undergone leads to changes in the heat flow. The subtle change of C_p upon a SOPT, for which there is no change in the enthalpy, (e.g., a Curie transition or a glass transition) can be slightly visualized as a step in the heat flow baseline. In contrast, the theoretical divergence of the C_p in FOPTs produces a cusp-like heat flow peak that can be integrated to obtain the latent heat involved among other parameters of the transformation.

2.2.8 Thermogravimetric analysis

The thermogravimetric analysis (TGA) is a method of thermal analysis in which the mass of a sample is continuously recorded while its temperature is changed in a controlled way. The typical setup of TGA instrument consists of a high-precision balance in which the pan containing the sample is placed in a furnace for the temperature control. TGA measurements provide information on processes such as thermal decomposition, absorption and adsorption/desorption, in which a mass change is involved.

In this thesis the TGA has been used exclusively to characterize the polymer-based magnetic composites as it provides a direct determination of the wt. % of the metallic fillers upon the temperature degradation of the polymer matrix.

2.2.9 Viscoelastic characterization

A material possesses viscoelastic behavior if it exhibits both elastic and viscous characteristics when subjected to any type of deformation. The viscoelasticity is characterized upon the application of an oscillatory force (stress) and determining the relation between the applied stress and the deformation (strain) produced in the material. In purely elastic materials, the applied stress and the resulting strain are in phase. Conversely, in purely viscous materials the resulting strain and the applied stress are out-of-phase with a phase lag of $\pi/2$. Then, viscoelastic materials show a phase lag in between of elastic ($\varphi = 0$) and viscous ($\varphi = \pi/2$) behaviors.

The oscillatory strain, σ, can be expressed as $\sigma(t) = \sigma_0 \sin(\omega t)$, where σ_0 is the amplitude and ω is the angular frequency of the oscillation. The applied stress can be expressed as $\epsilon(t) = \epsilon_0 \sin(\omega t + \varphi)$, assuming a phase lag φ (the stress precedes the strain). The ratio between the applied oscillatory stress and subsequent strain defines the dynamic modulus, which can be represented in the complex plane and divided into real (in-phase) and imaginary (out-of-phase) parts.

One of the common ways of characterizing the viscoelastic properties of materials is by the application of shear stress. In this case, the dynamic moduli are defined as:

$$G' = \frac{\sigma_0}{\epsilon_0} \cos\delta\,, \qquad G'' = \frac{\sigma_0}{\epsilon_0} \sin\delta, \tag{2.3}$$

where G' is called as shear storage modulus as it accounts for the elastic energy that is stored in the sample (real part) and G'' is called shear loss modulus as it represents the portion of the energy that is dissipated in the sample. From the two moduli, the complex viscosity of the material, η^*, can be obtained with real and imaginary components as:

$$\eta' = \frac{G''}{\omega}, \qquad \eta'' = \frac{G'}{\omega}, \tag{2.4}$$

It is also common to use continuous shear stress to determine the flow properties of the materials. This type of measurements directly provides the viscosity of the material under steady-state shear stress.

The viscoelastic analysis, not usual in magnetic-based works, has been used in the part of polymer-based magnetic composites to explain the modification of the processing conditions of the composites by the addition of the metallic powders.

2.3 Analysis methods for the study of thermomagnetic phase transitions

2.3.1 Determination of the isothermal entropy change from magnetic measurements

According to **Equation (1.2)**, the isothermal entropy change, $\Delta S_{iso}(T,H)$, can be obtained from magnetization measurements, $M(T,H)$. The way of applying the Maxwell relation is by a discretization of both the derivative and integral functions as:

$$\begin{aligned}\Delta S_M(T,H_N-H_1) &= \mu_0\int_0^H\left(\frac{\partial M(T,H)}{\partial T}\right)_H dH \\ &\approx \sum_{j=1}^{N-1}\left(\frac{\left(M_{i+1,j}-M_{i,j}\right)+\left(M_{i+1,j+1}-M_{i,j+1}\right)}{T_{i+1}-T_i}\right) \\ &\times\frac{\mu_0\left(H_{j+1}-H_j\right)}{2}.\end{aligned} \tag{2.5}$$

For the application of the Maxwell relation, an appropriate set of $M(T,H)$ data can be obtained by measuring M vs. T for different constant magnetic fields (isofield $M(T)$ curves), or by measuring M vs. H at different constant temperatures (isothermal $M(H)$ curves). As the temperature cannot be swept at a high rate to avoid the thermal inertia and that the heat released during the phase transition affects the temperature of the sample, isothermal $M(H)$ measurements are usually much faster than isofield $M(T)$ ones.

In the case of materials showing thermomagnetic SOPT, both measuring methods are equally valid without any consideration due to the absence of thermal hysteresis in SOPTs. In such case the measurement of isothermal $M(H)$ curves is more convenient in almost every situation.

However, the characterization of the ΔS_{iso} in the case of materials undergoing thermomagnetic FOPT requires some caution. These phase transitions are driven both by temperature and magnetic field and are accompanied by thermal hysteresis. This means that the state of the material can change while conducting an isothermal $M(0\rightarrow H)$ curve and it cannot be reverted to the initial state at that temperature by just going to the initial zero field due to the thermal hysteresis. Therefore, it is necessary to reset the state of the material before measuring the next isotherm to ensure that each $M(H)$ curve is not affected by the previous measurement as this causes erroneous results when computing ΔS_{iso}. This is done by following a discontinuous measuring protocol in which the sample is brought to a temperature at which the transformation has finished prior to each $M(H)$ measurement. Numerous studies have shown that the results obtained by the Maxwell relation from isothermal $M(H)$ are free from artifacts when using a discontinuous measuring protocol, in agreement with those obtained by isofield $M(T)$ curves [77–80]. Although the resetting protocol is needed when utilizing isothermal $M(H)$ curves to characterize the ΔS_{iso} in magnetocaloric materials undergoing FOPT, the total time of the experiments is still lower with respect to the use of isofield $M(T)$ measurements. In addition, the higher resolution with field in the case of measuring isothermal $M(H)$ curves allows a more precise study of the field dependence of the MCE, which is an analysis method widely used along this thesis.

In this thesis, most of the studied materials undergoing FOPT are Heusler alloys showing a magneto-structural transformation from low temperature martensitic phase to high temperature austenite with higher magnetization. When following the heating branch of the transformation, the resetting protocol used consists of cooling the sample in 0 field down to the single martensitic region, i.e., far away from the FOPT. Then, continuing with 0 applied field, the sample is heated up and stabilized at the desired temperature (avoiding any temperature overshoot), temperature at which the magnetic field is swept from 0 to maximum and then back to 0. For the cooling branch of the transformation, the resetting state is at the high temperature region so that the temperatures for the isothermal $M(H)$ curves are reached by cooling the sample down from the single austenitic phase at 0 field. Analogously, the field in that case is swept from 0 to maximum and back to 0 during the measurement.

The other case studied along the thesis of a material undergoing FOPT corresponds to a La(Fe,Si) system showing a magnetoelastic transformation.

Despite the different nature of this FOPT, it can be characterized in the same way as abovementioned protocols.

2.3.2 Scaling laws of the magnetocaloric effect in second-order phase transitions

The $\Delta S_{iso}(T)$ obtained for different fields in a SOPT collapse onto a single universal curve when they are rescaled in the appropriate manner [81–83]. The $\Delta S_{iso}(H)$ axis is rescaled by normalizing each curve to its respective peak, $\Delta S_{iso}^{pk}(H)$. The rescaling of the temperature axis follows a different approach, in which it is necessary to establish reference points at which the $\Delta S_{iso}(H)$ curves are equivalent. One possible point is at the position of the maxima, T_{pk}, which is established as the origin of the new axis. Additional reference temperatures, T_r, are chosen as those for which the $\Delta S_{iso}(H)$ correspond to a specific fraction of its corresponding peak, i.e., $\Delta S_{iso}(T_r) = \chi \cdot \Delta S_{iso}^{pk}$ where χ is usually between 0.5 and 0.7. In the general case, a reference temperature is established below the peak ($T_{r,1}$) and another above the peak ($T_{r,2}$). The temperature coordinates of each $\Delta S_{iso}(H)$ curve are then transformed to new θ coordinates according to:

$$\theta = \begin{cases} -(T - T_{pk})/(T_{r,1} - T_{pk}) & \text{if } T \leq T_{pk} \\ (T - T_{pk})/(T_{r,2} - T_{pk}) & \text{if } T > T_{pk} \end{cases} \tag{2.6}$$

It can be easily verified that the origin of the θ-axis is at T_{pk}, i.e., $\theta(T_{pk}) = 0$, and that the values at the reference temperature are fixed to ± 1: $\theta(T_{r,1}) = -1$ and $\theta(T_{r,2}) = 1$. The scaling is also possible by using one reference temperature.

In order to illustrate the application of the universal scaling of the MCE in SOPTs, the ΔS_{iso} due to a Curie transition has been simulated using the Arrott-Noakes equation of state [84]:

$$H^{1/\gamma} = a(T - T_C)M^{1/\gamma} + bM^{1/\beta + 1/\gamma}. \tag{2.7}$$

The parameters γ and β in **Equation (2.7)** are the critical exponents associated to the transition, while a and b are the fitting parameters. The

Arrott-Noakes equation of state in its general form, as presented previously, is also valid for materials that do not obey the mean field model. However, in the case of the mean field model (where $\gamma = 1$, and $\beta = 0.5$) the equation is simplified as:

$$H = a(T - T_C)M + bM^3. \tag{2.8}$$

Previous equation has been used to simulate isothermal $M(H)$ curves for the application of the Maxwell relation to calculate ΔS_{iso} according to **Equation (2.5)**. The parameters used for the mean field version of the Arrott-Noakes equation of state reproduce a response typical of amorphous alloys at room temperature ($T_{pk} = 300\text{ K}$, $a = 1\text{ T K}^{-1}(\text{A m}^2\text{ kg}^{-1})^{-1}$ and $b = 0.1\text{ T }(\text{A m}^2\text{ kg}^{-1})^{-1/3}$).

The obtained ΔS_{iso} curves for fields ranging from 0.1 to 1 T using a step of 0.01 T are presented in the inset of **Figure 2.2 (a)**. For the rescaled curves shown in **Figure 2.2 (a)**, two reference temperatures have been used: $T_{r,1}$ on the left-side of the peak so that $\Delta S_{iso}(T_{r,1}) = 0.7 \cdot \Delta S_{iso}^{pk}$, and $T_{r,2}$ on the right-side of the peak matching the condition $\Delta S_{iso}(T_{r,2}) = 0.5 \cdot \Delta S_{iso}^{pk}$. A perfect collapse of all the curves (90 curves in total) onto a single curve is observed.

On the one hand, this collapse serves as a qualitative determination of the second-order character of a transformation. On the other hand, the universal curves can be used to reconstruct the ΔS_{iso} response, being possible an extension to magnetic fields not reached during the measurements as well as an extension of the temperature range of the curves for high fields. The reason for this is the power law dependence of both $|\Delta S_{iso}^{pk}|$ and $|T_r - T_{pk}|$ in SOPTs, i.e., $|\Delta S_{iso}^{pk}| \propto H^n$ and $|T_{r,i} - T_{pk}| \propto H^\tau$. **Figure 2.2 (b)** shows the field dependence of $|\Delta S_{iso}^{pk}|$ and $|T_{r,i} - T_{pk}|_{i=1,2}$ in log scale, being evident the linearity of these three curves. The scaling can be undone by using the fitted parameters of the field dependence of $|\Delta S_{iso}^{pk}|$ and $|T_r - T_{pk}|$, with the possibility of extending the results beyond the maximum field used in the measurements.

Additionally, it is worth noting that not every rescaled curve has the same θ range. As the ΔS_{iso} response due to SOPT gets broader when increasing field, the T_r gets further away from the T_{pk} with increasing the field as shown in the inset **Figure 2.2 (b)** in which the $T_{r,i}$ trend to T_{pk} for 0 field and gets progressively further as the field increases. This means that, according to **Equation (2.6)**, the θ range is reduced with increasing field. It implies that the use of the rescaled curve for the lowest possible field will directly allow a temperature extension of the reconstructed ΔS_{iso} for higher fields.

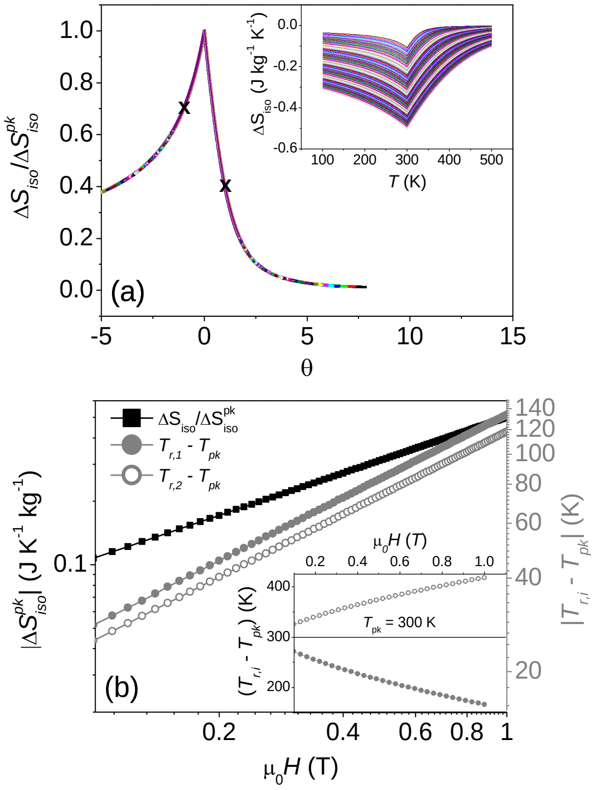

Figure 2.2. (a) inset: ΔS_{iso} obtained by the Maxwell relation from simulated magnetization data using the Arrott-Noakes equation of state for a SOPT. **(a)** Universal scaling of the ΔS_{iso} using 2 reference temperatures, $T_{r,i}$, (marked by “×”). **(b) inset** field dependence of $T_{r,i} - T_{pk}$ in linear scale **(b)** Field dependence of ΔS_{iso}^{pk} and $|T_{r,i} - T_{pk}|$ in logarithmic scale.

2.3.3 Determination of the order of thermomagnetic phase transitions: field dependence of the magnetocaloric effect

A traditional analysis method for this is based on the Banerjee's criterion [85]. According to this criterion, the Arrott plots (M^2 vs. $\mu_0 H/M$) should only show positive slopes in SOPT materials while negative slopes will be observed in case of analyzing a FOPT.

Based on the field dependence of the MCE, a perfect collapse onto a single universal curve of the $\Delta S_{iso}(H)$ response of a material unequivocally confirms the second-order character of the transition. However, there are different causes that can prevent the collapse when analyzing a SOPT, e.g., the presence of an additional phase transition (FOPT or SOPT) [86,87].

The field dependence of ΔS_{iso} in the form of the exponent n is closely related to the magnetic state of the material [81,88]:

$$n(T,H) = \frac{d\ln|\Delta S_{iso}|}{d\ln|H|}. \tag{2.9}$$

The exponent n trends to 1 in the ferromagnetic state of a material, while its trend changes to values around 2 in the paramagnetic region. For materials undergoing a Curie transition, the exponent n follows a characteristic curve that starts with values around 1 in the ferromagnetic state, then goes a minimum at the Curie transition followed by the final trend to 2 in the paramagnetic region with increasing temperature. The value of the minimum at the Curie transition is related to the critical exponents of the transition. Therefore, exponent n can also be a tool for studying materials undergoing more than one Curie transitions.

Recently, the study of the field exponent n has been extended to the analysis of FOPTs, which allowed to identify a characteristic fingerprint of this type of thermomagnetic phase transitions. The exponent n shows a maximum of $n > 2$ in FOPTs, serving as a very sensitive and quantitative criterion for determining the order of thermomagnetic phase transitions [89]. In this thesis, exponent n will also be used for studying the concurrent phase transitions, SOPTs and/or FOPT+SOPT, in multiphase magnetocaloric materials.

2.3.4 First-order reversal curve method for the characterization of hysteresis

The analysis of hysteresis through the first-order reversal curve (FORC) method started from the Preisach model of hysteresis [90]. It assumes that the hysteretic system is composed by a set of discrete hysteretic entities (hysterons) whose behavior is described by a nonlinear relay with time-dependent input and output. The output of the hysterons can only show two stable states called “up”, and “down” and the transition from one branch to the other occurs after the extremum values of the input signal or “switching fields”.

Based on this model, the FORC method was initially developed as a mathematical tool to identify the distribution of a classical Preisach model [91]. The FORC method has been further extended and its experimental implementation was proposed and applied to obtain a FORC distribution in ferromagnetic systems [92]. Although the experimental FORC distributions in ferromagnetic systems do not exactly coincide with the Preisach distribution, it can be related to the interaction and coercivity distributions of the system.

Considering the original case of the $M-H$ hysteresis as a reference, the FORC method consists of defining a series of minor hysteresis loops starting at a state in which the system is fully saturated (usually in the global “up” state) by applying a sufficiently large magnetic field, H_{sat}. From saturation, the field is swept down to a reversal state within the hysteresis loop, $H_{r,i} \leq -H_{sat}$, from which the field is then increased back to H_{sat}. The path from $H_{r,i}$ to H_{sat} defines a single FORC. This process is repeated for different $H_{r,i}$ until sufficient FORCs are obtained. The FORC distribution $\rho(H_r, H)$ is defined as the mixed second derivative:

$$\rho(H_r, H) = -\frac{\partial^2 M(H_r, H)}{\partial H_r \partial H}. \tag{2.10}$$

The distribution can be plotted in the $H_r - H$ plane, but it is usual to change the coordinates to the Preisach plane (see **Figure 2.3** (a)), which is defined by the interaction field $H_u = -(H_r + H)/2$ and the coercivity field $H_c = (H - H_r)/2$ axes, which reflect the center of the distribution and its absolute width, respectively. This coordinate change corresponds to a rotation of 45° of the axes of the distribution as shown in **Figure 2.3** (b).

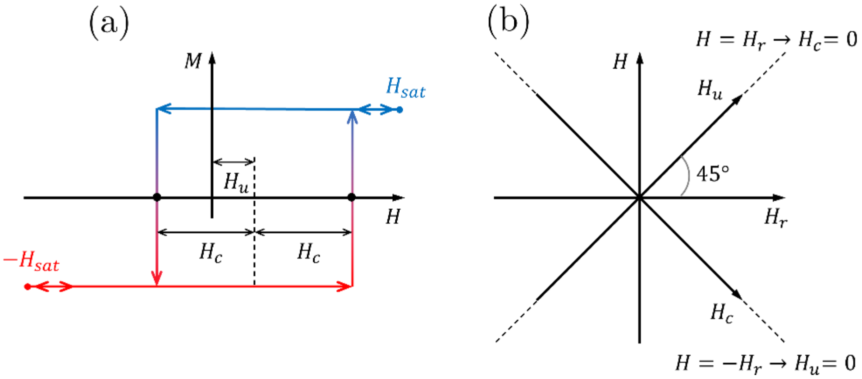

Figure 2.3. (a) Schematic representation of a square hysteresis loop between the saturation fields $\pm H_{sat}$ (hysteron).**(b)** Relation between original $H_r - H$ plane of the FORC distribution and the Preisach plane formed by the H_c and H_u axes.

This method is commonly applied for the characterization of diverse types of magnetic materials, such as recording media [92,93], permanent magnets [94], nanowires clusters [95–97] or multiphasic SOPT magnetocaloric materials [98]. In addition, it can be applied to characterize any type of hysteresis: ferromagnetic, ferroelectric, thermal, etc.

There are precedents of applications of the FORC method for the analysis of thermal hysteresis, highlighting works on spin-crossover materials [99,100]. The temperature variant of the original FORC method (TFORC) has been further extended and applied to magnetocaloric materials exhibiting FOPT [101–105]. The methodology for obtaining a TFORC distribution in FOPT magnetocaloric materials is totally analogous to the one described previously. The TFORC distribution is defined as:

$$\rho(T_r,T) = \pm\frac{\partial^2 M(T_r,T)}{\partial T_r \partial T}. \tag{2.11}$$

In this case, there can be difference in the distributions obtained by cooling or heating as its characteristics highly depend on the transformation kinetics, which may not be symmetric in one direction with respect to the other. Therefore, the plus and minus signs in **Equation (2.11)** refer to the heating and cooling branches, respectively, so that both distributions have the same sign.

The experimental protocol followed for obtaining a single reversal curve for the TFORC distributions consists of measuring, after saturation of the sample, magnetization versus temperature for a fixed magnetic field from a reversal temperature (T_r) back to the saturation temperature (T_{sat}) in which the sample is in single phase state. This procedure is repeated for different reversal temperatures to cover the region in which there is thermal hysteresis. Obtaining a well-resolved TFORC distribution by **Equation (2.11)** requires many points along both T_r and T axes to enable an efficient suppression of experimental noise, which usually magnifies when differentiating. Although the high resolution in the T axis is achieved due to its continuous sweeping, the acquisition of a significant number of minor loops (i.e., T_r points) is unfeasible in this case due to the resetting process and the low temperature sweeping rate that are required. Hence, a smoothing mechanism that works efficiently with the limited FORC data is required.

A smoothing algorithm was proposed by Pike et al. for obtaining HFORC distributions. It consists of fitting the dataset to polynomial surfaces (typically of second order along both directions), avoiding the cross derivatives [92]. In the case of temperature reversal curves, there is a limited number of T_r points, which requires a conservative smoothing factor along T_r while a higher smoothing can be considered along T. Then, as in Ref. [101], a variation of Pike's algorithm has been used in which the dataset has been fitted to a polynomial surface which is linear in T_r and quadratic in T, which has been demonstrated to provide a good compromise between smoothing and significance of the calculations in the previous TFORC study of Ref. [101].

Once the TFORC distributions are calculated using the experimental temperature variables T_r and T, they are rotated 45° by changing axes to T_u and T_h. However, $M(T)$ are not symmetric with respect to the center of the axes, making necessary to obtain the central temperature of the distributions as the center of the full $M(T)$ loop for each fixed magnetic field, T_{center}. Accordingly, the change of axes is performed $T_h = |T_r - T|/2$ and $T_u = (T_r + T)/2 - T_{center}$.

In this thesis, the thermal hysteresis of Heusler alloys undergoing magneto-structural transformation upon cooling and heating, is studied from cooling and heating TFORC distributions. In cooling TFORC, the saturation state is at a low temperature well in the martensitic phase region, which is reached upon cooling from each T_r. In heating TFORC, the saturation state corresponds to a high temperature in the region of single austenitic phase that is reached in each reversal curve upon heating. Analogously to the discontinuous measurement protocol used for calculating the ΔS_{iso}, the protocol used here ensures that each reversal curve is not affected by the previous one by starting and finishing every curve in the same T_{sat} far away from the FOPT. All these $M(T)$ measurements were performed with the VSM option of a PPMS where the temperature was continuously swept at the rate of 0.5 K min^{-1}, which is sufficiently low to minimize thermal inertia. Experimental points were taken every interval of 0.25 K.

3 Magnetocaloric materials undergoing multiple second-order phase transitions

Magnetocaloric materials undergoing SOPT are attractive for practical devices working cyclically primarily because of their absence of thermal hysteresis. However, their responses are typically of limited magnitude. In this chapter, Gd-based composites have been developed and proposed as a way to enhance the performance of SOPT materials. The convenient combination of phases with Curie transitions close to each other can lead to a total MCE with a broader temperature span and increased RC. However, this has to be made in such a way that the broadening of the response is not at the expense of a very small amplitude of the magnetocaloric peak, which would not be useful for applications. For this, composites with different fractions of Gd and Gd_7Pd_3 phases have been developed, leading to an increase in the RC with respect to pure Gd.

From a more fundamental point of view, the analysis of the field dependence of the MCE by the exponent n has been shown to be a useful tool for the detection of overlapping phase transitions, even when the presence of the second phase is not evident from the magnetic and MCE results. This chapter shows a novel procedure that allows the deconvolution of magnetocaloric responses of overlapping SOPTs. It is based on the scaling laws of the MCE and has been successfully applied to the Gd-Gd_7Pd_3 composite with the highest RC. The deconvoluted magnetocaloric responses have been used to obtain the phase fraction of the sample, providing results in agreement with the values obtained from XRD measurements.

3.1 Magnetocaloric Gd/Gd-Pd composites

With the aim of investigating the convoluted response of magnetocaloric composite materials, different amounts of Pd have been added to Gd to elaborate novel composites with coexisting Gd and Gd_7Pd_3 phases. Gd_7Pd_3 has a significant MCE near room temperature due to a Curie transition at ~335 K, thus being close to that of Gd. By varying the fractions of the two elements, composite samples with different proportions of the two phases have been achieved, ranging from Gd_7Pd_3 being a minor phase to a composition in which it becomes slightly predominant [106].

3.1.1 Synthesis

From the phase diagram of the Gd-Pd binary system as shown in **Figure 3.1**, a single Gd_7Pd_3 phase appears for 30 at.% Pd. Thus, varying Pd amounts of 5 to 20 at. % should produce samples with coexisting Gd and Gd_7Pd_3 phases without the need for any additional preparation step (e.g., thermal annealing). The intermetallic Gd_7Pd_3 phase coexists with the extra Gd that does not combine with Pd.

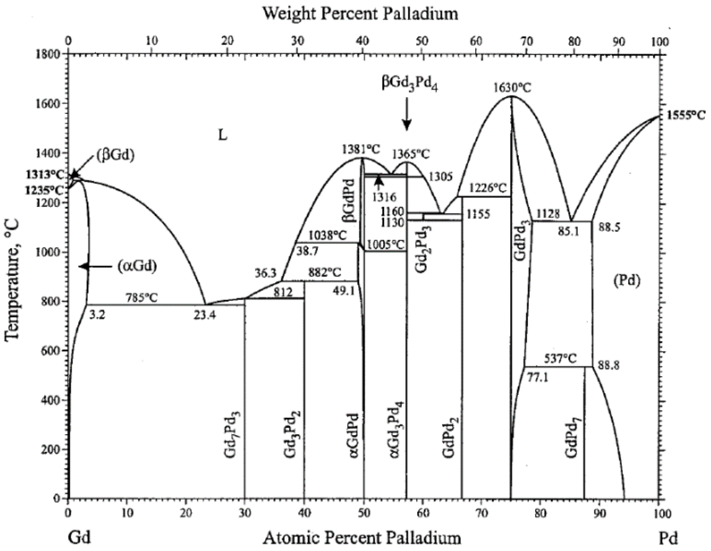

Figure 3.1. Phase diagram of Gd-Pd system obtained by Z. Du and H. Yang in Ref. [107], and presented in this version in Ref. [108].

Bulk samples with nominal stoichiometry $Gd_{100-x}Pd_x$ (x = 5, 10, 15, 20 at. %) were synthesized at Czestochowa University of Technology by arc melting high purity raw elements under Ar-controlled atmosphere. The ingots were flipped and melted again several times to ensure a good homogeneity of the bulk material.

3.1.2 Microstructural and compositional analysis

The biphasic character of the samples is observed by scanning electron microscopy (SEM) using a JEOL JSM 6610LV microscope equipped with an energy dispersive X-ray (EDX) spectrometer. The SEM micrograph and EDX results presented in **Figure 3.2** shows that the sample with 5 at.% Pd ($Gd_{95}Pd_5$ sample) exhibits pure Gd phase (depicted as oval-like shapes labeled as Area 1) surrounded by the intermetallic Gd_7Pd_3 phase (Area 2).

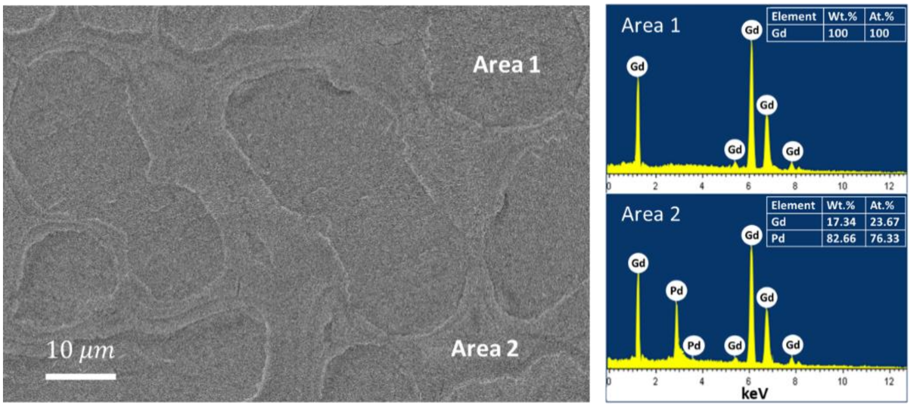

Figure 3.2. SEM image of $Gd_{95}Pd_5$ sample with the EDX results on the two selected areas.

The compositions of the two phases are confirmed through the EDX spectrum. The EDX results for all the samples of the series are summarized in **Table 3.1**. X-ray diffraction (XRD) measurements were carried out on ground samples to further study their biphasic character and to obtain the structural parameters of the phases. The XRD patterns are shown in **Figure 3.3**, where the peaks corresponding to hexagonal Gd ($P6_3/mmc$) and hexagonal Gd_7Pd_3 (Th_7Fe_3-type, $P6_3mc$) are identified for all samples. The presence of gadolinium oxide in the form of Gd_2O_3 (cubic Fm3m) is also observed, which could be ascribed to the oxidation of Gd phase at the surface of ground samples.

Table 3.1. EDX results obtained from distinguishable areas of the samples.

Sample	Phase	Wt. %	At. %
$Gd_{95}Pd_5$	Gd	Gd – 100	Gd – 100
	Gd_7Pd_3	Gd – 82.66 Pd – 17.34	Gd – 76.33 Pd – 23.67
$Gd_{90}Pd_{10}$	Gd	Gd – 100	Gd – 100
	Gd_7Pd_3	Gd – 79.19 Pd – 20.81	Gd – 72.02 Pd – 27.98
$Gd_{85}Pd_{15}$	Gd	Gd – 100	Gd – 100
	Gd_7Pd_3	Gd – 74.15 Pd – 25.85	Gd – 65.99 Pd – 34.01
$Gd_{80}Pd_{20}$	Gd	Gd – 100	Gd – 100
	Gd_7Pd_3	Gd – 77.89 Pd – 22.17	Gd – 70.44 Pd – 29.56

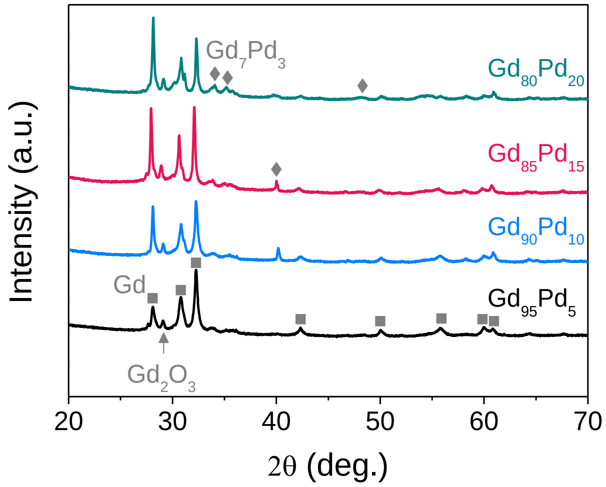

Figure 3.3. XRD patterns of $Gd_{100-x}Pd_x$ (x = 5, 10, 15, 20) composite samples. Square and diamond symbols indicate the peaks corresponding to Gd and Gd_7Pd_3 phases, respectively. The Gd_2O_3 attributed to surface oxidation has also been considered and computed (denoted by the gray arrow).

Rietveld refinement of the XRD patterns was also performed to analyze the phase fractions and the lattice parameters of the recognized phases in the samples. The refinement results are summarized in **Table 3.2**. There is an increasing fraction of Gd_7Pd_3 phase with increasing Pd content and, as consequence, a reduction of the proportion of Gd phase. No relevant changes between the lattice parameters of the different compositions are observed.

Table 3.2. Phase fractions in weight percentage and lattice parameters obtained from the Rietveld refinement.

Sample		Phases		
		Gd	Gd_7Pd_3	Gd_2O_3
$Gd_{95}Pd_5$	wt. %	61.0	33.1	5.9
	Lattice parameters (Å)	a = 3.639 c = 5.781	a = 9.975 c = 6.275	a = 5.305
$Gd_{90}Pd_{10}$	wt. %	56.9	36.2	6.9
	Lattice parameters (Å)	a = 3.629 c = 5.752	a = 9.961 c = 6.286	a = 5.312
$Gd_{85}Pd_{15}$	wt. %	46.8	46.4	6.8
	Lattice parameters (Å)	a = 3.615 c = 5.740	a = 9.893 c = 6.362	a = 5.312
$Gd_{80}Pd_{20}$	wt. %	42.9	48.4	8.7
	Lattice parameters (Å)	a = 3.630 c = 5.745	a = 9.974 c = 6.281	a = 5.294

3.1.3 Magnetic and magnetocaloric characterization

Magnetization measurements were performed using a LakeShore 7407 vibrating sample magnetometer (VSM) with a maximum applied field of 1.5 T. To reduce the effect of the demagnetizing field to a minimum, samples were prepared in needle-like shapes and oriented with the long axis parallel to the direction of the applied magnetic field. Additionally, the magnetization curves were corrected for the effect of the demagnetizing field prior to the calculation of the magnetocaloric response [109,110].

The ΔS_{iso} of the different composite samples are plotted in **Figure 3.4 (a)**. The peak corresponding to Gd appears at ~288K. With increasing Pd content, a growing second peak appears at ~338 K (marked with an arrow in **Figure 3.4 (a))**, which is associated to the Curie transition of the intermetallic Gd_7Pd_3 phase. The increasing response of Gd_7Pd_3 phase with increasing Pd content is followed by the subsequent decrease in the response of Gd phase, as a larger amount of Gd becomes part of the intermetallic phase. **Figure 3.4 (b)** shows the refrigerant capacity (RC) obtained from the responses in **Figure 3.4 (a)**. Considering the RC value of Gd at 1 T as reference (denoted by the horizontal line), a decrease of RC is obtained when alloying up to 10 at. % Pd. This is because the minor Pd alloying, i.e., minor secondary Gd_7Pd_3 phase, leads to a small peak that does not contribute to the$RC.$ Therefore, the only effect of the new additional phase is a decrease in the response of Gd due to dilution. When the content of Pd dopant is further increased, RC starts to increase and reaches a maximum value for the $Gd_{80}Pd_{20}$ sample, being 10 % higher than that of Gd. This agrees with literature, wherein it is reported that for the enhancement of the RC in a SOPT magnetocaloric composite, the majority phase should correspond to that with higher transition temperature [29]. This condition is only fulfilled for the $Gd_{80}Pd_{20}$ sample.

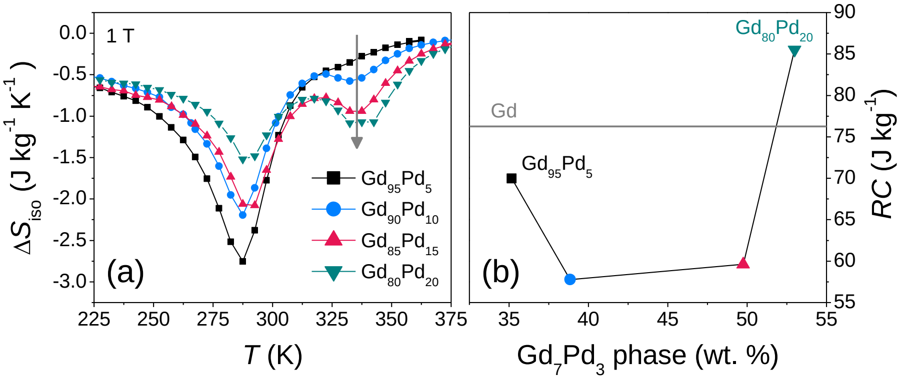

Figure 3.4. (a) Temperature dependence of the isothermal entropy change of the alloys from the series $Gd_{100-x}Pd_x$ for a magnetic field of 1 T. **(b)** Refrigerant capacity as a function of the weight percent of the intermetallic Gd_7Pd_3 phase within the composites calculated from the responses in **(a)**. As a reference, the horizontal line corresponds to the RC of pure Gd.

Figure 3.5 shows the temperature dependence of exponent n of the composite samples. The usual n behavior of a Curie transition is observed twice in these cases: exponent n that trends to values around 1 at low temperatures when both phases are in the ferromagnetic state, followed by a minimum corresponding to the Curie transition of Gd phase (at ~288 K) then a second minimum (at ~338 K) due to the Curie transition of the intermetallic phase, and finally increase to values that tend to 2 in the paramagnetic region of the two phases. In between the two minima, there is a local maximum due to the combination of a paramagnetic and a ferromagnetic phase, reaching values in between 1 and 2, being closer to 2 when there is a larger fraction of the Gd phase.

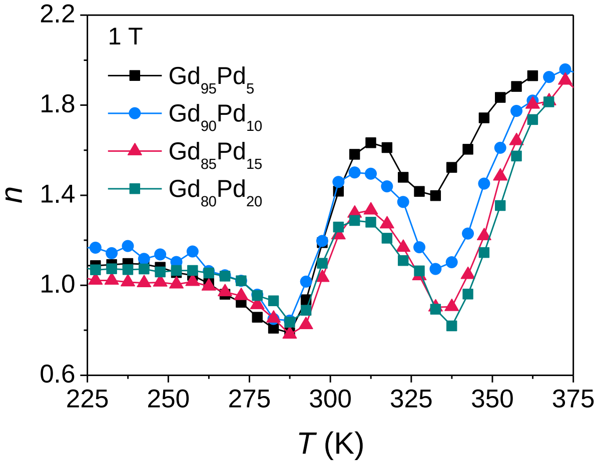

Figure 3.5. Temperature dependence of the exponent n of the alloys from the series $Gd_{100-x}Pd_x$ (x = 5, 10, 15, 20 at. %) for a magnetic field of 1 T.

In agreement with the mean field theory, n is closer to 2/3 at the transition of Gd in these samples since this phase always corresponds to a relevant fraction of the total material. However, values are still higher than 2/3 due to the contribution of the Gd_7Pd_3 phase, which is still ferromagnetic at that temperature. In the case of the transition of Gd_7Pd_3 phase, the associated minimum of n decreases with increasing Pd content, which agrees with previous results, indicating higher amount of Gd_7Pd_3 phase. It is worth mentioning that the minimum of n corresponding to the Curie transition of Gd_7Pd_3 phase in $Gd_{95}Pd_5$ sample is clearly observed, whereas it is not evident at all in the $\Delta S_{iso}(T)$ curves. Thus, it is also demonstrated the effectiveness of the exponent n to distinguish overlapping phase transitions even when one of them presents an insignificant $\Delta S_{iso}(T)$ response.

3.2 Deconvolution of magnetocaloric responses due to overlapping second-order phase transitions

In addition to the previously studied composites, which had several phases by design, magnetocaloric materials can unintentionally be multiphasic due to residual phases or impurities that appear during synthesis. Apart from the fundamental point of view, a deconvolution mechanism will be useful in practice for any of these situations as it would be relevant to find out the actual magnetocaloric response of the different phases from the total response of the multiphasic composite material. This will enable the prediction of the response of each phase similar to synthetizing them as a single-phase material.

Taking the previously studied $Gd_{80}Pd_{20}$ composite as the model case, a methodology to deconvolute the overlapping SOPTs based on the scaling laws of the MCE is proposed. A full collapse of the rescaled curves is not possible due to the dual phase character of the composite [86,87], which has similar concentration of the two phases and both present close Curie transitions. Nevertheless, it is shown how the distorted rescaled curves can still be used to reconstruct the magnetocaloric responses of the individual phases, deconvoluting the total MCE of the composite [111].

3.2.1 Scaling procedure

The scaling procedure has been applied to the total response of the biphasic sample, considering separately each of the phase transitions. On the one hand, referring to the Gd phase, the total $\Delta S_{iso}(T)$ curves for the different magnetic fields have been normalized using the peak values corresponding to the Curie transition of Gd phase, $\Delta S_{iso}^{pk,1}(H)$. The temperature axis is transformed to the θ_1 variable with origin at the temperature of the Gd peak, $T_{pk,1}$, using one reference temperature for rescaling, $T_{r,1}(H)$, which was selected on the left of this peak and for which the total ΔS_{iso} corresponds to half of its value at the peak, i.e., $\Delta S_{iso}(T_{r,1}) = 0.5 \cdot \Delta S_{iso}^{pk,1}$. On the other hand, when the scaling is referred to the Gd_7Pd_3 Curie transition, the total convoluted curves are normalized using the corresponding peak values, $\Delta S_{iso}^{pk,2}(H)$. The rescaled temperature θ_2 has its origin at the temperature of the Gd_7Pd_3 peak, $T_{pk,2}$, using one reference temperature $T_{r,2}(H)$ on the right of this peak so that $\Delta S_{iso}(T_{r,2}) = 0.4 \cdot \Delta S_{iso}^{pk,2}$. The reason for these choices of reference temperatures is to avoid that they are influenced by the other phase transition, which mostly happens in the temperature range between peaks. The temperature axis transformation according to the transition being considered for scaling ($i = 1, 2$ for Gd and Gd_7Pd_3 phases, respectively) can be described as:

$$\theta_1 = -(T - T_{pk,1})/(T_{r,1} - T_{pk,1}), \tag{3.1}$$

$$\theta_2 = (T - T_{pk,2})/(T_{r,2} - T_{pk,2}). \tag{3.2}$$

Figure 3.6 (a) and **(b)** show the rescaled curves of the total response of the composite sample for the different magnetic fields when the scaling is referred to Gd and Gd_7Pd_3 phase transitions, respectively. For both cases, the curves for the lowest (0.09 T) and highest fields (1 T) are highlighted to illustrate how the magnetic field affects the rescaled curves. With increasing magnetic field, the two peaks in both cases come closer to each other, with a local minimum between them that becomes shallower. This indicates an increasing overlap between the two transitions with increasing magnetic field, being evident that there is a tight overlap for 1 T (red curves). This is because the Curie transitions produce magnetocaloric responses that increase in width on both sides of the peak with increasing magnetic field while the position of the peak remains essentially unaltered. This forces the unfixed peak in each case to move towards the other as the overlap increases. Therefore, for the smallest field, both peaks are observed furthest from each other, also having the deepest value of the minimum that is formed between them. Although there is no collapse onto a universal curve due to the overlap of phase transitions, the curves for the lowest field in each case could be considered as that closest to the universal curve for the phase selected for scaling. Consequently, a single rescaled curve to reconstruct the magnetocaloric response of each phase transition has been extracted from the lowest field of 0.09 T. They are marked with the orange boxes in **Figure 3.7 (a)** and **(b)**, respectively. The temperature range in the region between the two peaks is restricted to that for which the effect of each phase transition on the other is assumed to be negligible.

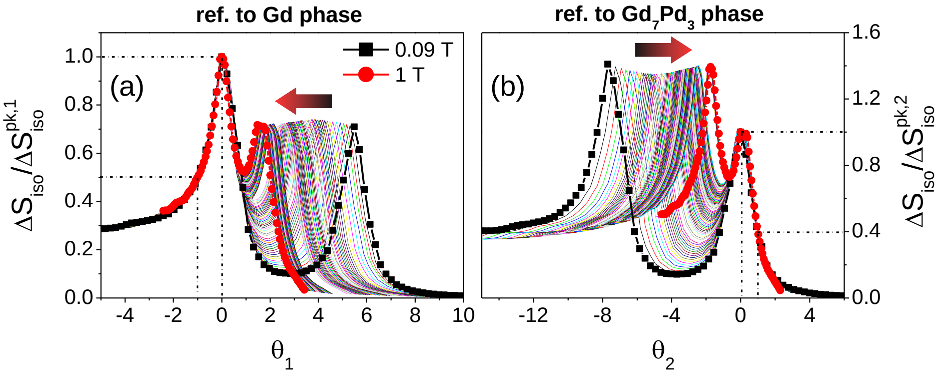

Figure 3.6. Rescaled ΔS_{iso} curves of $Gd_{80}Pd_{20}$ composite sample for magnetic fields ranging from 0.09 (black lines with square symbols) to 1 T (red lines with circular symbols) when the scaling procedure is applied to the Gd phase transition **(a)** and the Gd_7Pd_3 phase transition **(b)**. The dashed lines indicate the origin of the new θ axes and the reference temperatures used in each case.

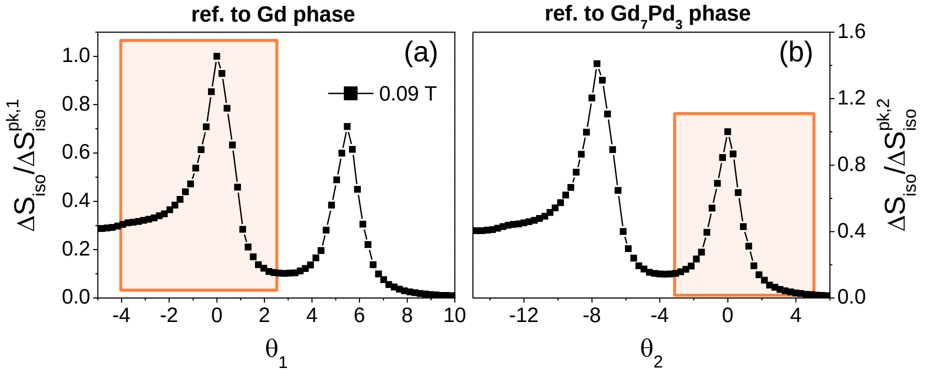

Figure 3.7. The orange boxes show the individual rescaled curve of Gd **(a)** and Gd_7Pd_3 **(b)** phase transitions extracted from the rescaled curves of the total response of $Gd_{80}Pd_{20}$ sample for 0.09 T.

3.2.2 Deconvolution procedure

The magnetocaloric responses for the different fields at the two Curie transitions can be reconstructed from the single rescaled curves in **Figure 3.7** by multiplying them with their corresponding peak values and undoing the temperature transformation via inverting **Equations (3.1)** and **(3.2)**. There are two possibilities for performing this inversion: either using the power laws that typically describe the behavior of $\Delta S_{iso}^{pk}(H)$ and $T_r(H)$ in SOPTs ($\Delta S_{iso}^{pk} \propto H^n$ and $|T_r - T_{pk}| \propto H^\tau$), or directly using the experimental values of $\Delta S_{iso}^{pk,i}(H)$ and those calculated for $T_r(H)$. **Figure 3.8 (a)** and **(b)** show the field dependence of $|\Delta S_{iso}^{pk}(H)|$ and $|T_r(H) - T_{pk}|$ in logarithmic scale for Gd and Gd_7Pd_3 phases in the composite sample, respectively. Linear fittings have been performed using the initial and final parts of each curve, demonstrating that, unlike samples with a single SOPT, the slope changes with field for both $|\Delta S_{iso}^{pk}(H)|$ and $|T_r(H) - T_{pk}(H)|$. It is noticed that the $|\Delta S_{iso}^{pk}(H)|$ of the two Curie transitions in **Figure 3.8 (a)** are relatively parallel to each other, revealing a similar evolution with the magnetic field. For $|T_r(H) - T_{pk}|$ (**Figure 3.8 (b)**), the lack of linearity is more evident in the whole magnetic field range, showing two-step behavior (low and high fields).

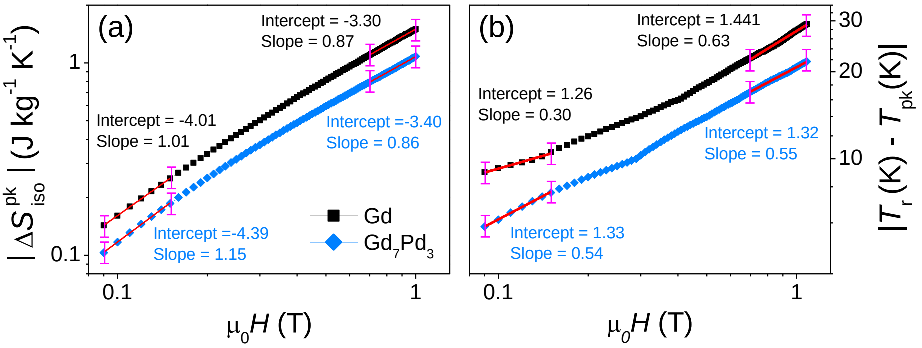

Figure 3.8. Magnetic field dependence of **(a)** $|\Delta S_{iso}^{pk}|$ and **(b)** $|T_r - T_{pk}|$ in logarithmic scale for Gd (square symbols) and Gd_7Pd_3 (diamond symbols) phases within $Gd_{80}Pd_{20}$ composite sample. The results of the linear fitting of initial and final parts of each curve are shown.

As there are no unique exponents that can be used to describe the behavior of $\Delta S_{iso}^{pk}(H)$ and $T_r(H)$ of the two phases in the whole studied field range, the reconstruction of the magnetocaloric responses was performed using: either 1) a single exponent for $\Delta S_{iso}^{pk,i}(H)$ and $T_{r,i}(H)$ extracted from the fittings for the initial fields (from 0.09 to 0.15 T) as these fields are the least affected by the overlap of the phase transitions, or 2) the experimental $\Delta S_{iso}^{pk,i}(H)$ and calculated $T_{r,i}(H)$. The comparison between the results from the two reconstruction methods could indicate how the proximity between the two Curie transitions and the increasing overlap with magnetic field affect the reconstruction procedure. Assuming no interactions between the two phases, the reconstructed responses of each of them have been added to recover the total convoluted response of the composite sample. **Figure 3.9** shows the reconstructed magnetocaloric responses of the composite sample and the experimental one for comparison for low (0.2 T) and high magnetic fields (1 T).

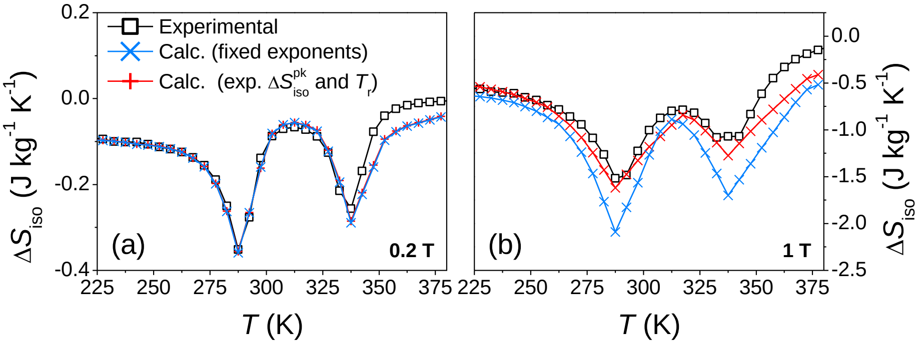

Figure 3.9. Temperature dependence of the total ΔS_{iso} of $Gd_{80}Pd_{20}$ sample for 0.2 T **(a)** and 1 T **(b)**. Square symbols: experimental values; x symbols: calculated reconstructed values from the universal curves using fixed exponents for $\Delta S_{iso}^{pk}(H)$ and $T_r(H)$; + symbols: calculated from universal curves using the experimental $\Delta S_{iso}^{pk}(H)$ and $T_r(H)$.

With respect to the reconstructed responses using fixed exponents, a good agreement is observed for low magnetic fields, as the coefficients have been obtained from the fittings in the low magnetic field region. At high fields (**Figure 3.9 (b)**), the peaks are noticeably overestimated (in absolute value). This is because the exponents for $\Delta S_{iso}^{pk,i}(H)$ and $T_{r,i}(H)$ were extracted from the fittings of the low field region, which further highlights that these magnitudes cannot be described by a single power law behavior for the entire field range. The use of the experimental $\Delta S_{iso}^{pk,i}(H)$ and $T_{r,i}(H)$ for the reconstruction also produces a response in good agreement with the experimental curve for low magnetic fields. For higher fields, the reconstructed response using the experimental values shows a better correspondence with the experimental response than the previous approach, but the predicted responses are still overestimated (**Figure 3.9 (b)**).

The $\Delta S_{iso}^{pk,i}$ assigned to each phase from the experimental curves of the composite can be overestimated as each phase transition can exhibit a non-negligible response at the peak temperature of the other due to their proximity. This effect, which would be enhanced with the increasing overlap as the field increases, is likely to be responsible for the observed discrepancy between experimental and reconstructed responses as presented in **Figure 3.9**. This is shown in **Figure 3.10,** where the experimental response of the composite is plotted together with the deconvoluted responses of Gd and Gd_7Pd_3 phases from the rescaled curves using the experimental $\Delta S_{iso}^{pk,i}(H)$ and $T_{r,i}(H)$.

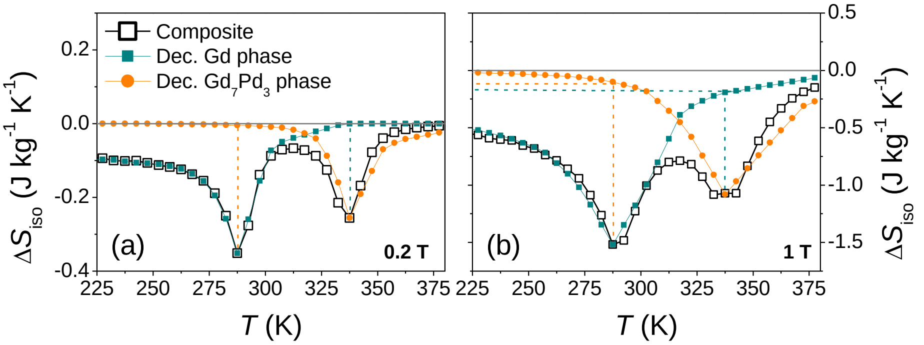

Figure 3.10. Temperature dependence of the isothermal entropy change for 0.2 T **(a)** and 1 T **(b)**. Open square symbols correspond to the experimental curves of the composite sample. Solid square symbols correspond to the reconstructed response of Gd phase by means of the universal curve using the experimental ΔS_{iso}^{pk} and T_r. Circular symbols correspond to the reconstructed response of Gd_7Pd_3 phase using the experimental ΔS_{iso}^{pk} and T_r.

The way in which the individual responses are obtained makes their peak values correspond exactly with those of the composite sample. It can be noticed that, for 0.2 T in **Figure 3.10 (a),** the contribution of each reconstructed response at the peak temperature of the other (indicated by dash lines) is virtually negligible, so both abovementioned approaches for the reconstruction work correctly due to limited overlap between the peaks. However, the cross effects become relevant for 1 T in **Figure 3.10 (b)**, being more important for Gd_7Pd_3 phase (with lower response), as previously observed. This confirms that the total reconstructed response of the composite, using either one of the two methods mentioned above, is overestimated for high fields due to the cross contributions, which prevents a direct identification of the response of each phase from the experimental results.

Therefore, two alternative procedures are proposed to remove the contribution of each phase transition at the peak temperature of the other. Both methods use the experimental $\Delta S_{iso}^{pk,i}$ and $T_{r,i}$ to undo the scaling, as mentioned above.

1. Subtraction method:
   New $\Delta S_{iso}^{pk,i}(H)$ values have been obtained by subtracting the deconvoluted response of the phase j ($j = 1,\ 2$) at the temperature of the peak of phase i ($i = 1,\ 2$) from the experimental values at the peak of phase i:

$$\begin{aligned} \Delta S_{iso}^{pk,1*}(H_j) &= \Delta S_{iso}^{pk,1}(H_j) - \Delta S_{iso}^{dec,2}(T = T_{pk,1}, H_j) \\ \Delta S_{iso}^{pk,2*}(H_j) &= -\Delta S_{iso}^{dec,1}(T = T_{pk,2}, H_j) + \Delta S_{iso}^{pk,2}(H_j) \end{aligned} \tag{3.3}$$

   These new peak values and previous experimental T_r of the two phases have been used to recalculate the deconvoluted responses.

2. Coefficients' method:

   The peak values of the experimental ΔS_{iso} of the composite sample correspond to a linear combination of the two deconvoluted responses using a_j and b_j coefficients for each phase:

$$\begin{aligned} \Delta S_{iso}\left(T = T_{pk,1}, H_j\right) &= a_j \cdot \Delta S_{iso}^{dec,1}\left(T = T_{pk,1}, H_j\right) \\ &\quad + b_j \cdot \Delta S_{iso}^{dec,2}\left(T = T_{pk,1}, H_j\right) \\ \Delta S_{iso}\left(T = T_{pk,2}, H_j\right) &= a_j \cdot \Delta S_{iso}^{dec,1}\left(T = T_{pk,2}, H_j\right) \\ &\quad + b_j \cdot \Delta S_{iso}^{dec,2}\left(T = T_{pk,2}, H_j\right) \end{aligned} \tag{3.4}$$

   Then, the a_j and b_j coefficients that best meet both previous conditions for each field are determined so that the vertical scale of the deconvoluted responses is modified while maintaining the shapes. These coefficients used to recalculate the deconvoluted responses are used to iteratively solve **Equation (3.4)**, i.e.:

$$\begin{aligned} \Delta S_{iso}^{dec,1\,*}(H_j) &= a_j \cdot \Delta S_{iso}^{dec,1}\left(H_j\right) \\ \Delta S_{iso}^{dec,1\,*}(H_j) &= b_j \cdot \Delta S_{iso}^{dec,2}\left(H_j\right) \end{aligned} \tag{3.5}$$

   It is observed that a second iteration of **Equation (3.4)** using the already corrected responses, give coefficients that are virtually 1 for all magnetic fields. This indicates that the experimental values at the peaks of the composite sample can be accurately reproduced as a linear combination of the initial deconvoluted responses in a single step.

In **Figure 3.11**, the new deconvoluted responses obtained by means of the two abovementioned methods have been added again to recover the total convoluted response of the composite sample and compare with the experimental curves. For a low field of 0.2 T, the two recalculated responses are in very good agreement with the experimental data, as already observed for the initial methods. When the field is increased up to 1 T, a much better correspondence is obtained after the corrections with **Equations (3.3)** and **(3.5)**. The relative difference between the peak values of experimental curves and those obtained by solving the linear combinations of **Equation (3.4)** for both low and high fields are virtually zero. In fact, this is expected as the coefficients are demonstrated to be those that meet this condition. This confirms the validity of both approaches and indicates that the coefficients calculated through **Equation (3.4)** are not arbitrary but those that compensate the cross contributions of the overlapping MCE peaks. The subtraction method, which is simpler, can also reproduce the experimental data. This implies a significant improvement with respect to the original reconstructions. In addition, after using the modified methods, not only the peak values are accurately reproduced but the shape of the curve in the temperature range between them is properly described.

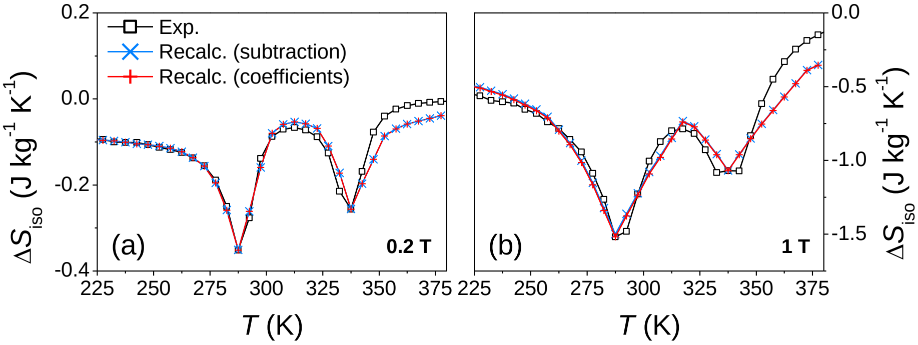

Figure 3.11. Temperature dependence of the total ΔS_{iso} of composite sample for 0.2 T **(a)** and 1 T **(b)**. Square symbols: experimental values; x symbols: reconstructed response using the corrected $\Delta S_{iso}^{pk}(H)$ with the subtraction method of **Equation (3.3)** ; + symbols: reconstructed response using the corrected $\Delta S_{iso}^{pk}(H)$ with the coefficients' method of **Equation (3.4)**.

3.2.3 Calculation of the phase fraction

It has been shown that the magnetocaloric response of the composite is the result of the addition of the individual responses of the constituent phases, confirming that they are independent and non-interacting. This implies that the total magnetization of the composite sample, M_T, is also the sum of the magnetizations of each phase independently, M_i, weighed with the mass fractions of each of them, f_{mi}:

$$M_T(T,H) = f_{m1} \cdot M_1(T,H) + f_{m2} \cdot M_2(T,H). \tag{3.6}$$

Therefore, the use of the Maxwell relation to compute the isothermal entropy change of the composite sample gives:

$$\begin{aligned} \Delta S_{iso}(T,H) &= f_{m1} \cdot \Delta S_{iso,1}(T,H) + f_{m2} \cdot \Delta S_{iso,2}(T,H) \\ &= \Delta S_{iso,1}^{dec}(T,H) + \Delta S_{iso,2}^{dec}(T,H) \end{aligned} \tag{3.7}$$

where $\Delta S_{iso,1}$ and $\Delta S_{iso,2}$ are the isothermal entropy change per unit mass of pure Gd and Gd_7Pd_3 phases, respectively.

This implies that, if the response of the individual phases per unit mass is known, the ratio of the deconvoluted response of each phase and the response of the pure phase would directly yield the mass fraction of the phase in the composite, i.e., $\Delta S_{iso,i}^{dec}/\Delta S_{iso,i} = f_{mi}$. In the current case of a biphasic composite, doing this for one of the phases would be enough for the estimation of the phase distribution of the material as $f_{m1} + f_{m2} = 1$.

To estimate the phase distribution of this composite material through the deconvoluted magnetocaloric responses, the peak value of the deconvoluted response of Gd phase has been compared with that of pure Gd, which is widely available in the literature. For this comparison, the initial deconvoluted response of Gd phase by using the experimental ΔS_{iso}^{pk} and those after the corrections of **Equations (3.3)** and **(3.5)** have been used. The calculated mass fraction of Gd phase, which is slightly dependent on the magnetic field, is plotted in **Figure 3.12** together with the Rietveld refinement results (47 wt. %, according to **Table 3.2**). The three calculated mass fractions through the deconvoluted magnetocaloric responses keep close to the value experimentally determined from XRD, with a maximum difference of approximately 3 wt. % when using the uncorrected deconvoluted response. The results from this uncorrected response show a growing trend with increasing field and this is related to the previously mentioned overestimation of the magnetocaloric response for larger fields due to the additive contribution of Gd_7Pd_3 phase. The results from the corrected deconvoluted responses using the subtraction and the coefficients methods (i.e., using **Equations (3.3)** and **(3.5)**, respectively) show better correspondence with the reference value from the XRD (with a maximum difference around 1 wt. % for the lowest fields), also removing the relatively large dependence with the magnetic field.

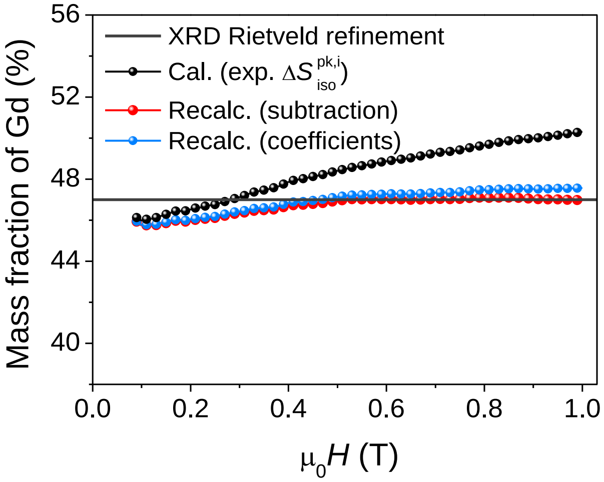

Figure 3.12. Mass fraction of Gd phase in $Gd_{80}Pd_{20}$ composite sample as a function of the magnetic field. The solid gray line represents the phase fraction (47 wt. %) obtained from Rietveld refinement. Sphere symbols indicate the results from the comparison of the magnetocaloric responses of pure Gd and the deconvoluted response of Gd phase using: the experimental ΔS_{iso}^{pk} (black), the corrected ΔS_{iso}^{pk} with the subtraction method (red), and the corrected ΔS_{iso}^{pk} with coefficients (blue).

3.3 Conclusions

Multiphase magnetocaloric composites with relatively close Curie transitions and appropriate phase fractions have been shown to enhance the refrigerant capacity with respect to pure phases. This has been demonstrated by the studied series of $Gd_{100-x}Pd_x$ (x = 5, 10, 15, 20) composites, which exhibit coexistent Gd and Gd_7Pd_3 phases with Curie transitions as close as ~40 K. The phase coexistence of Gd and Gd_7Pd_3 is observed and verified by XRD, SEM and magnetocaloric results. The phase fraction of Gd_7Pd_3 is found to increase with increasing Pd content.

The study of the field dependence of the magnetocaloric effect in the form of exponent n could reveal the presence of the minor phase in composite sample $Gd_{95}Pd_5$, even when the minority Gd_7Pd_3 phase is not evident in the ΔS_{iso} curves. An RC 10 % larger than that of pure Gd has been obtained for $Gd_{80}Pd_{20}$ sample, which comprises of 42 wt.% Gd, 48 wt.% Gd_7Pd_3 (higher Curie temperature) and 10 wt. % Gd_2O_3.

A procedure based on the scaling laws of the magnetocaloric effect is proposed to deconvolute the magnetocaloric responses due to overlapping thermomagnetic SOPTs. The $Gd_{80}Pd_{20}$ composite sample is used as the model case as it represents a challenging scenario of having two overlapping transitions with very similar responses leading to unavoidable cross effects which must be taken into account. The addition of the two deconvoluted responses accurately reproduce the experimental response of the composite sample.

Finally, the deconvoluted response of Gd phase within the composite has been compared with the response of pure Gd to estimate the mass fraction of this phase, giving results in good agreement with that of the Rietveld refinement.

4 Magnetocaloric materials with overlapping first- and second-order phase transitions

Current MCE research is mainly focused on materials showing FOPT as their associated MCE is usually larger than those of SOPT. One such example is the Ni_2Mn-based Heusler alloys undergoing martensitic transition (FOPT) of martensite to austenite and vice versa. Their large inverse MCE together with non-reliance of critical elements contributes to their popularity in the community. Moreover, they can also undergo magnetic phase transitions of their martensitic and austenitic phases, thus typically offering two types of MCE of opposite signs: conventional ($\Delta S_{iso} < 0$) and inverse MCE ($\Delta S_{iso} > 0$). When all these multiple magnetic phase transitions overlap, the complexity of studying and interpreting the thermomagnetic behavior and performance of Ni_2Mn-based Heusler alloys heightens.

In this chapter, a series of off-stoichiometry Ni_2MnIn Heusler alloys is used as a model system to show different degree of overlap among their phase transitions. As the overlap between the martensitic and magnetic transitions increases, the magnetocaloric responses decrease and the tight phase transition concurrence leads to a total ΔS_{iso} with features resembling artifacts (e.g., spikes in the data). The case of more separated phase transitions also presents an unusual behavior in which the MCE due to the FOPT decreases with increasing field. The use of appropriate characterization and analysis techniques shows that these behaviors are due to the competition between the martensitic and magnetic transitions.

4.1 Concurrence of first- and second-order phase transitions in Heusler alloys

Among the Ni_2Mn-based Heusler alloys, Ni-Mn-In has been receiving the most attention (based on the annual publication counts from the search in Web of Science) for the last three years. These publications mainly dedicate to compositional studies as the performance and transition temperature selection are highly dependent on their compositions. $Ni_{0.5}Mn_{0.5-x}In_x$ with x = 0.15 to 0.16 exhibits ferromagnetic martensitic and austenitic phases [112]. Further tuning of the Ni/Mn ratio, enables the magnetostructural transformation of $Ni_{0.5-y}Mn_{0.5+y}In_{0.15}$ to occur near room temperature [113]. Hence, with the aim of studying the phase complexity of Ni_2MnIn family and its relation to their MCE performance, a series of off stoichiometry $Ni_{49+x}Mn_{36-x}In_{15}$ Heusler alloys with varying Ni/Mn ratio is developed to tune the degree of overlap in their thermomagnetic phase transitions. This study is conducted through the analysis of the ΔS_{iso} and its field dependence, as well as through characterization techniques such as temperature XRD, calorimetry and AC susceptibility [114].

4.1.1 Synthesis and microstructural details

A series of five polycrystalline off-stoichiometric full Heusler alloys with nominal compositions $Ni_{49+x}Mn_{36-x}In_{15}$ (x = 0, 0.5, 1, 1.5 and 2) was prepared by arc melting in argon atmosphere then annealed in vacuum at 1123 K for 72 h for improved homogenization. These samples were supplied by US Army Research Laboratory. The measured composition of the samples, presented in **Table 4.1** together with their electron per atom (e/a) ratio, was obtained using EDX equipped on a field emission scanning electron microscope (Zeiss Ultra 55 FE-SEM). Subsequently, the samples will be denoted by their e/a ratio.

XRD measurements at room temperature were performed on ground samples using a Rigaku D-Max B Diffractometer with Cu K_α radiation. Prior to the measurements, the powdered samples were subjected to heat treatment at 823 K in vacuum for 6 h to remove the residual stress induced by grinding.

The XRD results reveal that, except for e/*a* 7.826 and 7.839 alloys, all other samples exhibit single monoclinic 7M modulated martensite. The e/*a* 7.826 sample exhibits $L2_1$ austenitic structure while e/*a* 7.839 sample shows a coexistence of austenitic and martensitic phases.

Table 4.1. Compositions of the alloys from the series $Ni_{49+x}Mn_{36-x}In_{15}$ measured through EDX and their corresponding electron per atom ratio, e/a, used as sample designation from now on.

Nominal composition	Measured composition	e/a ratio
$Ni_{49}Mn_{36}In_{15}$	$Ni_{48.1}Mn_{36.5}In_{15.4}$	7.826
$Ni_{49.5}Mn_{35.5}In_{15}$	$Ni_{48.6}Mn_{35.9}In_{15.5}$	7.839
$Ni_{50}Mn_{35}In_{15}$	$Ni_{49.5}Mn_{35}In_{15.5}$	7.865
$Ni_{50.5}Mn_{34.5}In_{15}$	$Ni_{50.4}Mn_{34.4}In_{15.2}$	7.902
$Ni_{51}Mn_{34}In_{15}$	$Ni_{49.8}Mn_{34.8}In_{15.5}$	7.874

4.1.2 Evolution of thermomagnetic phase transitions along the series

Figure 4.1 shows the $M(T)$ curves of the studied samples measured with a maximum magnetic field of 1.5 T. Various magnetization changes that emerge from different and concurrent phase transitions are observed for the samples, although the different features are easily distinguishable only for the samples with the lowest electron per atom ratio, i.e., e/a of 7.826 and 7.839. Upon heating, these two samples show: (1) a magnetization decrease due to the Curie transition of the low temperature martensitic phase, (2) which is followed by an abrupt magnetization increase arising from the magnetostructural transformation from martensite to ferromagnetic austenite with larger magnetization, (3) subsequently followed by a magnetization decrease due to the Curie transition of the newly formed austenitic phase. It is observed that the martensitic transition shifts to higher temperatures with increasing e/a ratio. In the case of the other alloys, this trend is less evident due to the lower increase of magnetization associated to the formation of the austenite.

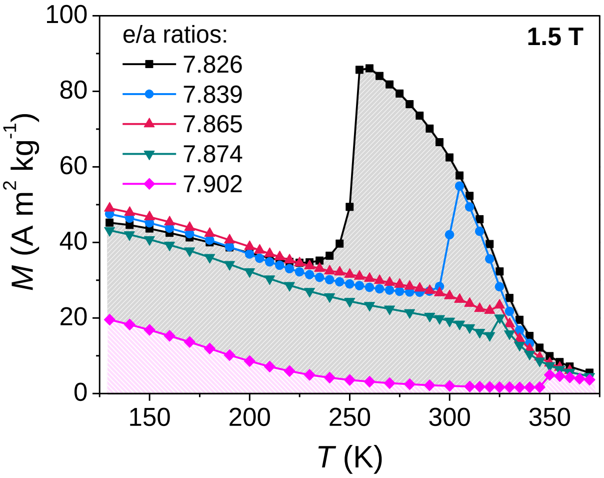

Figure 4.1. $M(T)$ curves upon heating of the alloys of the studied series for an applied magnetic field of 1.5 T.

Figure 4.2 shows the temperature dependence of ΔS_{iso} of the alloy series for a magnetic field change of 1.5 T. Due to the hysteresis associated to FOPT, magnetization measurements were conducted using the discontinuous measuring protocol detailed in **Chapter 2**.

For sample e/a 7.826, the isothermal entropy change peaks are related to the magnetization changes described previously. The small negative ΔS_{iso} values in the range 150–200 K arise from the slight magnetization decrease observed at low temperature due to the uncompleted Curie transition of the martensitic phase (T_C^M) (that, in this case, occurs at temperatures higher than the start of the martensitic transition). Above 210 K, the responses due to the two main transitions in the sample are observed: a large positive peak (colored in blue) due to the martensitic transition (210 – 250 K), followed by another negative response, well defined in this case, due to the Curie transition of the austenitic phase (T_C^A). Among this series, sample e/a 7.826 shows the largest inverse MCE with an adiabatic temperature change of ΔT_{ad} = -4.15 K for 1.76 T [115]. As the e/a ratio increases in this alloy series, the ΔS_{iso} curves get more significantly affected by the increased proximity between the martensitic transition and the Curie transition of the austenitic phase: the resulting two MCE responses, both conventional and inverse, become smaller as the two transitions get closer. Furthermore, the total response seems to be anomalous for samples e/a 7.865 and 7.874 in which a spike appears embedded into the high temperature conventional MCE, resembling an experimental artifact (observed around 320 K).

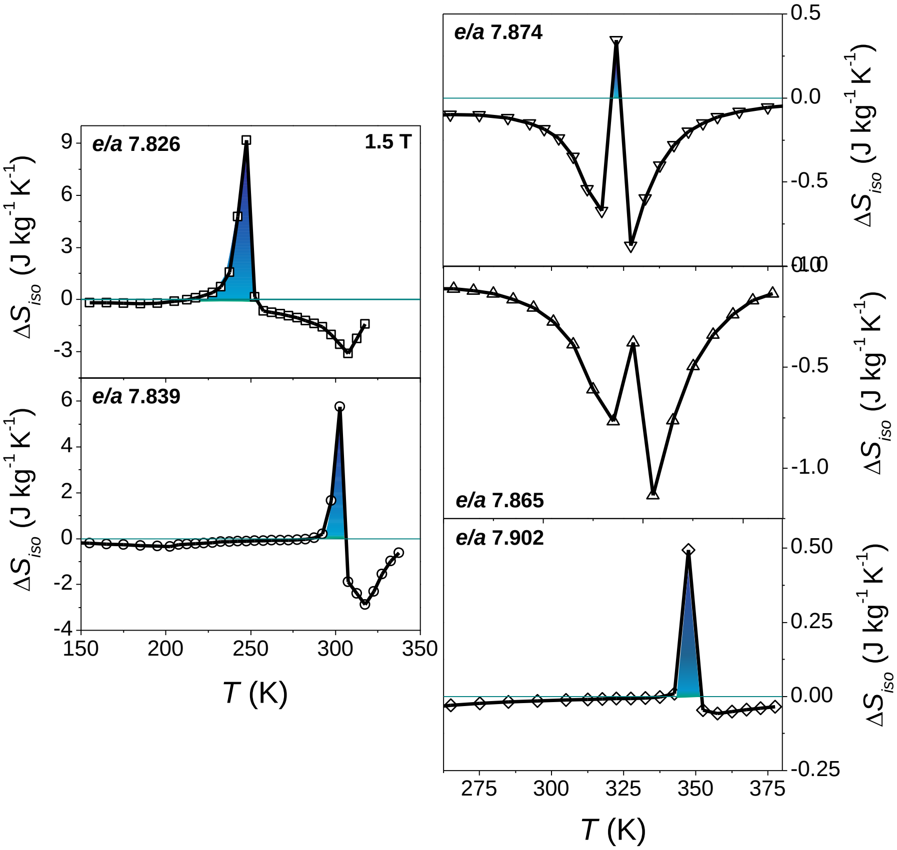

Figure 4.2. Temperature dependence of the isothermal entropy change of the alloy series for a magnetic field change of 1.5 T. The positive ΔS_{iso} (inverse MCE) peak values arising from the martensitic transition are marked with gray closed symbols to highlight the evolution of this transformation with varying e/a.

XRD experiments at temperatures above and before the appearance of the artifact-like feature in the MCE of sample e/a 7.874 were collected and sample e/a 7.826 will be the reference for comparison. **Figure 4.3 (a)-(b)** shows the XRD patterns at different temperatures of grounded e/a 7.826 and 7.874 samples using a Bruker D8 Advance diffractometer with Cu Kα radiation. For both cases, single cubic L21 structure (*Fm-3m* space group) corresponding to austenitic phase is observed at 363 K. The peak indexed with an asterisk has been found to correspond to the Ni reflections, coming from the nickel-plated copper sample holder. The low temperature patterns (210 K and 133 K for samples e/a 7.826 and e/a 7.826, respectively) show the characteristic peaks of the monoclinic 7M martensitic structure (*I2/m* space group). In this case, the presence of the principal peak of the austenitic phase (at 42.5° corresponding to the 220 Bragg peak) is ascribed to minor remnants of this phase which may be accentuated by the grinding of the samples.

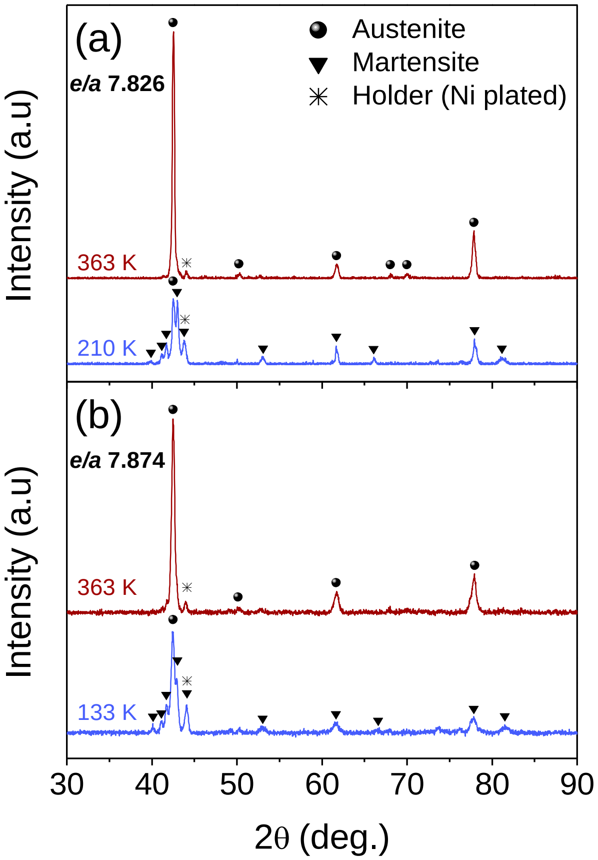

Figure 4.3. XRD patterns of powdered sample e/a 7.826 (a), and of powdered sample e/a 7.874 at 363 and 133 K (b) collected at 363 and 210 K.

The presence of the same structural transformation observed for both samples indicates that the spike observed in the MCE of sample e/a 7.874

(as well as in sample e/a 7.865) should not be an artifact but rather emerges from the martensitic transition, which entails a small magnetization change for this maximum applied field.

The occurrence of martensitic transition in all samples of the series is further confirmed through differential scanning calorimetry (DSC). The obtained T_M by means of DSC measurements (temperature of the onset of the heat flow peak) have been compared in **Figure 4.4** to those corresponding to the temperatures at the peaks of the inverse MCE for 1.5 T, $T_{pk(inverse\ MCE)}$. Even though sample e/a 7.865 does not show a positive peak, the temperature of the spike embedded into the conventional MCE is in perfect agreement with the DSC results, thus indicating that the observed spikes in samples e/a 7.865 and 7.874 are not experimental artifacts but emerge from the overlapping thermomagnetic phase transitions that produce MCE of opposite signs.

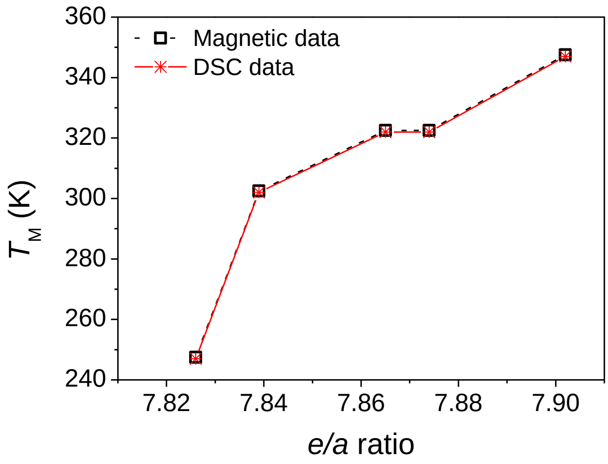

Figure 4.4. e/a dependence of the martensitic transition temperatures obtained through magnetization (square symbols) and DSC (asterisk symbols) measurements.

For sample e/a 7.902, the inverse MCE peak is observed more clearly than for e/a 7.865 and 7.874 as it does not look to be embedded into the negative values. According to its $M(T)$ curves in **Figure 4.1,** its austenitic phase forms while being nearly paramagnetic and the martensite at those temperatures, unlike for the other samples, exhibits almost zero magnetization. Therefore, a lower competition between the different transitions is observed as martensitic phase does not produce any significant MCE and the austenite forms above the temperature that would cause the maximum change of magnetization (its Curie transition).

4.1.3 Magnetic field as a control parameter of the overlap between concurrent first- and second-order phase transitions

It was previously shown in **Chapter 3** that for materials with two overlapping Curie SOPTs, the overlap between phase transitions increases with higher fields due to the broadening of the transitions and a very small field dependence of the peak [116]. However, in the case of a combination of FOPT and SOPT, the magnetic field can act as a deconvoluting agent. In fact, the applied field favors the stabilization of the magnetic phase, shifting the austenite formation to start at lower temperature, while the MCE from the Curie transition tends to broaden towards higher temperatures. In order to illustrate the effect of the magnetic field on the overlap of the two transitions and to clarify the convoluted situation in sample e/a 7.874, the AC susceptibility technique has been used due to its suitability to detect magnetic phase transitions even in the presence of negligible applied magnetic field. Measurements were performed with the ACMS II option of a PPMS using an oscillating excitation of 0.5 mT amplitude and 10 kHz frequency, in the presence of different applied DC magnetic fields.

The temperature dependence upon heating of the normalized real (χ') and imaginary (χ'') components of the AC susceptibility for samples e/a 7.826 and 7.874 are presented in **Figure 4.5** (the former sample acts as the reference).

For zero applied magnetic field, sample e/a 7.826 shows an abrupt increase in both components (which are very similar to each other) that reaches a maximum at ~260 K, followed by a sharp decrease at ~315 K, wherein the former feature indicates the occurrence of the martensitic transition while the latter the Curie transition of the austenitic phase. It is noticed that the abrupt decrease in χ'' due to the Curie transition is preceded by a small increase. This peak observed at ~200 K is related to intermartensitic transitions. When increasing the bias magnetic field up to 1 T, the changes in the real component are much more gradual than those for zero field, while the imaginary component allows a clearer identification of the phase transitions: the start of martensitic transition has shifted approximately -5 K and the feature related to the Curie transition of the austenite seems to be extended to higher temperatures. Therefore, both types of phase transitions appear more separated with increasing magnetic fields. Once the features in the components of the AC susceptibility due to the different phase transitions are identified for sample e/a 7.826, it is more straightforward to proceed with sample e/a 7.874.

For zero field, sample e/a 7.874 shows a single feature in both χ' and χ'' at ~315 K, resembling the previously identified Curie transition. This suggests that the FOPT is masked, as indicated above. When increasing the field to 1 T, various features are now distinguished in χ'': an increase due to the martensitic transition at ~325 K, followed by a gradual decrease related to the Curie transition of this newly formed austenitic phase. For a bias field of 5 T, the χ'' curve shows that the martensitic transformation to austenite has shifted to lower temperatures (~320 K) and that the effect of the Curie transition of this phase becomes more gradual. These indicate that the observed transition at ~315 K for zero field corresponds to the ferro to paramagnetic transition of the martensitic phase, with the austenite being formed above 325 K (the observed T_M for 1 T), temperature at which it is already paramagnetic. The magnetic field, therefore, acts as a control parameter that promotes the formation of the austenitic phase in its ferromagnetic state, shifting the T_M to lower temperatures, which compensates the shift caused by larger e/a. It is important to remark that there are three overlapping phase transitions in sample e/a 7.874: the Curie transition of the martensite (SOPT), the martensitic transition (FOPT), and the Curie transition of the austenite (SOPT), which set a complex and interesting scenario for further studies.

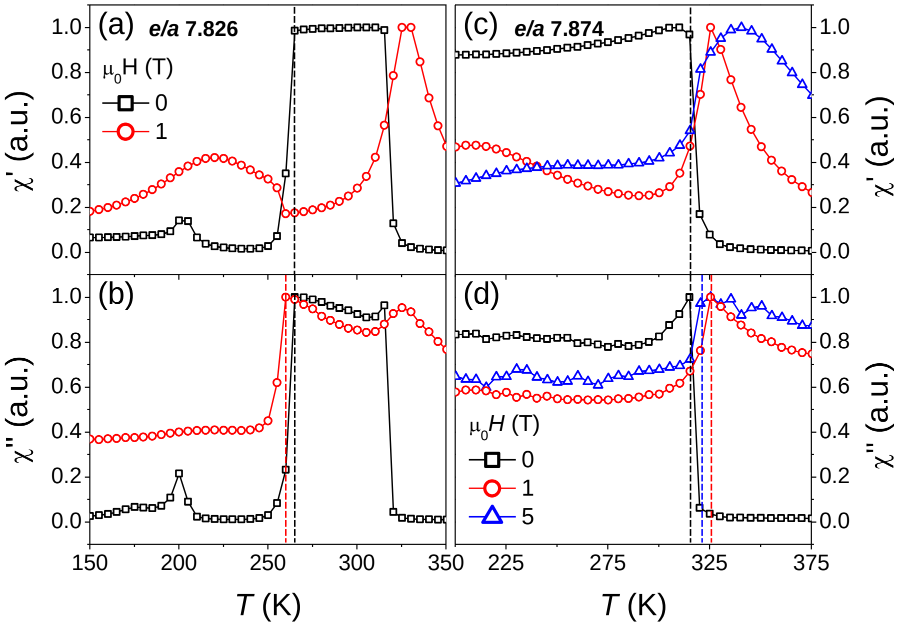

Figure 4.5. Temperature dependence for selected magnetic fields of: (a) normalized real (χ') and (b) imaginary parts (χ'') of the AC susceptibility of e/a 7.826 sample; (c) χ' and χ'' of e/a 7.874 sample. The feature related with the occurrence of the martensitic transition is indicated as dashed lines in the χ'' curves.

Motivated by previous findings, the magnetic and magnetocaloric behavior of these two samples were further investigated at a larger magnetic field using the VSM option of a PPMS reaching a maximum field of 9 T. **Figure 4.6 (a)-(b)** shows the $M(T)$ curves for different fields up to 9 T of the two samples. It is clearly observed that the martensitic transition in the two samples shifts to lower temperatures with increasing fields. The onset of the martensitic transition (determined as the maximum of dM/dT) shows a linear dependence with the magnetic field in sample e/a 7.826 with a slope of -8.10 K T^{-1}. For an improved definition of the transformations in sample e/a 7.874, measurements were performed using a fine temperature step in the region of the martensitic transition. The response of the FOPT is very subtle for low fields and it becomes recognizable in the plotted $M(T)$ curves for high magnetic fields starting at ~1 T. In this sample, for low fields, the structural transformation into austenite occurs after the Curie point of this phase. Therefore, the magnetization increase is not as large as that observed for sample e/a 7.826, whose maximum value for 9 T is roughly half of that for the latter. In this case, the effect of the magnetic field shifting the martensitic transition to lower temperatures is less significant: the average shift is -1.25 K T^{-1}. The reason for the different field dependence behavior in sample e/a 7.874 is that the magnetic field does not have much capacity to stabilize the austenite phase since the increase in magnetization that occurs with the structural transformation into austenite is not significant.

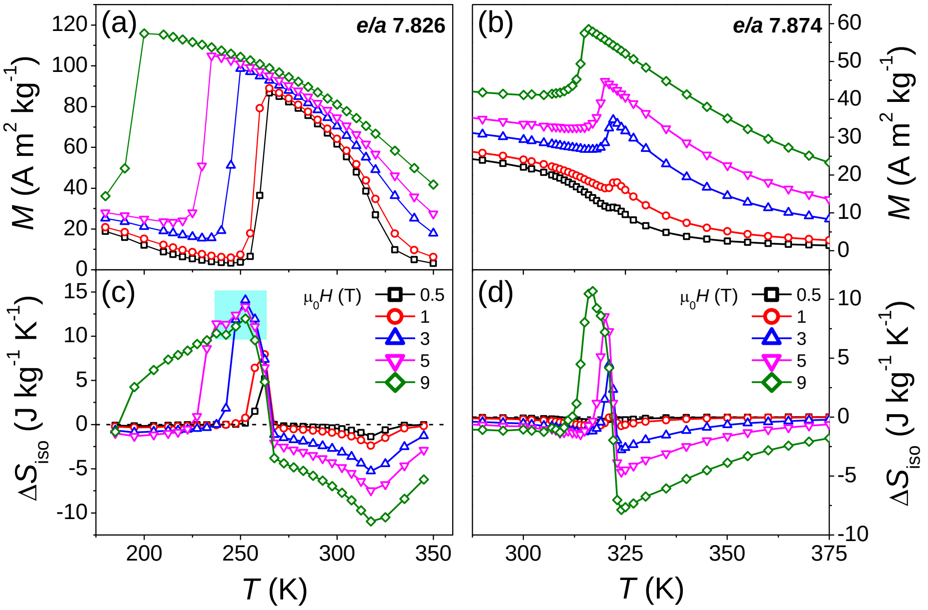

Figure 4.6. (a)-(b) Temperature dependence of the magnetization for different fields for samples e/a 7.826 and 7.874, respectively. **(c)-(d)** Temperature dependence of the isothermal entropy change for samples e/a 7.826 and 7.874. Cyan box in **(c)** highlights the anomalous decrease of the values at the peak of the FOPT.

Figure 4.6 (c)-(d) shows the $\Delta S_{iso}(T)$ curves for different magnetic field changes of samples e/a 7.826 and 7.874, respectively. For sample e/a 7.826 at fields larger than 3 T, a decrease in the peak values of the inverse MCE due to the FOPT is observed with increasing field (highlighted in cyan in **Figure 4.6 (c)**). It is known that the peak values of the ΔS_{iso} due to a FOPT can saturate for magnetic fields above that for which the transition is completed. Consequently, this observed decrease is not expected. When increasing magnetic field, this anomalous decrease is accompanied by a noticeable overlap between the positive ΔS_{iso} values arising from the martensitic transition and the subsequent conventional MCE due to the Curie transition of the austenitic phase. This is similar to the previous observation of the overlap between multiple SOPTs studied in **Chapter 3**, where the response due to each phase transition is affected by the response of the other before it can reach values close to zero. Based on the abovementioned results of sample e/a 7.826, it is reasonable to infer that the decreased peak values of the inverse MCE are not due to a measurement artifact (e.g., due to sample breaking or detachment from the holder), but it rather originates from the overlap of phase transitions that produce competing ΔS_{iso}. On the other hand, the different transitions in sample e/a 7.874 become distinguishable in the ΔS_{iso} curves for increasing fields, as observed in the $M(T)$ curves, being the positive ΔS_{iso} due to the martensitic transition clearly defined from 3 T in **Figure 4.6 (d)**.

4.1.4 Determination of the order of the phase transitions

It has been shown in **Chapter 3** the high sensitivity of the field dependence of the MCE in the form of exponent n to show evidence of multiple phase transitions. The exponent n will be investigated in samples e/a 7.826 and 7.874 showing a different degree of overlap between the FOPT and the relevant Curie transition of the austenitic phase. This recently proposed method to determine the order of thermomagnetic phase transitions [89] has been applied and compared to the conventional Banerjee's criterion in the convoluted situation of sample e/a 7.874.

To correlate the features of the exponent n curves with the characteristics of the corresponding ΔS_{iso}, **Figure 4.7 (a)-(b)** shows the temperature dependence of exponent n together with ΔS_{iso} of samples e/a 7.826 and 7.874, respectively. For sample e/a 7.826, n is close to 1 at low temperatures and changes abruptly when increasing temperature due to the switching of ΔS_{iso} from negative to positive values (region shaded in green at ~210 K), then n increases up to values higher than 2 in the region of the FOPT (orange region between 235 and 245 K), which is followed by another abrupt change when ΔS_{iso} switches from positive to negative values. In the region of the Curie transition of the austenitic phase, a minimum of n is observed at the peak temperature of this SOPT, after which n begins to increase as the paramagnetic region of the sample is reached. In sample e/a 7.874, the same features are recognized although in this case they are closer to each other due to the tight overlap of phase transitions: the abrupt change of n firstly observed at low temperatures is caused by the change of ΔS_{iso}, immediately after an overshoot of $n > 2$ is observed due to the FOPT (orange region), followed by another abrupt n decrease due to the next switching of sign of ΔS_{iso}.

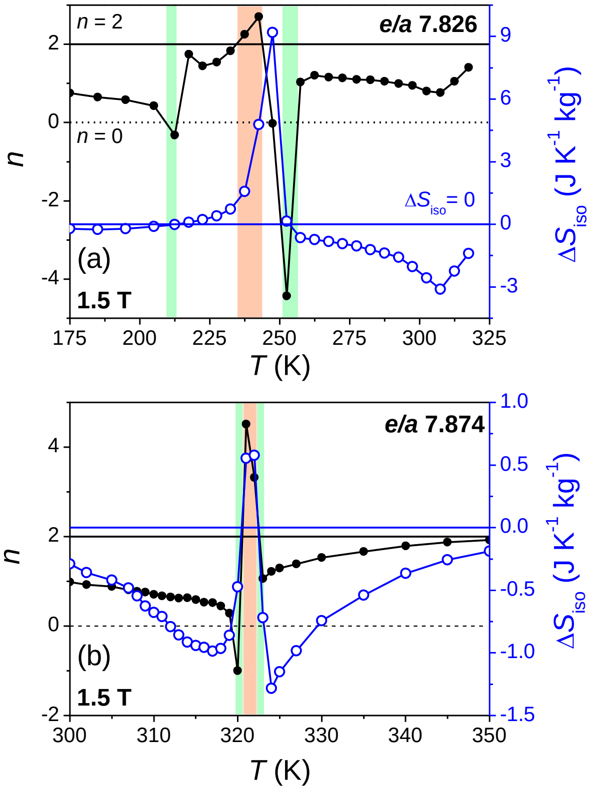

Figure 4.7. (a)-(b) Temperature dependence of exponent n (left y-axis) and ΔS_{iso} (right y-axis) for samples e/a 7.826 and 7.874 for 1.5 T, respectively. Green regions indicate the changes in n caused by the change in ΔS_{iso} signs. Orange regions highlight the overshoot of $n > 2$ related to the occurrence of the FOPT.

Therefore, the applicability of the overshoot criterion of $n > 2$ for the determination of the order of phase transitions is proven even in the intricated situation of tightly overlapping phase transitions in sample e/a 7.874.

Figure 4.8 shows the Arrott plots of sample e/a 7.874 from 310 K (black circle symbols) to 325 K (red circle symbols) with 1 K step interval, obtained from the magnetization measurements performed up to 9 T. Negative slopes can be observed for some of the curves, further confirming that the sample undergoes FOPT according to the Banerjee's criterion. However, this is not evidenced in the Arrott plots for low magnetic fields until reaching ~5 T in the curve corresponding to 319 K (blue circle symbols). The tight overlap of phase transitions of different order in this sample makes the Banerjee's criterion less efficient as large fields have to be reached. This points out the higher sensitivity of exponent n in determining the order of a thermomagnetic phase transition.

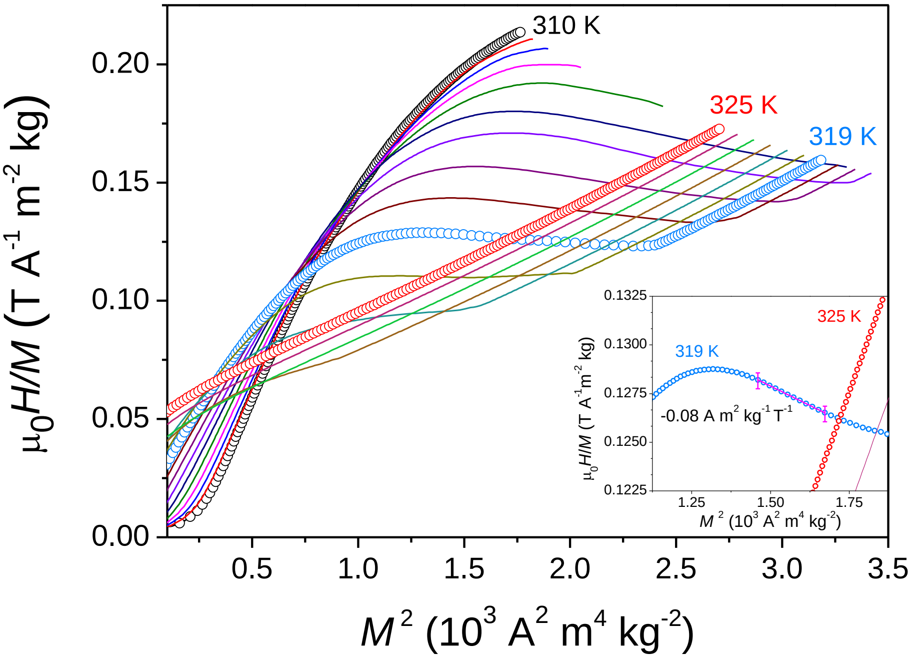

Figure 4.8. Arrott plots of sample e/a 7.874 at selected temperatures within the region in which the various phase transitions take place. The inset presents the magnified area of the curve corresponding to 319 K for which an evident negative slope is first observed for the lowest field of ~5 T.

4.2 Deconvolution of magnetocaloric responses of concurrent first- and second-order phase transitions

Although sample e/a 7.826 shows the most separated martensitic and magnetic transitions among the studied series, their relative distance is not enough to avoid their overlap. The overlap in this case seems to increase with increasing magnetic fields, being the most likely cause of the observed decrease in the inverse MCE (cyan region in **Figure 4.6 (c)**). As the MCE corresponding to the Curie transition of the austenitic phase is relatively well defined, a modification to the proposed deconvolution procedure (**Chapter 3**) has been used to deconvolute the first- and second-order phase transitions of sample e/a 7.826 [117]. The elimination of the reconstructed response of the SOPT from the total MCE of the alloy would separate the contribution from the FOPT.

4.2.1 Scaling procedure

The main difference with the method previously presented for SOPTs is that the scaling procedure in this case cannot be applied to each of the phase transitions as only the Curie transition is of second-order type. The total $\Delta S_{iso}(T)$ curves for the different magnetic fields have been rescaled by normalizing them with respect to the corresponding peak value of the Curie transition of the austenitic phase, $\Delta S_{iso}^{pk,C}(H)$, and using a reference temperature, $T_r(H)$, at a temperature lower than this peak to transform the T-axis to the θ variable:

$$\theta = (T_{pk,C} - T)/(T_r - T_{pk,C}), \tag{4.1}$$

where $T_{pk,C}$ is the peak temperature of the Curie transition. The reference temperature of the scaling has been chosen following that $\Delta S_{iso}(T_r) = 0.5\Delta S_{iso}^{pk,C}$. These rescaled curves for various magnetic fields are presented as a function of θ in **Figure 4.9**.

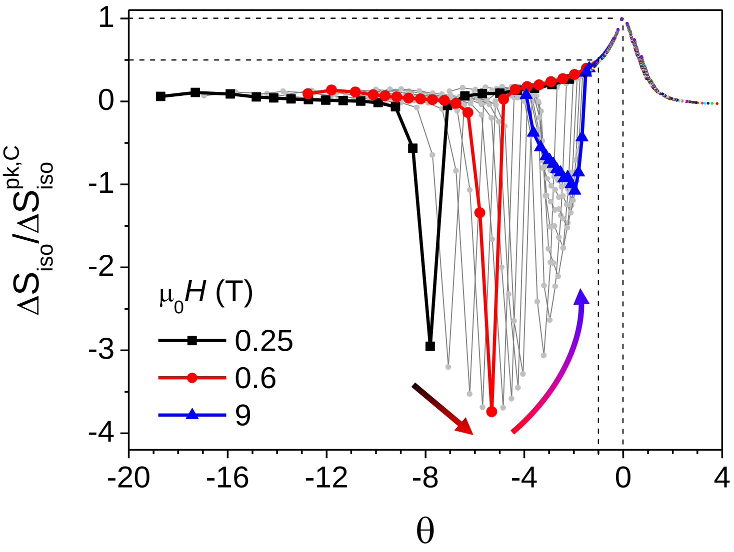

Figure 4.9. Rescaled curves of the total ΔS_{iso} response of sample e/a 7.826 obtained by applying the scaling to the response of the Curie transition of the austenitic phase. Dashed lines indicate the reference temperature, T_r, ($\theta = \text{-}1$ for $\Delta S_{iso}(T_r) = 0.5 \cdot \Delta S_{iso}^{pk,C}$) and the peak temperatures where the origin of the θ axis is placed ($\theta = 1$ for $\Delta S_{iso}(T_r) = \Delta S_{iso}^{pk,C}$).

The peaks corresponding to the two magnetocaloric responses in **Figure 4.9** appear inverted as they have been normalized using the negative $\Delta S_{iso}^{pk,C}$. The rescaled curves for all the magnetic fields from 0.25 T to 9 T using a step of 0.025 T are plotted in colored symbols for the range $\theta > \text{-}1.5$ to show the good collapse in this region, in which the SOPT is not affected by the FOPT for all magnetic fields. In the region of the martensitic transition (i.e., $\theta \leq \text{-}1.5$), not all the curves are plotted so that the different features can be distinguished easily. When increasing the magnetic field from its minimum value, the peak values from the FOPT increase at a higher rate, in absolute value, than those of the SOPT (which are fixed at 1). However, for 0.6 T (indicated in **Figure 4.9** as red) and above, this behavior is inverted and the rate of increase of the FOPT with respect to the SOPT progressively gets smaller, eventually decreasing. For 9 T, the peak values corresponding to the FOPT and SOPT are very similar to each other. This is due to the saturation of the height of the ΔS_{iso} peak due to a FOPT from a certain field that causes the completion of the transformation, while that of the

SOPT does not. It is also noticed that the two magnetocaloric responses get closer with increasing field, similar to the previously studied case of overlapping SOPTs, despite being different in nature (FOPT vs. SOPT) and tend to shift in different temperature directions with increasing field. The reason for the increasing overlap is that the MCE from the Curie transition increases in width towards lower temperatures (reflected on the used T_r), which occurs at a higher rate than its peak shifts to higher temperatures and the peak from the FOPT shifts towards lower temperatures. It is also due to the cumulative character of the ΔS_{iso} curves as deduced from the properties of the definite integral (**Equation (1.2)**), i.e., a ΔS_{iso} curve for a magnetic field change ($\Delta H_1 = H_1 - H_0$) contains the curves corresponding to smaller magnetic fields changes ($\Delta H_2 = H_2 - H_0$, with $H_2 < H_1$). Therefore, the shift of the start of FOPT to lower temperatures with increasing field makes that the low temperature extremum of the ΔS_{iso} peak moves to lower temperatures while its high temperature end remains at the same position, as observed in **Figure 4.6 (c)**. In the case of the ΔS_{iso} due to the Curie transition, the low temperature end shifts to lower temperatures while the high temperature one towards higher temperatures.

Therefore, to avoid as much as possible the distortions due to the phase overlap, the single rescaled curve of the Curie transition has been extracted from the rescaled curves for the lower magnetic fields. Various rescaled curves in the range 0.25 – 0.8 T have been selected to construct the universal curve with an appropriate number of points as shown in **Figure 4.10**. The curve in **Figure 4.10** covers the full temperature range of the Curie transition as it reaches values near zero at both sides of the peak. This would allow the prediction of the MCE from the Curie transition at the peak temperatures of the MCE corresponding to the FOPT and thus ascertain the influence of the overlap on the observed anomalous decrease in peak values of the inverse MCE with increasing magnetic field.

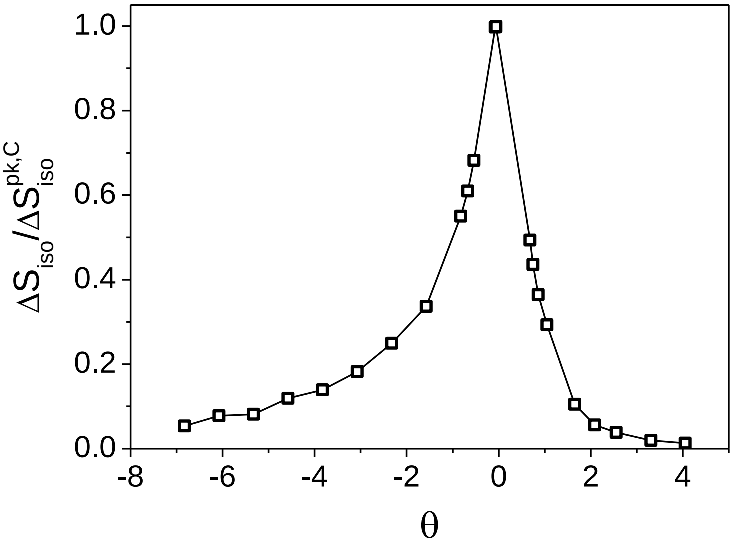

Figure 4.10. Universal curve of the ΔS_{iso} response of the austenitic phase in sample e/a 7.826 that has been formed from various rescaled curves in the low field region.

To check the feasibility of using power laws to describe the magnetic field dependence of $|\Delta S_{iso}^{pk,C}|$ and $|T_r - T_{pk,C}|$ in this case, these two magnitudes are plotted vs. magnetic field in logarithmic scale in **Figure 4.11**.

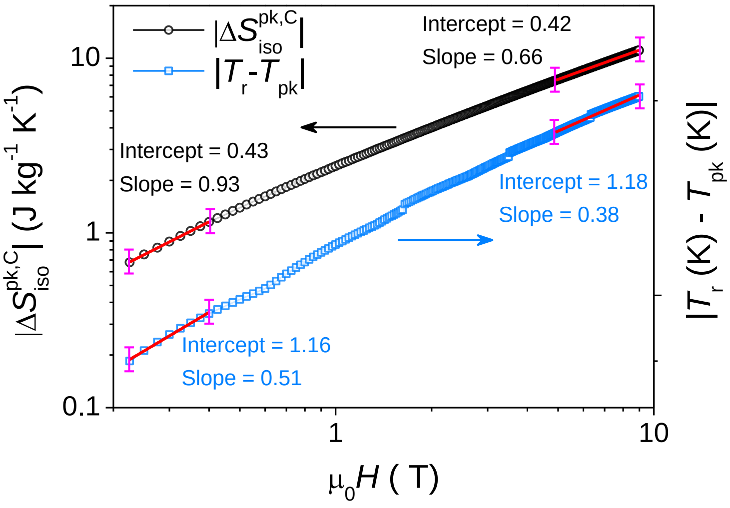

Figure 4.11. Field dependence of $|\Delta S_{iso}^{pk,C}|$ and $|T_r - T_{pk}|$ resulting from the scaling of the Curie transition of the austenitic phase.

The slopes obtained by linear fitting for low and high fields in the log-log plot indicate that these two magnitudes cannot be described by a single power law for the entire field range. Therefore, the phase overlap also, in this case, cancels the validity of the power laws. Accordingly, the MCE from the Curie transition has been reconstructed by multiplying the universal curve in **Figure 4.10** by the experimental $\left|\Delta S_{iso}^{pk,C}(H)\right|$ and undoing the x-axis transformation by reverting **Equation (4.1)** with the $T_r(H)$ extracted from experimental data. However, it has to be noted that the full temperature range of the extracted universal curve for low fields will enable the reconstruction of the complete response of this transformation for high fields, where a significant part is not experimentally observable due to the overlap of phase transitions.

Figure 4.12 (a) shows the temperature dependence of the experimental ΔS_{iso} curves, together with the reconstructed response from the Curie transition for various magnetic fields. This graph allows to appreciate the good agreement between the reconstructed and experimental curves in the region of the SOPT unaffected by the FOPT (from $T > 270$ K), where only minor deviations are noticed at the largest temperatures for the highest magnetic field. These minor discrepancies do not influence the goal of performing the reconstruction as they are located the furthest away from the FOPT. These observed deviations are only due to the fact hat scaling is performed by using the low field universal curve, without a reference temperature above the peak, to reconstruct the high field data, and not to any other phase transition.

In the region of the positive ΔS_{iso} values due to the FOPT ($T < 270$ K), the reconstructed MC response emerging from the Curie transition increases with increasing magnetic field, constituting a relevant fraction of the total ΔS_{iso} for the highest field. It is therefore evident that the two opposite MCEs compete, resulting in an apparently diminished response from the FOPT. Finally, the reconstructed Curie responses for the various fields have been subtracted from the corresponding experimental curves and the results are presented in **Figure 4.12 (b).**

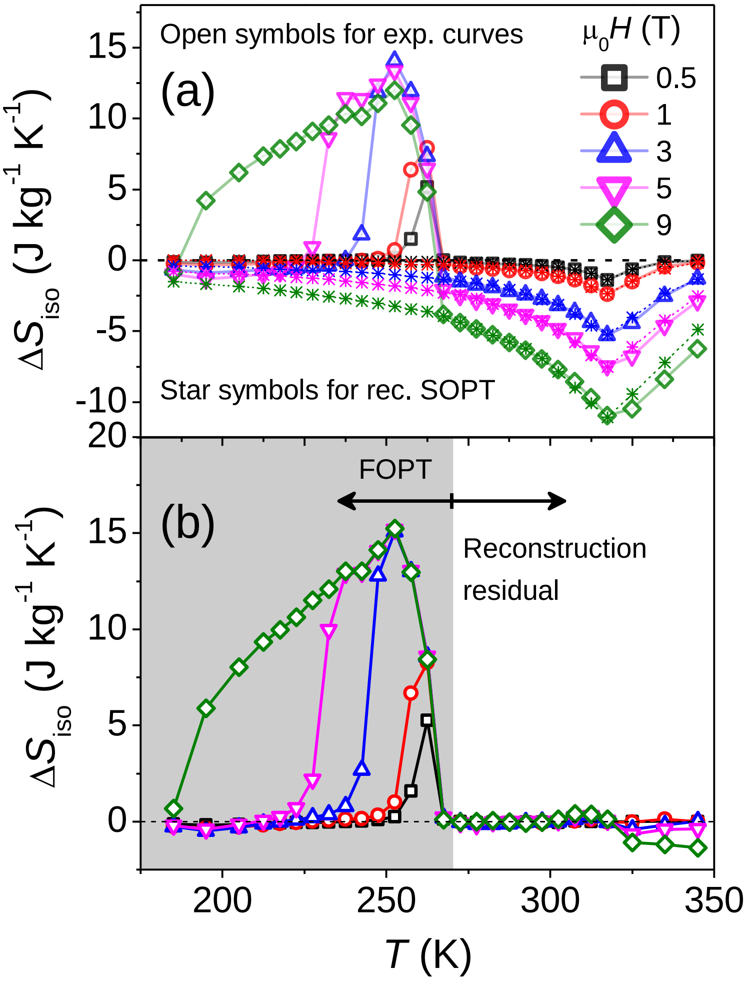

Figure 4.12. (a) Temperature dependence of experimental ΔS_{iso} (open symbols) and reconstructed ΔS_{iso} of the Curie transition of the austenitic phase (asterisk symbols) for different magnetic field changes. **(b)** Results from the subtraction of reconstructed Curie transition from the total experimental response for the different magnetic fields. The shaded gray part corresponds to the deconvoluted response from the FOPT and the right region is considered as the residual of the reconstruction of the SOPT.

This time, two different temperature regions are distinguished in **Figure 4.12 (b)**: the shaded part in gray ($T <$ 270 K) corresponds to the deconvoluted MCE due to the martensitic transition, while on the right side of this gray box is the residual of the experimental minus reconstructed emerging from the Curie transition. The deconvoluted MCE from the martensitic transition now shows the typical behavior from FOPTs, with values that saturate at a certain magnetic field change and do not decrease with further increase in the magnetic field. Therefore, it is confirmed that the origin of the anomalous decrease of the maximum in the inverse MCE from the FOPT is due to the competition between the opposite magnetocaloric responses of the overlapping FOPT vs. SOPT. On the other hand, the residual remains around zero except at temperatures above ~320 K for fields higher than 3 T.

4.3 Conclusions

The effects of the overlap of thermomagnetic phase transitions producing opposite magnetocaloric responses have been investigated with a series of $Ni_{49+x}Mn_{36-x}In_{15}$ (x = 0, 0.5, 1, 1.5 and 2) Heusler alloys. The different compositions show a different relative distance between a first-order martensitic transformation, producing positive ΔS_{iso}, and the Curie transition of the high temperature austenitic phase, with conventional negative ΔS_{iso} values. The total MCE due to both types of phase transitions decrease as they approach each other. The competition between the two individual responses produces features that resemble experimental artifacts in the ΔS_{iso} curves for samples e/a 7.865 and 7.874, whose phase overlap is the tightest. The temperature and field dependence of the martensitic transformation and the details of the overlap were analyzed through AC susceptibility for applied bias fields from 0 to 5 T. The comparison of the susceptibility results for sample e/a 7.874 for different fields reveals that, for zero bias field, the austenitic phase is formed while being paramagnetic. For increasing field, the martensitic transformation occurs before the completion of the magnetic transition of the low temperature martensite, being then concurrent with the Curie transition of the austenite.

The field dependence of the MCE in the form of the exponent n has been studied in the complex scenario of sample e/a 7.874, with three overlapping phase transitions. The recently developed criterion to determine the order of thermomagnetic phase transitions has been applied in this case, finding that it is possible to discern the occurrence of the FOPT for relatively low fields, surpassing the sensitivity of Banerjee's criterion.

However, the phase overlap leads to anomalous observations, not only when the phase transitions are tightly overlapped but also in the case in which they are more separated. Sample e/a 7.826 shows a decrease in the positive ΔS_{iso} values when magnetic field increases above 3 T. Using the universal scaling laws of the MCE obtained from the situation where the sample exhibits the least phase overlap, the MC response from the Curie transition of the austenitic phase has been reconstructed for the full temperature range. The predicted response of the Curie transition has been subtracted from the total MCE of the alloy, allowing the deconvolution of the contribution exclusively due to the first-order martensitic transformation. It is confirmed that the anomalous decrease of the inverse MCE with high magnetic fields is due to the competing MCE response from the Curie transition.

5 Study of thermal hysteresis of magnetocaloric materials using TFORC

Thermal hysteresis in MC-FOPT materials may be an important drawback as it reduces the usable MCE under thermal cycling. In particular, it has recently been shown that $(NiMnSi)_{0.66}(Fe_2Ge)_{0.34}$ alloy undergoing magneto-structural transition with a giant ΔS_{iso} exhibits a negligible reversible response due to its large thermal hysteresis [37]. Moreover, a large thermal hysteresis can lead to a misinterpretation of the type of the phase transition that the material undergoes [37]. A more complete understanding of thermal hysteresis and the mechanisms that produced it is therefore required, for which the development of a specific characterization method is needed. The FORC method is frequently used for the study of the magnetic field hysteresis, and it has been recently applied to the case of thermal hysteresis in magnetocaloric FOPT materials [101,102]. However, at that early stage the so called TFORC method was limited to fingerprinting the thermal hysteresis, as the theoretical background that supports the interpretation of conventional (field) FORC cannot be directly extrapolated to the thermal case. More recently, an extensive work used the simulated magneto-elastic transformation of $La(Fe,Si)_{13}$ type alloys to identify the features of TFORC distributions and associate them to different characteristics of the hysteretic transformation [103]. In this chapter, a combination of experimental and simulated results has been employed to characterize the thermal hysteresis in Ni-Mn-In Heusler alloys using the TFORC technique. The proposed model for the magneto-structural transition of these systems allows to associate the features of the experimental TFORC distributions to the characteristics of the hysteretic thermomagnetic behavior of the alloys [104].

5.1 Experimental characterization of thermal hysteresis in $Ni_{50}Mn_{34}In_{16}$ Heusler alloys using the TFORC method

The TFORC technique has been applied to two Ni-Mn-In Heusler alloys with small compositional differences that produce a shift of the magneto-structural transformation of ~10 K, while the Curie transition of the austenite remains the same for the two alloys. As the martensitic and Curie transitions in these alloys are close to each other, the small shift of the FOPT allows to analyze the effects of the proximity of the two types of phase transitions. Additionally, these alloys show non-monotonic martensitic transformation with different transformation rates, which will likely have an influence in the TFORC distributions, making this Ni-Mn-In Heusler system a good candidate as model case for the TFORC study.

5.1.1 Synthesis and compositional details

Two polycrystalline Ni-Mn-In Heusler alloys were produced by IMEM-CNR, Parma (Italy), using arc melting under argon-controlled atmosphere from high purity elements. The alloys were designed to have slightly different final composition close to the nominal stoichiometry $Ni_{50}Mn_{34}In_{16}$. For this, the elements for the two alloys were weighed to match the mentioned stoichiometry except for Mn that was added with slightly different excess amounts: +3 wt.% for sample S1 and +1.5 wt.% for sample S2. The resulting ingots from arc melting were flipped and remelted several times to ensure a good homogeneity prior to an annealing under argon-controlled atmosphere at 1073 K for 72 h. To finish the annealing treatment, the alloys were water quenched.

The compositions of the two alloys were determined by EDX (energy-dispersive X-ray) analysis. The obtained compositions are presented in **Table 5.1** together with the sample designation and the corresponding e/a ratio.

Table 5.1. Measured compositions from EDX of the two alloys and the corresponding e/a ratio.

	Measured composition	e/a ratio
S1	$Ni_{49.42}Mn_{34.35}In_{16.23}$	7.8334
S2	$Ni_{49.65}Mn_{34.19}In_{16.17}$	7.8434

5.1.2 Magnetic and magnetocaloric characterization

Figure 5.1 (a)-(b) shows the temperature dependent magnetization curves upon heating and cooling (right and left branches, respectively) of samples S1 and S2 for different applied fields.

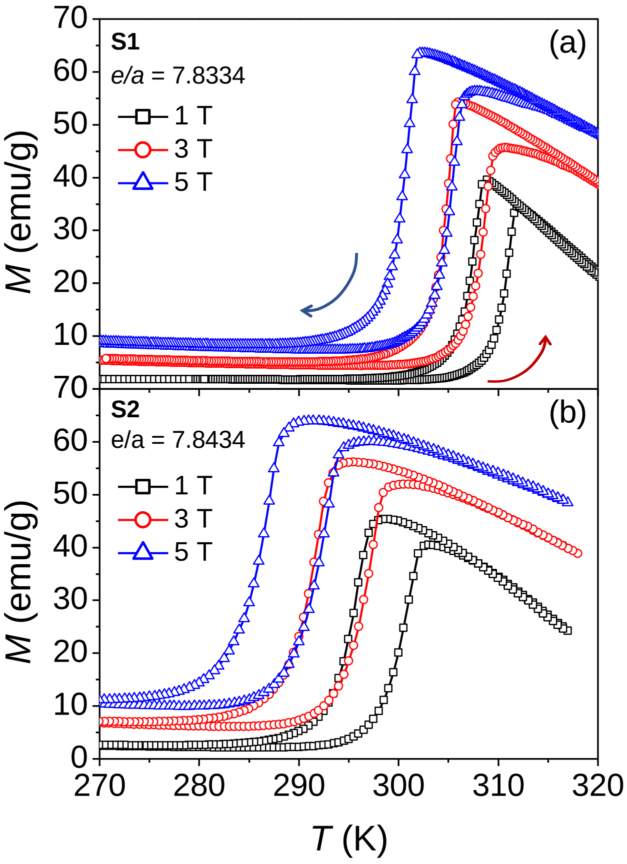

Figure 5.1. (a)-(b) $M(T)$ upon heating and cooling for magnetic fields of 1, 3 and 5 T of samples S1 and S2, respectively.

Upon heating, both samples show a magnetization increase due to the martensitic transformation from martensite to ferromagnetic austenite, which is followed by a magnetization decrease due to the Curie transition of the austenitic phase. When cooling back to the initial temperature, the martensitic transformation is shifted to lower temperatures, revealing the typical hysteretic behavior of FOPTs. The martensitic transformation shifts to lower temperatures with increasing field both for heating and cooling. This is due to the previously commented capacity of the magnetic field to stabilize the austenitic phase with larger magnetization. The behavior of these two new samples is similar to the one observed in samples with e/a 7.826 and 7.839 of the series studied in **Chapter 4**. The main difference is that the low temperature martensitic phase shows a very low magnetization in the alloys studied in this chapter and that the sample with the lower e/a ratio has lower martensitic transition temperature. Furthermore, the small compositional difference between S1 and S2 causes them to have virtually the same Curie temperature (312.5 and 313.0 K for samples S1 and S2, respectively) with an appreciably different martensitic transition (~10 K difference), with both transitions around room temperature, as intended.

Figure 5.2 shows the temperature of the martensitic transition, T_M, obtained for both samples from the maximum of dM/dT upon heating and cooling for different fields. An approximately lineal variation of T_M with the magnetic field is obtained, with slopes of -1.5 K T^{-1} and -2.2 K T^{-1} for S1 and S2, respectively. As the heating and cooling branches of each sample are not perfectly parallel, the temperature difference between T_M upon heating and cooling has been considered as the field dependent thermal hysteresis, $\Delta T_{hys}(H)$.

For sample S1, ΔT_{hys} is 3.2 K for 1 T, increasing up to 3.9 K for 5 T. The same trend of increasing $\Delta T_{hys}(H)$ with increasing field is observed for sample S2, with values equal to 5.0 and 6.0 K for 1 and 5 T, respectively. It is evident that sample S1, with lower relative distance between the martensitic and Curie transitions, has a lower thermal hysteresis. This agrees with reports indicating an increasing lattice compatibility between martensitic and austenitic structures when the structural and Curie transitions are closer to each other, resulting in a lower hysteresis [44].

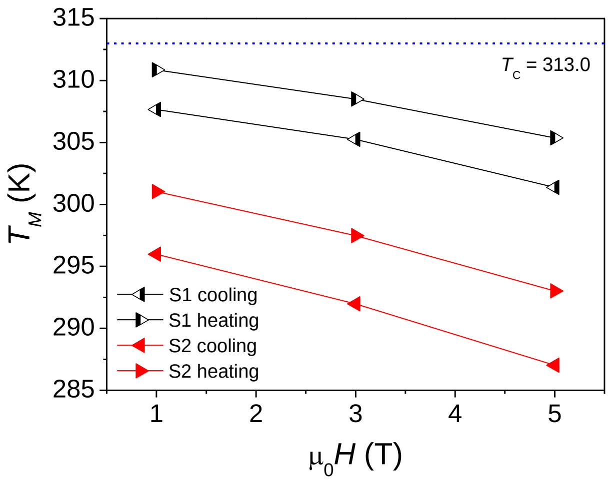

Figure 5.2. Dependence with the magnetic field of the temperature of the martensitic transition of samples S1 and S2.

Figure 5.3 shows $\Delta S_{iso}(T)$ of samples S1 and S2 for different magnetic field changes. As for other the samples undergoing FOPT studied in previous chapter, the ΔS_{iso} has been indirectly obtained through isothermal magnetization measurements using a discontinuous measurement protocol. The martensitic transformation produces large inverse ΔS_{iso} responses around room temperature, with peaks values as high as 11.85 and 14.30 J kg^{-1} K^{-1} for 2 T for samples S1 and S2, respectively. It is noticed that sample S1 exhibits lower MCE than S2 up to 3T, but the situation changes for higher fields, with peak values of 26.43 and 22.21 J kg^{-1} K^{-1} for 5 T for S1 and S2, respectively. On the one hand, the martensitic transition in sample S1 causes a lower total magnetization change than in sample S2, as it is closer to the Curie transition. On the other hand, as demonstrated previously, the conventional response of the Curie transition detracts from the positive ΔS_{iso} values emerging from the FOPT. This compensation effect should be higher in sample S1, with phase transitions that are more overlapped. However, the shift of T_M to lower temperatures with increasing magnetic field causes that the magnetization changes in the two samples become more similar, being virtually the same for 5 T. Under those larger fields, the response of S1 surpasses that of S2 as the former exhibits more abrupt magnetization change with the martensitic transition.

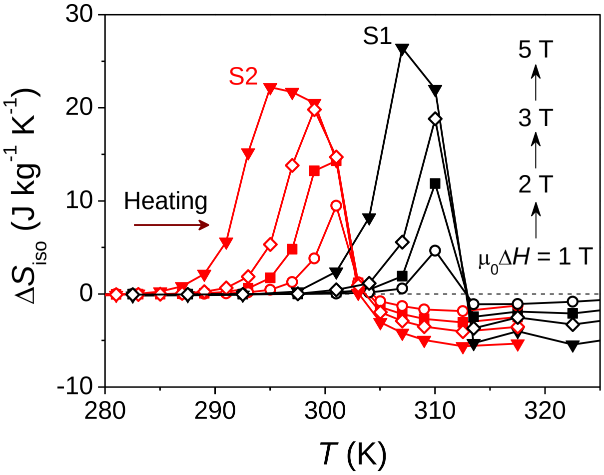

Figure 5.3. Temperature dependence of the isothermal entropy change of samples S1 and S2 for magnetic field changes of 1, 2, 3 and 5 T.

5.1.3 TFORC distributions

The experimental TFORC characterization has been focused on sample S1 due to the more overlapped martensitic and Curie phase transitions and the more abrupt magnetization changes when compared to S2, having obtained both cooling and heating distributions for different fields.

The reversal magnetization curves of sample S1 measured for 1 and 3 T are presented in **Figure 5.4 (a)-(b)**, respectively. The dashed-dotted red line, corresponding to the $T = T_{r,i}$ line, represents the heating branch that is followed to reach the different T_r from the low temperature saturation state, T_{sat}^C. These sets of reversal curves were used to calculate the TFORC distributions shown in **Figure 5.4 (c)-(d)** according to the procedure commented in **Chapter 2**. The TFORC distributions for 1 and 3 T look quite similar to each other, being the maximum height of the peak the most evident difference. In this case, the largest field shows the highest peak distribution, indicating that the magneto-structural transformation produces more abrupt magnetization changes for increasing field. There are different features, common to both distributions, that make their shapes different from the circular peak that would be the case of a totally symmetric transformation [103], namely (numbers correspond to the marks in **Figure 5.4 (c)-(d))**:

(1) a circular-shaped peak that is distorted downwards,

(2) a valley of negative values at T_u above the peak that extends towards increasing T_h, and

(3) an elongation of the peak producing a ridge approximately along the +45° direction, which appears to be delimited by the negative values mentioned above.

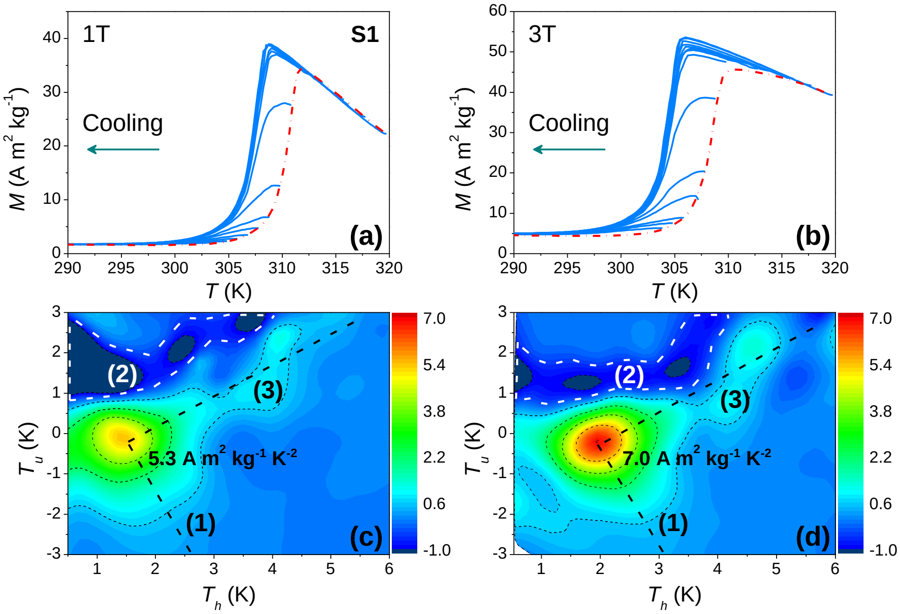

Figure 5.4. (a)-(b) Magnetization vs. temperature reversal curves upon cooling of sample S1 for 1 and 3 T, respectively. **(c)-(d)** Corresponding TFORC distributions obtained from the reversal curves for 1 and 3 T, respectively. The number in parentheses accompanied by the dashed lines indicate the main characteristics of the distribution: (1) main peak distorted downwards, (2) valley of negative values for T_u above the main peak, (3) elongation of the main peak along the +45° direction.

It is worth noting that the characteristics of the TFORC distributions are highly influenced by the path followed when going from T_{sat}^{C} to T_r, as the way back to T_{sat}^{C} depends on how the sample had transformed, i.e., the amount of the new phase formed in this process. In this sense, the elongation at +45° will be attributed in **Section 5.2.2** to differences in the reversal magnetization curves (upon cooling) that start at high T_r due to a slowdown of the structural transformation to austenitic phase near its completion along the heating branch. This feature is also evident in the M vs. T loops of **Figure 5.1** and produces an extension of the thermal hysteresis towards high temperatures. The difference between reversal curves in the region of the Curie transition in which magnetization increases upon cooling is responsible (as demonstrated in **Section 5.2.2**) for the negative $\rho(T_r,T)$ (opposite to those of the main peak). Finally, the downwards distortion of the peak can be associated (also demonstrated in **Section 5.2.2**) to differences in the reversal curves of low T_r due to a slowdown of the transformation upon cooling near its completion that extend the hysteresis down to low temperatures.

Figure 5.5 (a)-(b) show the reversal curves upon heating of sample S1 for 1 and 3 T (red lines), respectively. The path followed in this case to reach the different T_r from the high temperature saturation state, T_{sat}^{H}, is plotted with the blue dashed line. The calculated heating TFORC distributions are presented in **Figure 5.5 (c)-(d).** In this case, the TFORC distributions for the two magnetic fields also look very similar to each other but significantly different to those of the cooling mode. The difference between the heating TFORC distributions for 1 and 3 T basically lies in the height of the peak, being higher for the largest field, as observed previously in the cooling diagrams. Therefore, the magnetization changes in this case also become larger when increasing field, but with maxima of the distributions that are lower than those of the cooling mode. This can be explained by the presence of the Curie transition of the austenite, which is more overlapped with the magneto-structural transformation in heating than in cooling modes.

In comparison, the heating TFORC diagrams are less distorted from the circular shape than those of the cooling mode, with only a noticeable distortion downwards that should be associated to magnetization differences at low T for the reversal curves starting at low T_r. This is due to an interruption of the martensitic transformation when cooling (from austenite to martensite) close to the end of the process, which delays its completion. However, no relevant negative areas are observed above the peak nor any elongation of the peak along the +45° direction.

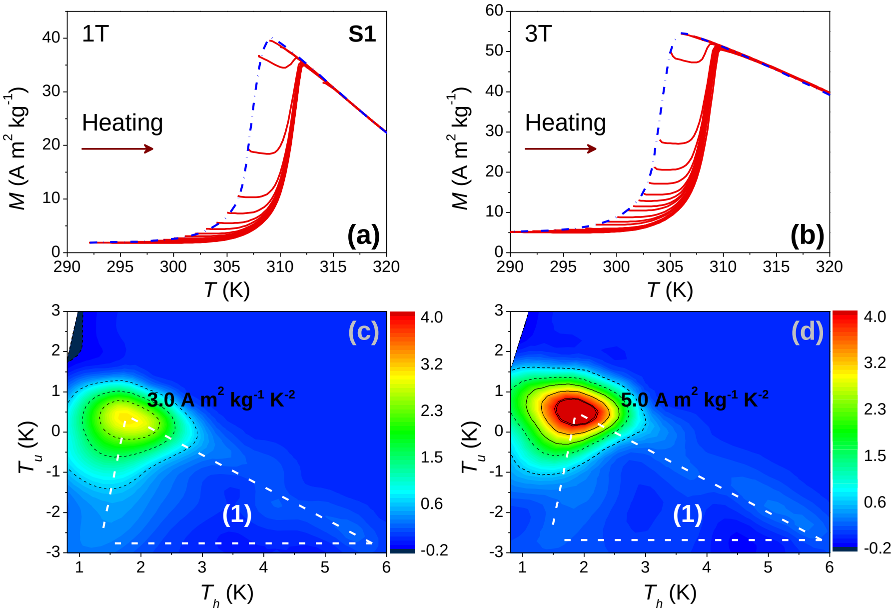

Figure 5.5. (a)-(b) Magnetization vs. temperature reversal curves upon heating of sample S1 for 1 and 3 T, respectively. **(c)-(d)**

It is expected that some of the relevant features of the TFORC distributions are associated to characteristics of the martensitic transformation near its completion along both branches. Therefore, **Figure 5.6** plots the cooling and heating full reversal curves of sample S1 for 3 T (i.e., those reversal curves starting furthest from saturation in each case, solid lines) together with the corresponding paths from saturation to those T_r (dashed lines). This will help to discern the origin of the similarities and differences of cooling and heating TFORC distributions.

Although it would be expected that both cycles overlap, there is a remarkable difference close to the completion of the martensitic transformation upon heating (highlighted with the gray box). On the one hand, when the heating branch of the FOPT is followed up to T_r in cooling TFORC, i.e., starting from T_{sat}^C where the sample is fully martensite, a slowing down of the process close to 100% of austenite causes thermal hysteresis at higher temperatures than expected. On the other hand, the major heating branch of the martensitic transformation for the heating TFORC is followed by the reversal curves which start at the lowest T_r. In this case, the previously commented deceleration of the transformation close to the end of the heating branch is not observed, which could explain the absence of the ridge along +45° in the heating TFORC contours.

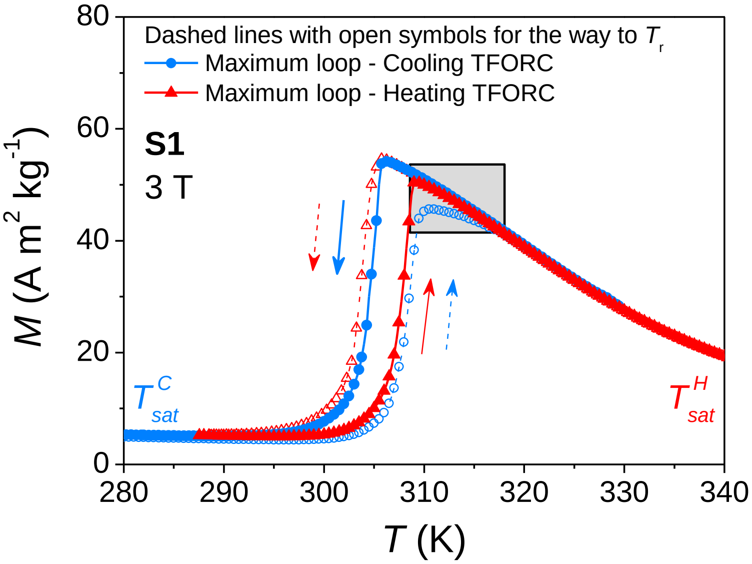

Figure 5.6. Loops corresponding to the broadest TFORC cycle in each case, i.e., that corresponding to the highest and lowest T_r for cooling and heating TFORC, respectively. Dashed lines with open symbols represent the initial path towards T_r. The grey box highlights the difference between the $M(T)$ curves near the completion of the martensitic transition upon heating.

To confirm the existence of the observed features on the cooling TFORC distributions of sample S1 and analyze the effect of the overlap between the FOPT and the Curie transition, the cooling TFORC for 1 and 3 T has been also obtained for sample S2, which has more separated phase transitions. The temperature reversal curves upon cooling of sample S2 for 1 and 3 T are shown in **Figure 5.7 (a)-(b)**, respectively, with the corresponding

TFORC distribution plotted in **Figure 5.7 (c)-(d)**. The cooling TFORC distributions of sample S2 show the same features previously commented for the case of sample S1. However, some differences can be found. In this case, both fields yield to distributions of very similar height, being lower than for sample S1. This is related to the fact that sample S1 showed more abrupt magnetization changes when the two phase transitions move away from each other with increasing magnetic field, as could also be observed in the MCE results, with larger MCE for more separated phase transitions with increasing field. Additionally, the peaks of sample S2 appear more distorted downwards with a more predominant ridge that becomes more relevant with increasing field. Moreover, the negative regions are also present in this sample above the peak, limited by the location of the ridge, but they are much less significant in sample S2, which is also related to a more separated FOPT and Curie transition.

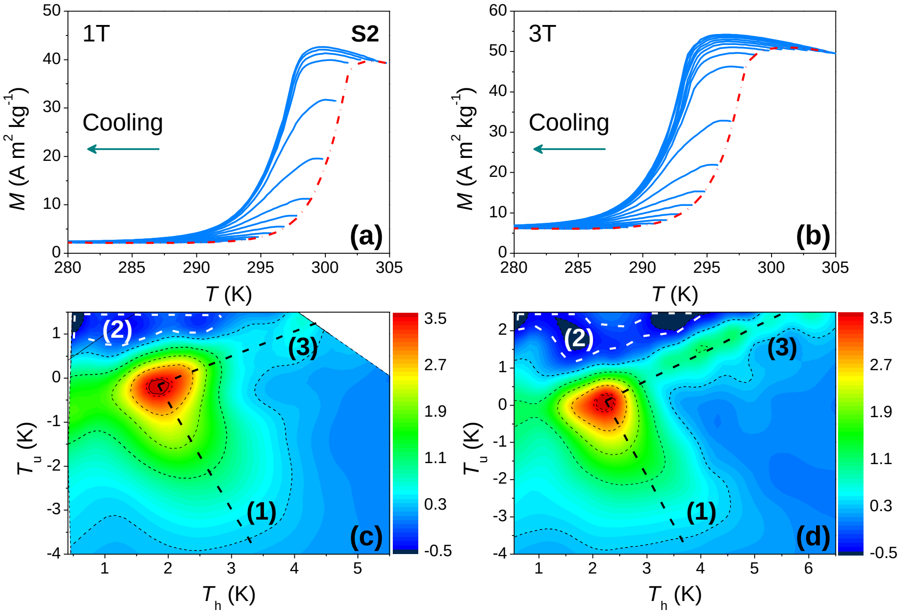

Figure 5.7. (a)-(b) Magnetization vs. temperature reversal curves upon cooling of sample S2 for 1 and 3 T, respectively. **(c)-(d)** Corresponding TFORC distributions for 1 and 3 T, respectively. (1) main peak distorted downwards, (2) valley of negative values for T_u above the main peak, (3) elongation of the main peak along the +45° direction.

5.1.4 Reconstruction of magnetization loops

The conventional (field) FORC analyses has been recently used to quantitatively recover phase-resolved magnetic hysteresis loops in materials with convoluted phases through the selective integration of the obtained distributions [118]. In this case of magnetic TFORC distributions, the deconvolution is, in principle, not possible because the different phases are not independent but transform from one to the other, being this the origin of the hysteresis.

However, the complete magnetization cycles from the TFORC measurements could be reconstructed by integrating the distributions along the full range of both original T_r and T variables. This can serve as an analysis method of the reliability of the distributions for an acquired number of reversal curves (i.e., for a number of T_r points) as well as to check the effects of applying any smoothing algorithm. Two different curves are then obtained depending on the integration variable used the TFORC distribution:

1. By integrating the distribution along T_r to obtain $f(T)$

$$f(T) = \int_0^{+\infty} \rho(T_r, T)\, dT_r, \tag{5.1}$$

   and subsequently integrating it along the T axis:

$$M_{T_r,T} = \int_0^{+\infty} f(T)\, dT. \tag{5.2}$$

   The final reconstructed curve, M_{T,T_r}, will have the same number of points as the number of T_r coordinates in the distribution, and corresponds to the branch of the transformation which is followed on the way to the different T_r. This means that it will likely be the poorest defined part of the reconstruction due to the limited number of reversal curves in this case.

2. On the other hand, the distribution is integrated along T,

$$f(T_r) = \int_0^{+\infty} \rho(T_r, T)\, dT, \tag{5.3}$$

and then along T_r:

$$M_{T,T_r} = \int_0^{+\infty} f(T_r)\, dT_r. \tag{5.4}$$

The curve, $M_{T_r,T}$, with number of points equal to those of the longer reversal curve, will correspond to the cooling or heating branch when considering cooling or heating TFORC distributions, respectively.

Figure 5.8 (a)-(b) shows the reconstructed magnetization branches of the martensitic transformation from cooling and heating TFORC, respectively. It is noted in **Figure 5.8 (a)** that the reconstructed curves from both smoothed and standard distributions produce similar results to each other that agree well with the experimental data until reaching the region of the Curie transition of the austenite. However, in **Figure 5.8 (b)** reconstructed curves obtained from smoothed TFORC distributions are noticeably underestimated while those from the raw distributions are slightly overestimated. A common feature of reconstructed curves in **Figure 5.8 (a)** and **(b)** is that they do not follow the experimental curves in the region of the Curie transition of the austenitic phase.

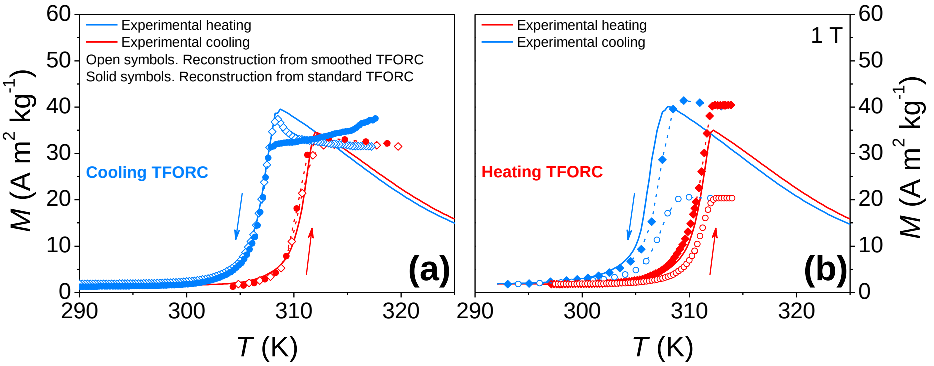

Figure 5.8 (a)-(b) Reconstructed magnetization loops of sample S1 obtained by the integration of cooling and heating TFORC distributions for 1 T, respectively.

The generalized disagreement between reconstructed and experimental curves in the region of the Curie transition could be caused by the absence of signal in the TFORC diagrams from that part of the loop, which is completely reversible and it is reduced to zero with the cross derivatives even if it has an evident temperature dependence. The need to include the reversible part to be able to recover the saturation magnetization by the full-range integration of the distributions has been reported for the case of conventional FORC distributions [119]. A similar approach is followed here, for which the reversal curves have been extended from their start to that of the longer reversal curve using their magnetization value at $T = T_r$, i.e.:

$$M^{C}_{ext}(T_r, T) = \begin{cases} M(T_r, T) & \text{if T} < \text{T}_\text{r} \\ M(T = T_r) & \text{if T} \geq \text{T}_\text{r} \end{cases}, \quad (5.5)$$

$$M^{H}_{ext}(T_r, T) = \begin{cases} M(T_r, T) & \text{if T} > \text{T}_\text{r} \\ M(T = T_r) & \text{if T} \leq \text{T}_\text{r} \end{cases}. \quad (5.6)$$

Where M^{C}_{ext} and M^{H}_{ext} are the extended magnetization for cooling and heating TFORC experiments, respectively. The extended reversal magnetizations curves obtained by applying **Equations (5.5)** and **(5.6)** to cooling and heating TFORC experiments are shown in **Figure 5.9 (a)-(b)**, respectively.

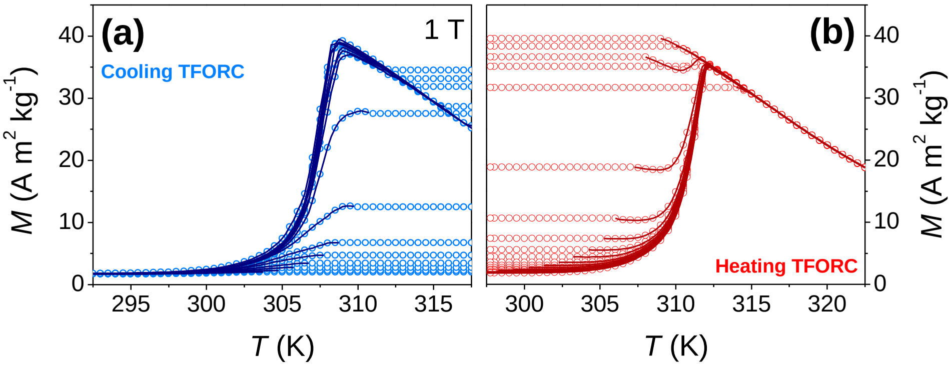

Figure 5.9. Extended reversal curves (open symbols) using the value of the magnetization data (solid lines) at $T = T_r$.

The extended reversal curves of **Figure 5.9 (a)-(b)** have been used to calculate the corresponding cooling and heating TFORC distributions by using both the direct (unsmoothed) derivatives and the polynomial fitting of Pike's algorithm. These new TFORC datasets, in turn, have been used for a new reconstruction of the complete magnetization vs. temperature loops of sample S1 for 1 T (**Figure 5.10)**. It is worth pointing out that the extensions have not influence in the resulting TFORC distributions as the derivative with respect to T vanishes along the constant extension.

Figure 5.10 (a) shows a significant improvement in the reconstruction when using the unsmoothed distributions. In this case, the region of the Curie transition of the austenite is also well reproduced, finding an almost perfect overlap between the complete experimental and reconstructed cooling curves. However, the reconstructed curves from the smoothed cooling TFORC distribution do not show an improvement with the use of the extended data and continue to noticeably fail in the fully reversible Curie transition of the austenitic phase. This is due to the effectively longer steps of T_r and T emerging from the smoothing.

The results of the reconstruction from the extended heating TFORC distributions in **Figure 5.10 (b)** show analogies with those commented previously for reconstructions of **Figure 5.10 (a)**. While the reconstructed curves from the unsmoothed distributions show an improved agreement with the original data, the reconstructed curves from the polynomial-fitted distributions are still noticeably underestimated. In this case, the reconstructions from the unsmoothed distributions do not cover a larger region of the Curie transition because of the lack of many reversal curves starting at those temperatures, which in this case correspond to those closer to T_{sat}.

Therefore, it is shown that, even if distributions are noisier, those calculated by the usual cross derivate formula (unsmoothed) produce the most accurate reconstructions of the experimental loops. It is also worth pointing out the effectiveness of the data extension to be able to recover the information from the fully reversible area of the loops. However, the use of the smoothing algorithm is justified since the main objective of the work is the qualitative study of experimental TFORC distributions. The recognized features of the TFORC distributions are present in both smoothed and unsmoothed distributions, though they can be distinguished and studied much more easily after smoothing. The measurement of a larger number of T_r curves with a lower step in the region of the transformation will make that the reconstructions after smoothing look much more like the experimental curves.

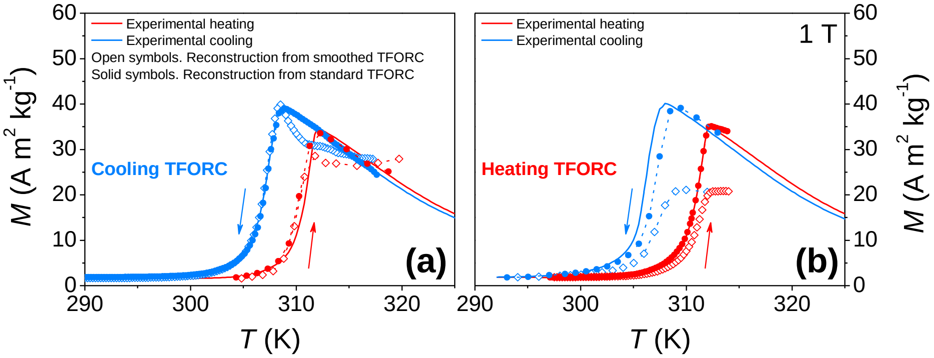

Figure 5.10. (a)-(b) Reconstructed magnetization loops of sample S1 obtained by the integration of extended cooling and heating TFORC distributions for 1 T, respectively.

5.2 Obtaining TFORC distributions from the modeled thermomagnetic behavior of the alloys

The magnetic behavior of the alloy S1 has been simulated for 1 and 3 T in order to associate the different features of the experimental TFORC distributions with the characteristics of the hysteretic martensitic transformation as well as to study the effect of the thermomagnetic behavior of the two structural phases.

5.2.1 Modeling of the various thermomagnetic phase transitions for the case of Ni50Mn34In16 Heusler alloys

The simulation of the temperature dependent magnetization curves has to be performed by using two different contributions. On the one hand, the evolution with temperature of the fraction of each phase upon a martensitic transformation has been simulated using the cumulative skewed normal distribution [120]:

$$f(T) = \frac{1}{2}\left[1 + erf\left(\frac{T-\xi}{\sqrt{2}\sigma}\right)\right] - 2O_{\mathrm{T}}\left(\frac{T-\xi}{\sigma}, \alpha\right), \tag{5.7}$$

where erf is the error function and O_T the Owen's T function. The parameters for these two functions are ξ (that indicates the location of the transformation and is related to T_M in this case), σ (scale of the normal distribution, affecting the width of the transformation) and α (shape or skewness factor). The distribution is right or left skewed depending on whether α is positive or negative, respectively. This distribution has a mean value of $\xi + \sigma\left(\frac{\alpha}{\sqrt{1+\alpha^2}}\right)\sqrt{\frac{2}{\pi}}$ and a variance of $\sigma^2(1 - \frac{2\alpha^2}{\pi(1+\alpha^2)})$. The normal distribution is recovered for zero skewness factor, i.e., $\alpha = 0$, since $O_T(\alpha = 0) = 0$. The skewed normal distribution is a phenomenological function that, among others, can describe in a relatively simple way transformations in materials that are governed by nucleation-growth processes, as occurs in martensitic transformations. As the addition of the austenite and martensite fractions (f_{Mar} and f_{Aus}, respectively) should obey that $f_{Mar} + f_{Aus} = 1$, the distribution has been applied only to obtain the fraction of austenitic phase. For a heating process, the initial fraction of austenite at temperatures well below T_M is zero, which is obtained with $f(T \ll T_M) = 0$. Conversely, when cooling, the material initially shows a single austenitic phase at temperatures well above T_M, which is obtained by defining the austenite fraction as $1 - f(T)$ in this process. Therefore, a distinction will be made between heating and cooling by separately defining the austenite fraction with respect to the initial conditions at temperatures sufficiently far from the transformation. In addition, the hysteretic behavior has been reproduced by distinguishing the parameters of the distribution (i.e., ξ, σ, and α) for heating or cooling, resulting in two transformation functions, f_{Aus}^H and f_{Aus}^C, for heating and cooling processes, respectively [103]:

$$f_{Aus}^H(T) = \frac{1}{2}\left[1 + \mathrm{erf}\left(\frac{T-\xi^H}{\sqrt{2}\sigma^H}\right)\right] - 2\mathrm{O}_{\mathrm{T}}\left(\frac{T-\xi^H}{\sigma^H}, \alpha^H\right), \tag{5.8}$$

$$f_{Aus}^C(T) = 1 - \frac{1}{2}\left[1 + \mathrm{erf}\left(\frac{\xi^C-T}{\sqrt{2}\sigma^C}\right)\right] - 2\mathrm{O}_{\mathrm{T}}\left(\frac{\xi^C-T}{\sigma^C}, \alpha^C\right), \tag{5.9}$$

where H and C superscripts refer to the heating and cooling branches, respectively.

On the other hand, considering that both martensitic and austenitic phases are ferromagnetic, their temperature dependent magnetization curves can be reproduced using the Brillouin's function [121,122]:

$$\frac{M(T)}{M_S} = \frac{2J+1}{2J}\coth\left(\frac{2J+1}{2J}\frac{g\mu_b J(H+\lambda M)}{k_b T}\right) - \frac{1}{2J}\coth\left(\frac{1}{2J}\frac{g\mu_b J(H+\lambda M)}{k_b T}\right), \tag{5.10}$$

where M_S is the saturation magnetization, g is the Landé factor, μ_B the Bohr magneton, J the total angular momentum quantum number and λ the exchange constant.

The total magnetization of the material at a certain temperature upon heating and cooling branches (M_T^H and M_T^C, respectively) can then be calculated by combining the temperature dependence of the martensitic and austenitic phase fractions and their magnetizations (M_{Mar} and M_{Aus} for the martensite and austenite, respectively):

$$M_T^H(T) = f_{Aus}^H(T)M_{Aus}(T) + f_{Mar}^H(T)M_{Mar}(T), \tag{5.11}$$

$$M_T^C(T) = f_{Aus}^C(T)M_{Aus}(T) + f_{Mar}^C(T)M_{Mar}(T). \tag{5.12}$$

The parameters for both the phase fraction and the thermomagnetic behavior of the phases have been fitted using the experimental magnetization curves of sample S1 for 1 and 3 T. The obtained parameters are presented in **Table 5.2**.

The use of α^C and α^H parameters different from 0 means that both cooling and heating processes are not symmetric, i.e., there are different rates along the transformation upon cooling and heating. The positive α^C is related to a transition that starts faster and then becomes slower, and the negative sign of α^H indicates the opposite. However, as $|\alpha^C| = |\alpha^H|$, and σ is the same for both branches, the structural transformation upon cooling and heating takes place within the same temperature range, being the heating and cooling curves identical but just separated by a distance corresponding to the thermal hysteresis [103].

The obtained parameters for the thermomagnetic behavior of austenitic and martensitic phases in sample S1 are in accordance with literature about this type of Heusler alloys [112,123,124].

Table 5.2. Parameters used for the cumulative skewed normal distribution to simulate the phase fraction of austenite for 1 T and 3 T and for the Brillouin's function to reproduce the thermomagnetic behavior of austenitic and martensitic phases.

Phase fraction	Cumulative skewed normal distribution					
	α^H	σ^H	ξ^H	α^C	σ^C	ξ^C
1 T	-10	1.5 K	313.5 K	10	1.5 K	311.5 K
3 T	-10	1.75 K	309.5 K	10	1.75 K	305.8 K
Magnetization	Brillouin's function					
	Austenite			Martensite		
M_S	$150\ \mathrm{A\,m^2\,kg^{-1}}$			$120\ \mathrm{A\,m^2\,kg^{-1}}$		
g	2			2		
J	2.5			2		
λ	$1.06 \cdot 10^6$			$9.37 \cdot 10^5$		

As an illustration of the procedure, **Figure 5.11** shows the total simulated magnetization upon cooling and heating for 1 T through the combination of the phase fraction (inset) and the magnetic behavior of the phases (dashed lines) using **Equations (5.11)** and **(5.12)**.

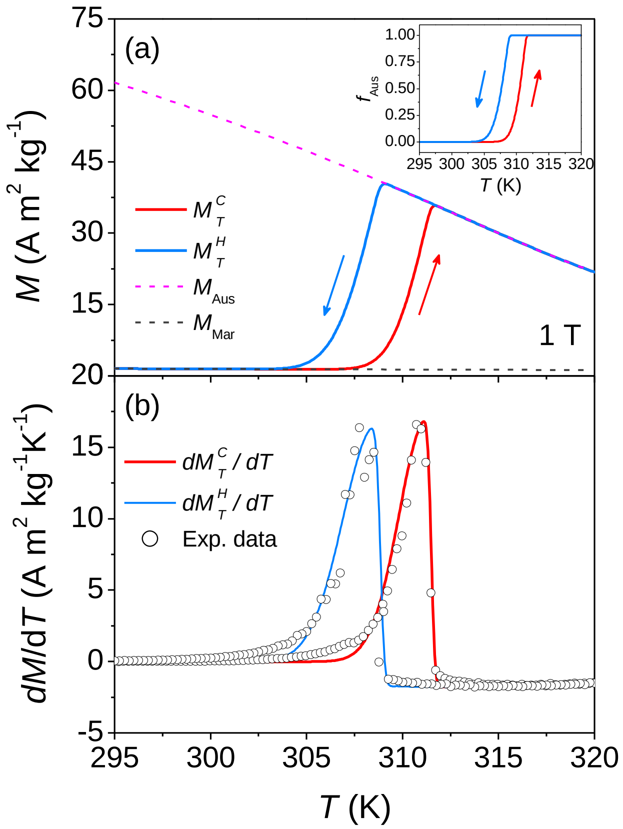

Figure 5.11. (a) Modeled thermomagnetic behavior together with the temperature dependence of magnetization of austenitic and martensitic phase. Inset: temperature dependence of austenitic phase fraction. **(b)** Derivative with respect to temperature of the modeled thermomagnetic behavior (lines) and the experimental data (symbols).

However, the observed feature in the experimental $M(T)$ curves of sample S1 in **Figure 5.6** near the completion of the transformation to austenitic phase still needs a modification of the model to be able to reproduce it. This is done by introducing a second cumulative skewed normal distribution at high austenite fraction while heating, with the meaning of a slowed down process. For the additional distribution, larger σ^H values have been used (3.75 and 8.75 K for 1 and 3 T, respectively) and, according to the fitting with the experimental full cycle loops of **Figure 5.6**, this additional process starts at 95 % of the completion for 1 T and at 86 % for 3 T. Only the new distribution is used once the selected percentage of the transformation is reached.

Figure 5.12 shows the total simulated magnetization after including the mentioned second cumulative skewed normal distribution. A slowing down of the transformation is clearly observed now for 1 and 3 T, marked with the grey boxes, similar to the observed experimentally near the complexion of the transformation to austenitic phase.

The proposed model is versatile enough to reproduce different scenarios by considering a) either just the martensitic transformation alone, or b) the total magnetization (martensitic transformation convoluted with the thermomagnetic behavior of the phases), or even c) the total magnetization including a mechanism that slows down the transformation to austenite near its completion, which has been shown to be necessary for some experimentally observed results. By separately studying the different abovementioned scenarios, it would be possible to assess the relation between the features of the experimental TFORC distributions with the characteristics of the thermomagnetic behavior of the material.

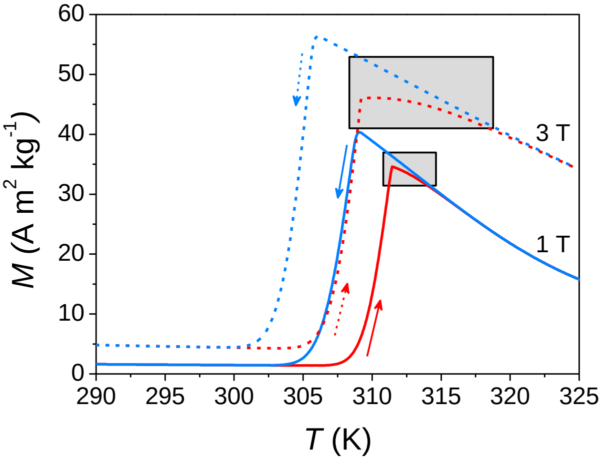

Figure 5.12. Modeled temperature dependence of magnetization for 1 and 3 T including a second process that slows down the transformation upon heating close to its completion (gray boxes).

5.2.2 Simulated TFORC distributions

Using the previously proposed model, the magnetization across each minor temperature loop can be obtained by knowing the initial fraction of each phase (which depends on the values of T_r and on which T_{sat} has been reached) and the branch of the transformation that is going to be followed with the reversal curve.

To explain the procedure, the cooling TFORC case is used as an example. In this case, the material at a generic T_r would comprise a mixture of austenitic and martensitic phases with fractions $f_{Aus}^{H}(T_r)$ and $f_{Mar}^{H}(T_r)$, respectively, obtained following the heating branch of the transformation from T_{sat}^{C} (single martensite). Along the cooling reversal curve, the existent initial fraction of martensite will remain, while the initial fraction of austenite will be transforming into martensite. Consequently, the fractions of austenite and martensite along a cooling reversal curve can be obtained as follows, respectively:

$$f_{Aus,rev}^{C}(T) = f_{Aus}^{H}(T_r) f_{Aus}^{C,renorm}(T), \tag{5.13}$$

$$f_{Mar,rev}^{C}(T) = f_{Aus}^{H}(T_r) f_{Mar}^{C,renorm}(T) + f_{Mar}^{H}(T_r). \tag{5.14}$$

These equations should satisfy that their addition is 1 at each temperature as well as that the final state at T_{sat}^{C} will be single martensitic phase.

Previous equations should fulfill three conditions:

1. Their addition is 1 at each temperature ($f_{Aus,rev}^{C}(T) + f_{Mar,rev}^{C}(T) = 1$).
2. The final state at T_{sat}^{C} will be single martensitic phase ($f_{Aus,rev}^{C}(T_{sat}^{C}) = 0$ and $f_{Mar,rev}^{C}(T_{sat}^{C}) = 1$).
3. The initial state, i.e., $T = T_r$, should be consistent with the one defined previously to the path to T_r, i.e., $f_{Aus,rev}^{C}(T_r) = f_{Aus}^{H}(T_r)$ and $f_{Mar,rev}^{C}(T_r) = f_{Mar}^{H}(T_r)$.

For these conditions to be fulfilled, the temperature-dependent functions have to be renormalized in the following way:

$$f_{Aus}^{C,renorm}(T) = 1 - \frac{f_{Aus}^{C}(T) - f_{Aus}^{C}(T_r)}{f_{Aus}^{C}(T_r)}, \tag{5.15}$$

$$f_{Mar}^{C,renorm}(T) = 1 - f_{Aus}^{C,renorm}(T) = \frac{f_{Mar}^{C}(T_r) - f_{Mar}^{C}(T)}{1 - f_{Mar}^{C}(T_r)} \tag{5.16}$$

These renormalized functions also ensure that all the initial amount of austenite transforms into martensite as $f_{Aus}^{C,renorm}(T = T_r) = 1$.

In the case of heating TFORC, the process is inverted as the initial fraction of martensite is the one that will transform to austenite during the heating reversal curves. Then, the fractions of austenite and martensite along a heating reversal curve will be obtained according to:

$$f_{Aus,rev}^{H}(T) = f_{Mar}^{C}(T_r) f_{Aus}^{H,renorm}(T) + f_{Aus}^{C}(T_r), \tag{5.17}$$

$$f_{Mar,rev}^{H}(T) = f_{Mar}^{C}(T_r) f_{Mar}^{H,renorm}(T). \tag{5.18}$$

Analogously, the renormalized temperature dependent fractions of austenitic and martensitic phases in this case of heating TFORC are:

$$f_{Aus}^{H,renorm}(T) = \frac{f_{Aus}^{H}(T_r) - f_{Aus}^{H}(T)}{1 - f_{Aus}^{H}(T_r)}, \tag{5.19}$$

$$f_{Mar}^{H,renorm}(T) = 1 - \frac{f_{Mar}^{H}(T) - f_{Mar}^{H}(T_r)}{f_{Mar}^{H}(T_r)}. \tag{5.20}$$

The thermomagnetic behavior of each phase separately follows a well-defined process, so that the magnetization due to each phase in the total system depends only on the corresponding phase fraction and the actual temperature. Therefore, the total magnetization along the minor loops for cooling and heating TFORC can be calculated by directly multiplying the temperature dependent phase fractions previously obtained times their temperature dependent magnetization, resulting in formulas analogous those of **Equations (5.11)** and **(5.12)**:

$$M_{T,rev}^{C}(T) = f_{Aus,rev}^{C}(T)M_{Aus}(T) + f_{Mar,rev}^{C}(T)M_{Mar}(T), \tag{5.21}$$

$$M_{T,rev}^{H}(T) = f_{Aus,rev}^{H}(T)M_{Aus}(T) + f_{Mar,rev}^{C}(T)M_{Mar}(T). \tag{5.22}$$

To be able to directly compare the experimental and modeled TFORC distributions, a similar number or reversal curves has been used for obtaining the simulated distributions. Additionally, the Pike's smoothing algorithm has also been applied in the case of simulated reversal curves, even though no noise is present and the smoothing is not needed. **Figure 5.13 (a)-(b)** shows the cooling and heating TFORC distributions associated to the modeled structural transformation, represented with f_{Aus}, without considering any magnetic behavior. The main peak in both cases shows a downwards distortion producing a final triangular shape that resembles the observed feature labeled with (1) in the experimental distributions of **Figure 5.4**, **Figure 5.5**, and **Figure 5.7**. This feature is therefore confirmed to be due to the asymmetry of the transformation in both cooling and heating branches. This is in agreement with results for a ferro to paramagnetic transformation upon heating [103]. No additional features are detected by modeling the martensitic transformation with just a single skewed normal distribution. The next step is to include the total magnetization into the previously calculated reversal curves, obtaining the distributions presented in **Figure 5.13 (c)-(d).** In the case of the cooling TFORC of **Figure 5.13 (c)**, a negative area above the peak is now noticeable, which indicates that the overlapping thermomagnetic behavior of the phases with temperature dependent magnetizations affects the TFORC distributions by adding extra asymmetry. In the case of the cooling TFORC distribution, the Curie transition of the austenite is the responsible of this characteristic, confirming the previous hypothesis and agreeing with the experimental results in which a sample with more separated phase transitions (sample S2) shows less negative regions in the distribution. The comparison between the phase fraction and magnetic heating TFORC distributions of **Figure 5.13 (b)-(d)** indicate that the thermomagnetic responses of the phases have a lower effect in the heating case. Only a subtle additional positive region below the peak is noticeable in the case of the magnetic distribution that is ascribed to the magnetic response of the martensitic phase, with a magnetization that remains practically invariant as shown in **Figure 5.12**. The modeled heating TFORC distributions are rather similar to the experimental ones in **Figure 5.7 (c)-(d)**. However, the modeled cooling TFORC distribution do not show the ridge along the +45° direction observed experimentally (**Figure 5.4 (c)-(d)**). The probable cause for this is that the model used so far did not incorporate the abrupt slowing down of the transformation in heating when it is about to finish.

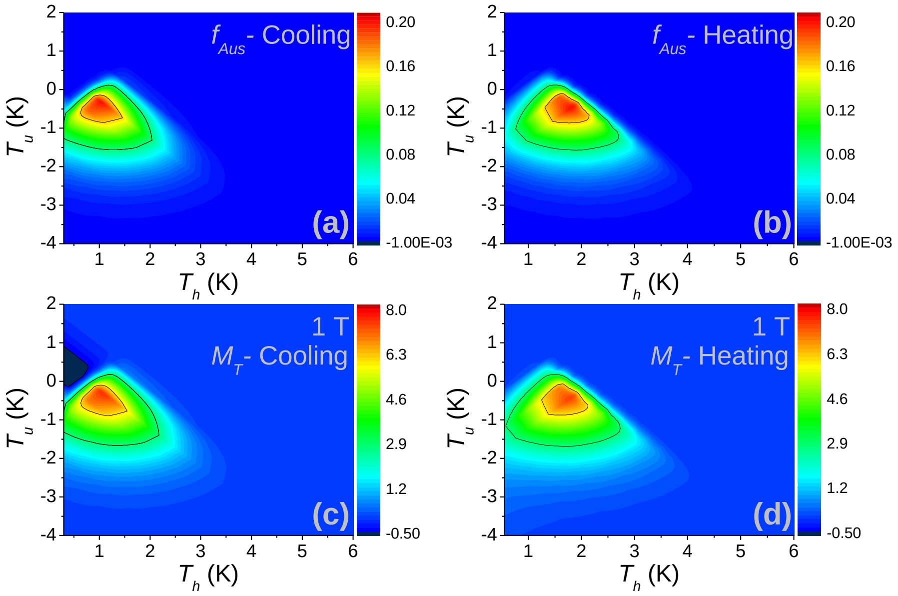

Figure 5.13. (a)-(b) TFORC distributions using the modeled austenite fraction with a single cumulative skewed normal distribution and (c)-(d) including the temperature dependent magnetization for 1 T.

To confirm this expectation, the additional process of slowing down the transformation to austenitic phase near its completion (as was shown in **Figure 5.12**) is incorporated in the cooling TFORC distributions for 1 and 3 T of **Figure 5.14 (a)-(b)**, respectively.

The modeled cooling TFORC distributions for both magnetic fields show now all the identified characteristics on the experimental ones. The downward distortion and negative areas are maintained, with the addition of an elongation along +45° like the one present in experimental distributions. Additionally, the characteristics of the modeled distributions show the same degree of importance with respect to the applied field than those of experimental distributions. While the negative area is more relevant for the lower field, due to the tighter overlap between the FOPT and the Curie transition, the ridge is more important for the higher field according to an earlier start of the interruption of the transformation during the heating process.

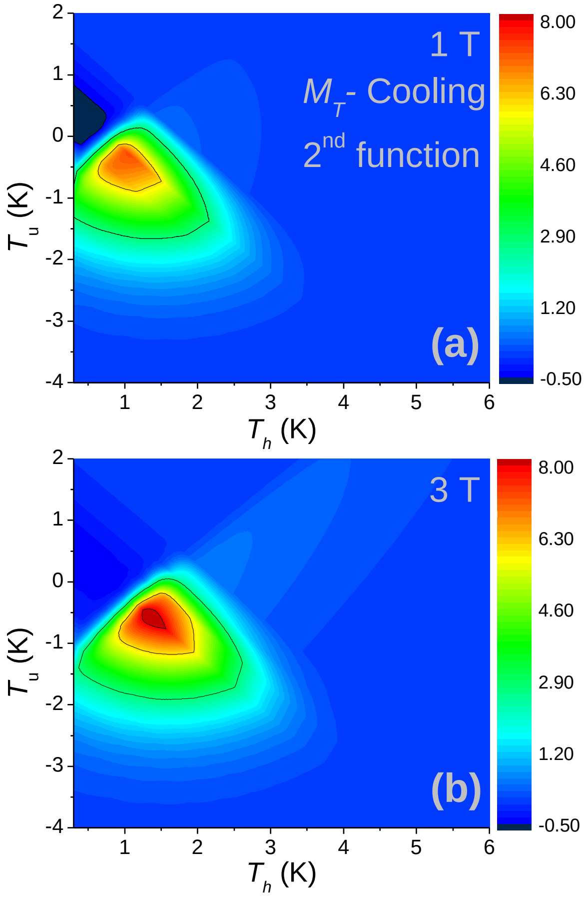

Figure 5.14. (a)-(b) Modeled TFORC distributions for 1 and 3 T, respectively, obtained using a secondary skewed distribution that slows down the transformation to austenitic phase.

5.3 Conclusions

The thermal hysteresis in materials undergoing magneto-structural transformation has been studied through the emergent TFORC method. For this, two Heusler alloys with compositions very similar to each other and close to the nominal stoichiometry $Ni_{50}Mn_{34}In_{16}$ have been used. As shown in **Chapter 4**, the rich variety of transformations makes these Heusler alloy systems particularly attractive as a model case study. In this case, the close stoichiometry of the two alloys produces a difference of around 10 K in their martensitic transformation while the thermomagnetic behavior of the martensitic and austenitic phases remains invariant from one alloy to the other. This enables a fine comparison and study of the influence of the phase overlap. For the interpretation of the TFORC distributions, these were calculated using a smoothing algorithm that skip the standard cross derivative calculation and provides a good compromise between smoothing and qualitative significance of the distributions. The complete magnetization loops have been recovered from the TFORC distributions, showing that those obtained by the unsmoothed distribution produces the most accurate reconstruction.

To unequivocally attribute the characteristics of the experimental TFORC distributions to the properties of the transformation, the behavior of the alloys has been modeled by combining a function for the structural transformation with another for the thermomagnetic behavior of the phases. The simulations allowed to separately study the effects due to the magnetostructural transformation and those emerging from the thermomagnetic behavior of the phases. It has been found that the peaks of the experimental distributions are highly altered due to the asymmetry of the transformation, with the occurrence of different transformation rates for heating and cooling processes. This produces a distortion of the TFORC distributions from the circular shape characteristic of symmetric transformations to a triangular appearance. Interestingly, the thermomagnetic behavior of the phases due the non-hysteretic Curie transitions has an influence in the distributions, adding extra asymmetry. Negative areas above the main peak appear in the cooling TFORC due to the relevant temperature dependence of magnetization due to the austenitic phase, with its Curie transition closely overlapped with the magnetostructural transformation. This effect is not present in the heating TFORC, in which the subtle temperature dependence of the magnetization of the martensitic phase gives rise to positive areas below the peak of the distribution.

6 Novel method for the fabrication of functional composite filaments for additive manufacturing

The printing of functional objects using the extended FDM technique is still under development with a limited variety of commercial functional filaments. Therefore, in most cases, it is necessary to resort to the elaboration of custom-made composite filaments. When developing own composite filaments of desired compositions (also spillovers to magnetic and magnetocaloric filaments), the filament quality cannot be disregarded because it will affect the process and quality of 3D printing. The standards of high-quality composite filaments entail good diameter homogeneity and homogeneous dispersion of the functional elements within the polymer matrix. With the ultimate goal to manufacture high-quality magnetocaloric filaments, a novel methodology is designed and verified. By using customized encapsulation of functional fillers as the feedstock for extrusion, homogenous composite filaments with controlled compositions are produced. In this chapter, as a proof-of-concept example, soft magnetic composites combining the thermoplastic PLA (polylactic acid) and maraging steel particles were produced. The magnetic properties and behavior of the fillers are preserved while the thermal and rheological behavior of the polymer change noticeably. The decrease of the melt viscosity of composites with respect to the pure polymer is the main attribution to the different processing parameters.

6.1 Methods for producing composite filaments

The fastest way of obtaining composite filaments usually rely on industrial grade machinery, such as kneaders or compounders. Even in these cases, it is still challenging to obtain smooth filaments with high filling fractions valid for 3D printing functional parts of high dimensional resolution [125]. On the other hand, at laboratory scale (so that the industrial reliance could be avoided), customized composite filaments have been developed by mixing the polymer and fillers without any blending mechanism before introducing the mixture directly to the hopper of an extruder [126]. However, this quick and simple method leads to a general problem of inhomogeneity in the distribution of fillers and unpredictable filler content, even for low concentrations as reported in Ref [126], in which 4 g of magnesium particles were mixed with 150 g of PLA. The solution casting is another way of lab-manufacturing custom-made composites which is based on the chemical mixing of the polymer and fillers using an appropriate solvent [127,128]. Once the solvent is removed, e.g., by heating, the resulting mixture is cut into pieces and used as the feedstock for extrusion. This method, although relatively simple, requires the use of an appropriate solvent, which is dependent on the polymer type and thus can post safety hazards and/or of limited resource availability. Additionally, the need of successive cutting and re-extrusion steps to achieve homogeneous filaments is also reported for this procedure. This noticeably increases the processing time, and might cause a low predictability and reproducibility of manufactured filaments [129].

Therefore, with the aim of elaborating functional magnetic composites with enhanced uniformity in a simple and repeatable way and avoiding industrial or chemical reliance, a novel encapsulation methodology for preparing the feedstock has been proposed and developed.

6.1.1 Description of developed procedure

To prevent the accumulation or loss of powder before it reaches the melting part of the extruder, polymer (PLA in our case) capsules that contain the magnetic fillers will be used as the feedstock for filament extrusion. This will require capsules of sizes and shapes similar to those of typical polymer pellets used for extruding filaments. The capsular design with precise dimensions was realized via CAD drawing using Autodesk Fusion 360 software (**Figure 6.1**). As shown, each template contains 16 capsules and a corresponding lid for the full template. All capsular templates in this work were 3D printed with a desktop Ultimaker S5 printer using a nozzle of 0.4 mm-diameter. Unlike the presentation of the template in **Figure 6.1 (a)**, the printing of the capsular designs was performed with the flat side facing down on the platform of the 3D printer. Capsule walls were formed by two layers of polymer (width of 0.35 mm) according to the default printing settings of the printer and nozzle size. In this way, the amount of polymer can be minimized while the presence of two-layered walls ensures no porosity for avoiding loss of fillers. The rounded part of the capsules (bottom side in **Figure 6.1 (a)**) was built using more than two layers of polymer as, according to the placement of the model on the build platform, it was the only hanging part and its walls were defined by the layer height (0.15 mm).

The hemispherical shapes of the capsules facilitate their filling by having a full diameter opening, while no inconvenience was found in the flowability of the feedstock inside the extruder. Nevertheless, the shape and dimensions of the capsules can be customized accordingly, i.e., thicker walls to lower the filler concentration, or, in contrast, increase filler concentration by further reducing the wall thickness in relation to the total volume of the capsule. Moreover, composition variation is also possible by mixing filled capsules and polymer pellets for the final feedstock since they are of similar shapes and sizes.

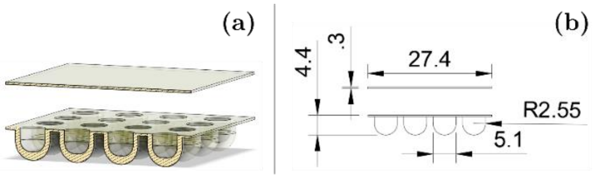

Figure 6.1. **(a)** 3D cross-sectional view of the capsular template and its lid (for sealing), and **(b)** their detailed dimensions in mm (where R refers to radius).

The next step of the feedstock preparation is fillers loading and encapsulation (see the schematic flowchart in **Figure 6.2**). For the former, it was done manually by leveling the powder (maraging steel in this case) up to the maximum height of the capsules to avoid any air bags during sealing. Subsequently, the encapsulation was completed by sealing the templates with lids (both made of the same polymeric material) using appropriate solvent of solubility, which is acetone in the case of PLA. The addition of a small amount of acetone to the base of a lid makes it sufficiently sticky to perfectly adhere to the capsular template. To finalize the process, the sealed templates were dried at 50 °C for 15 min to eliminate any trace of acetone. Alternative ways for the sealing can be explored depending on the polymer that is used, e.g., heat or pressure sealing. The latter will require some modifications to the design, resembling that of medical pills. However, none of these modifications (capsule production method or sealing procedure) will affect the principle of operation of the proposed methodology.

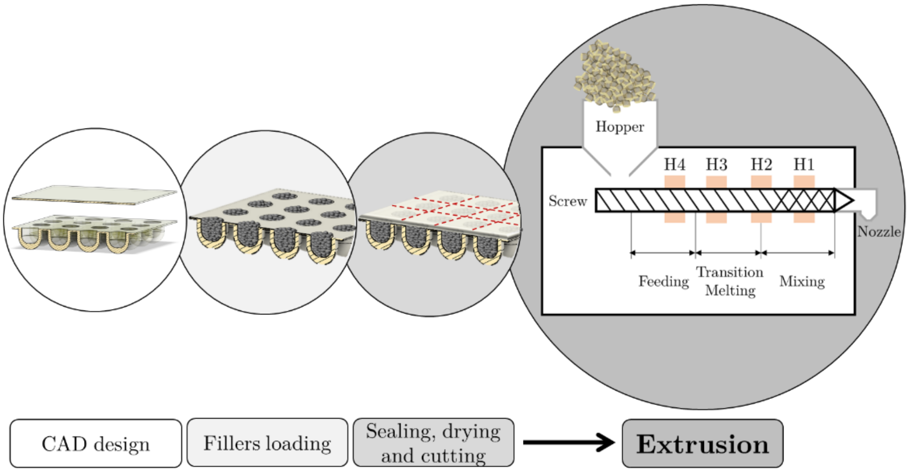

Figure 6.2. Schematic representation of the fabrication procedure. Starting from the CAD design, the templates are subsequently filled with the functional particles, posteriorly sealed before the individual capsules are finally separated to be used as typical pellets for the extrusion of the filament. The final element represents an extruder of thermoplastic materials, in which the different heaters are indicated (H1 to H4) along the extrusion path.

Once the templates were filled and sealed, individual capsules were separated and used as the feedstock for extrusion. The filaments in this work were all manufactured using a single-screw desktop extruder 3devo NEXT 1.0 ADVANCE. In this commercial extruder, there are four independent heaters along the melting and mixing zones, being the mixing zone at the end of the extrusion path and defined by a special design of the screw that facilitates the mixing of the polymer and fillers (see **Figure 6.2**). With the developed procedure, the polymer and fillers travel along the extrusion path in a constant proportion, avoiding the loss or agglomeration of the fillers, and reach the final mixing zone in the desired fraction so that a homogeneous filament can be obtained in a single extrusion process.

Alternative fabrication and filling procedures could speed up the procedure and take it even to industrial scale. Among them, vacuum- or thermo-forming could be good options for the manufacturing, including an automatic filling system. However, the use of 3D printing in this case constitutes an affordable, customizable, and fast way (without relying on industrial processes) of fabricating composite filaments for research in acceptable production volume for this purpose.

6.2 PLA composite filaments with soft magnetic maraging steel fillers

As a concept validation approach of the presented method, gas-atomized soft maraging steel particles and PLA were used to produce soft magnetic functional filaments with nominal filler fractions of 5, 8 and 12 vol. %. Both the fillers and polymer matrix are available in industrial quantities and are a good testing ground for validation.

The capsules filled with the maraging steel powder were mixed with proper amounts of PLA pellets (with similar shape and size) to fit the nominal filling fractions in the cases of 5 and 8 vol. %. In the case of the composite filament with 12 vol. % of fillers, only custom-made capsules were used as feedstock without any extra addition of PLA.

The temperatures used for the four heaters (H4 to H1) were 443 K – 458 K – 463 K – 453 K (170 °C – 185 °C – 190 °C – 180 °C). These temperatures are lower than those predefined for pure PLA due to the increased flowability of the composite filament when leaving the nozzle of the extruder. The filament diameter was set to 2.85 mm and was dynamically controlled in-situ by means of an optical sensor incorporated before the spooling mechanism. **Figure 6.3 (a)** shows the in-situ measurements of the filament diameter for 8 vol. % filament during extrusion. A linear fitting of the data gives a y-intercept of 2.845 mm that corresponds to the average filament diameter and a negligible slope indicating the constant trend during the process. Despite the scattering of the filament diameter around the average value, an RMS error (root mean square error) of 0.109 mm reflects a good agreement with the nominal diameter. Furthermore, these small fluctuations are typical of a PID-controlled process and would not limit the use of the filament in 3D printing.

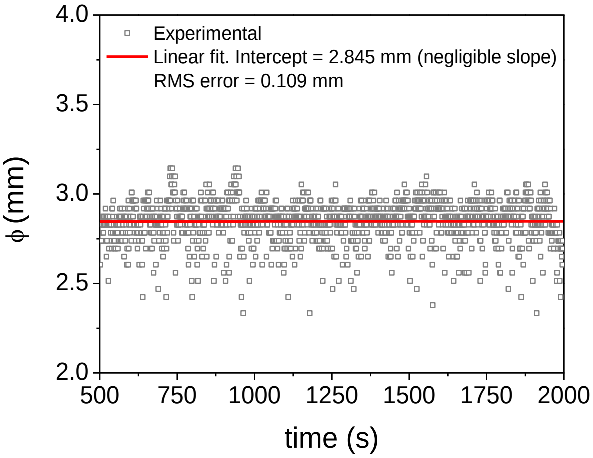

Figure 6.3. (a) In-situ measurements of the diameter of the composite filament with 8 vol. % of maraging steel particles during extrusion.

6.2.1 Morphological characteristics of the maraging steel composite filaments

Figure 6.4 shows the SEM images of the as-received maraging steel powder (the fillers) and manufactured composite filaments using a FEI Teneo microscope. The fillers shown in **Figure 6.4 (a)** are of spherical shape, being noticeable a wide range of particle sizes. Panels **(b)-(d)** of **Figure 6.4** show the SEM images of unpolished cross-sections (perpendicular to the axis of the cylindrical filaments) of the composites with nominal 5, 8, and 12 vol. %, respectively. These images show that the fillers preserve their original morphology and how they are embedded within the polymeric matrix. The observed gaps in **Figure 6.4 (b)-(c)** are due to the detachment of some particles when segmenting the filaments for characterization. The insets of **Figure 6.4 (b)-(d)** present the complete and polished cross-sectional areas of the corresponding filaments using the BSE imaging. In this case, the morphological characteristics of the particles are affected by the polishing, but the different atomic number contrast between the polymer and metallic particles gives an overview of the particle dispersion. These images show that the particles are evenly dispersed throughout the section of the filaments with no observed particle aggregations or empty zones.

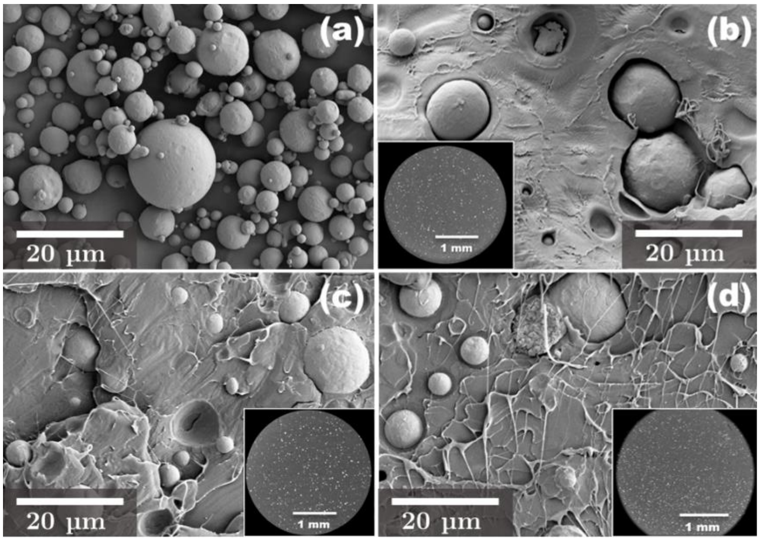

Figure 6.4. (a) SEM micrograph of the gas-atomized maraging steel powder. **(b)-(d)** SEM images of unpolished cross-sectional areas of the composite filaments with 5, 8 and 12 nominal vol. % of fillers, respectively. The insets in **(b)-(d)** show BSE images from of the complete and polished cross-sectional areas of the corresponding composite filaments.

The achievement of evenly dispersed particles can be an important challenge, especially for composite filaments with low and controlled fractions of fillers. This type of composite filaments is interesting for the manufacturing of "smart parts" which, thanks to the functional property added with the fillers, can give information about their local operating conditions. Although the SEM images suggest an even distribution of particles, this only provides surface information and, therefore, it might not be representative of the volume of the filaments.

The volumetric distribution of fillers was investigated by means of micro-computed X-ray tomography for the composite filament with the lowest fraction of maraging steel particles (nominal 5 vol. %). It was performed using the Easytom XL 160 system equipped with an open X-ray tube (LaB6) producing a spot of less than 500 nm width at the tungsten anode to achieve a resolution of < 1 µm. The total analyzed volume corresponds to a cylindrical section of ϕ1.8 mm x 1.1 mm of the interior of the filament.

Microstructural quantification was performed using the MorpholibJ suite of plugins [130] in the open source image analysis software FIJI [131]. In this analysis, each particle can be labeled and individually accounted for the calculations. Hence, a cubic volume of 1 mm length was cropped from the images for a detailed analysis (this reduced volume is due to the large number of particles with the consequent computational cost). A square cross section of the center of the analyzed cubic volume is presented in **Figure 6.5 (a)** (with the rotation axis of the filament perpendicular to the page) after applying the thresholding algorithm "distance transform watershed 3D" that enables the distinction of individual particles which are in contact with each other. Then, for each particle, the volume, surface, and coordinates of the center of mass are stored. **Figure 6.5 (b)** shows the same cropped section in which each particle is joined to its first neighbors according to the Delaunay triangulation method, from which the distribution of inter-particle distance can be obtained. From the total reconstructed volume, the sum of the particle volume is computed, giving a fraction of 5.5 ± 0.5 vol. %, which is in very good agreement with the intended concentration. The 3D-reconstruction of a cubic volume with 300 µm edge at the center of the total analyzed volume is shown in **Figure 6.5 (c)**, where particles are colored based on their sizes.

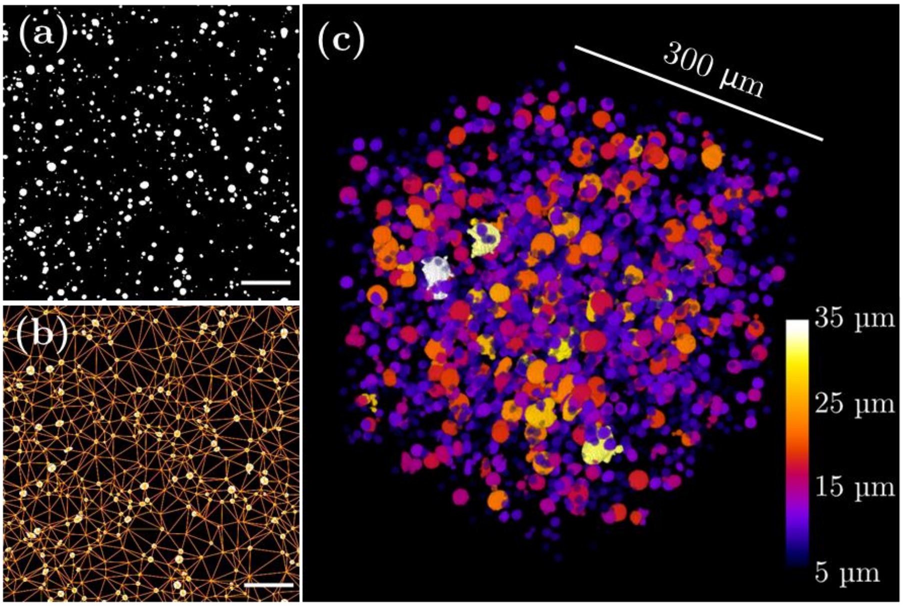

Figure 6.5. X-ray tomography results of the composite filament with nominal 5 vol. % of maraging steel particles: **(a)** cropped slice of the total analyzed volume after the application of a segmentation algorithm to separate adjacent particles, **(b)** Delaunay triangulation for determining the inter-particle distance. **(c)** 3D reconstruction of a cubic subvolume of 300 µm edges with particles colored according to their diameter. Scale bars in panels **(a)-(b)** represent 100 µm.

Figure 6.6 (a) shows a histogram with the particle sphericity obtained by comparing the volume (V_p) and surface area (S_p) of the particles with those of a perfect sphere with the same volume, i.e.:

$$sphericity = \frac{\pi^{\frac{1}{3}}(6V_p)^{\frac{2}{3}}}{S_p}. \tag{6.1}$$

A sphericity of 1 is attributed to a perfect spherical shape. More than 75 % of the particles have a sphericity in the 0.9 – 1.0 range, confirming the highly spherical shape of the gas atomized maraging steel particles. Using the volume of each particle, once confirmed that most of them are nearly spherical, the equivalent diameter (d) can be obtained by inverting the formula of the sphere volume, i.e., $d = (6V/\pi)^{\frac{1}{3}}$. The distribution of particle diameters is shown in **Figure 6.6 (b)** wherein the histogram and black line represent the relative and cumulative frequencies, respectively. The relative size distribution is fitted to a log-normal distribution (red line) whose formula is given by:

$$P(d) \propto \frac{1}{\sqrt{2\pi\sigma^2}} \frac{1}{d} \exp\left[-\frac{(\ln d - \ln \mu)^2}{2\sigma^2}\right]. \tag{6.2}$$

The log-normal distribution is typically valid for the description of phenomena involving a random variable with a large amount of data in which negative values are physically impossible, as in the present case. From the fitted parameters μ and σ, the mean particle diameter ($\bar{d}$) and the variance (σ_d) are obtained according to:

$$\bar{d} = \mu \exp\left(\frac{\sigma^2}{2}\right), \qquad \sigma_d = \bar{d}\sqrt{\exp(\sigma^2) - 1}\,. \tag{6.3}$$

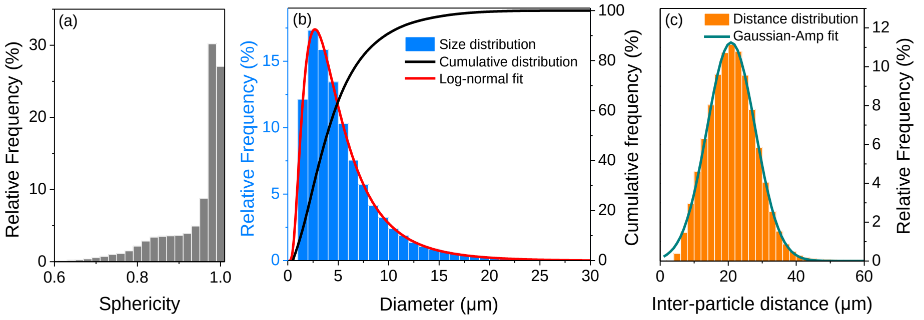

Figure 6.6. (a) Particle sphericity distribution. **(b)** Distribution of the equivalent particle diameter in relative frequency (histogram), its fitted log-normal distribution (red line) and cumulative frequency (black line). **(c)** Distribution of inter-particle distance (histogram) and the fitted curve corresponding to the amplitude version of the gaussian distribution (dark cyan line).

The analyzed volume of the filament gives a mean particle diameter of $\bar{d} = (6 \pm 4)\ \mu\mathrm{m}$. The results of the relative frequency of inter-particle distance from the Delaunay triangulation is presented in **Figure 6.6 (c)**. This distribution is fitted to the amplitude version of a gaussian peak function from which a mean separation of (22 ± 10) µm is obtained. The fitting to a gaussian distribution is an indication of the even distribution of particle distance. Additionally, an average distance between first neighbors much larger than the mean particle diameter further confirms the appropriate dispersion of the particles within the filament and the lack of agglomeration within the analyzed volume. This demonstrates the validity of the manufacturing method, as a homogeneous distribution of particles is achieved even in the case of the lowest particle fraction.

6.2.2 Functional magnetic properties

Figure 6.7 shows the $M(H)$ loop of the maraging steel powder at room temperature. The soft magnetic behavior is evident, with a coercivity that is imperceptible in the plotted magnetic field range. The saturation magnetization (M_S) is 110.58 A m^2 kg^{-1} for 1.5 T. The inset of **Figure 6.7** corresponds to the magnified intercept with the x-axis, from which a coercive field of $\mu_0 H_c = 2.81\ \mathrm{mT}$ is obtained.

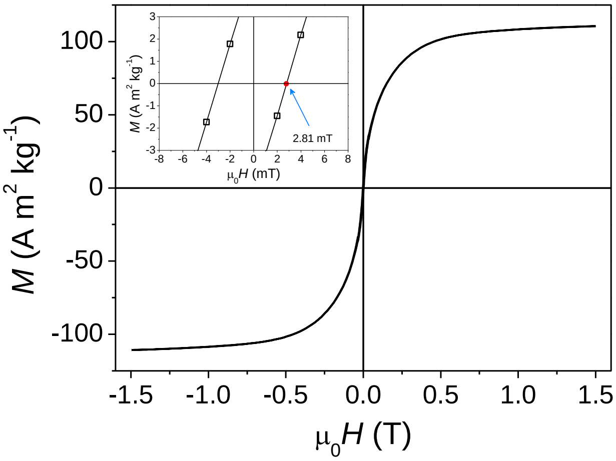

Figure 6.7. $M(H)$ hysteresis loop of the mararing steel powder used as filler for the composites. The inset magnifies the low field region to determine coercivity (2.81 mT).

The first quadrant of $M(H)$ loops of the maraging steel powder and selected pieces of the three composite filaments are shown in **Figure 6.8**. Assuming a linear relationship between the magnetization of the composite filaments and particle content, the mass fraction of fillers can be estimated by comparing their saturation magnetization per unit mass for the maximum field of 1.5 T with that of the raw maraging steel powder. This leads to fractions of fillers of 26.5, 37.5 and 47.5 wt. % for the filaments with nominal 5 vol. %, 8 vol. %, and 12 vol. %, respectively. The volume percent of fillers can be calculated using the obtained weight fractions and the densities of the phases (1.25 g cm^{-3} and 8.10 g cm^{-3} for PLA and maraging steel, respectively).

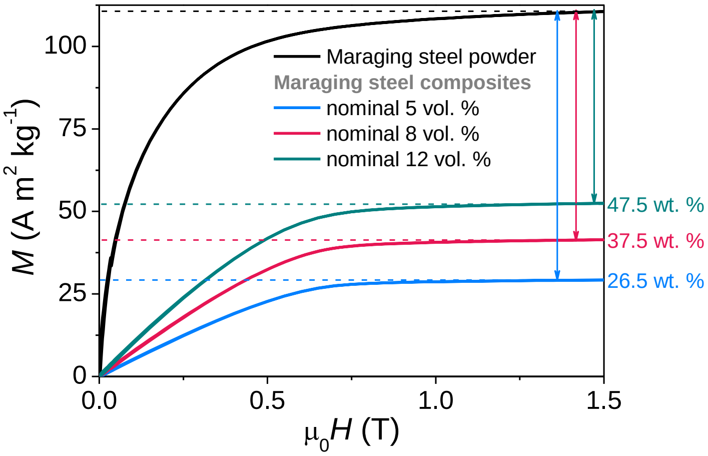

Figure 6.8. First quadrant of the $M(H)$ hysteresis loop of the raw maraging steel particles (compacted in a silver capsule) and the different composite filaments. The mass fraction of fillers in the composites is obtained by comparing their saturation magnetization per unit mass with that of the raw magnetic powder.

The results are summarized in **Table 6.1**, which shows the good correspondence between nominal and experimental values obtained from magnetic measurements.

Table 6.1. Fraction of maraging steel fillers within the composite filaments determined through magnetization measurements.

Sample	M_S (A m^2 kg^{-1})	Amount of maraging steel powder determined from M_S	
		wt. %	vol. %
Raw powder	110.6	100.0	100.0
5 vol. % nominal	29.2	26.4	5.3
8 vol. % nominal	41.4	37.5	8.5
12 vol. % nominal	52.5	47.5	12.2

It is also observed that the composite samples exhibit soft magnetic behavior with the same coercivity of the raw maraging steel powder. The appreciable difference in the shape of the curves of the composites with respect to that of the raw maraging steel powder, with a lower slope up to saturation, is due to different demagnetizing factors.

MOKE observations were carried out on a piece of the filament with nominal 5 vol. % of maraging steel fillers. This was done in order to find evidence of interaction between the particles, related with the dispersion of the fillers within the polymer matrix. For the measurements, the filament piece was polished using a colloidal Si-suspension (OP-S from Struers) to minimize the residual stresses due to grinding and polishing. **Figure 6.9** shows the MOKE images with the magnetic domains present in different maraging steel particles of the composite filament. For the visualization of the domains, pure in-plane Kerr sensitivity [132] was used along the horizontal direction in which the magnetic field was applied. Domains shown in **Figure 6.9 (a)** correspond to the demagnetized state of three particles that are relatively close to each other, achieved by means of an AC field decay to zero from an initial saturating field. Domains present in **Figure 6.9 (b)-(c)** correspond to the remanence state at zero field of isolated particles. For the presented images, the saturation state (with no domain contrast) was subtracted from the final images to improve the domains visualization. As the specimen was polished along the longitudinal axis of the filament, the domains adapt to the exposed surface due to energy reasons and may not be the same as those of bulk spherical particles. The observed domain patterns seem to correspond to the superficial or closure pattern of underlying volume domains with some component of magnetization that can point out-of-plane. The size of the observed domains ranges from sub-micrometer up to several micrometers and, despite their adaptation to the surface, domains of similar sizes would be expected for the volume owing to the reduced sizes of the particles.

No domain contrast is detected for polar conditions under pure Kerr sensitivity to out-of-plane magnetization, indicating that the shown domains are strictly magnetized in-plane. These characteristics are typical of low-anisotropy soft magnetic materials, in agreement with previous results indicating the global soft magnetic character of the maraging steel powder and composites. No evidence of magnetic stray-field interactions among the particles is noticed, which can further confirm the good dispersion of the particles within the PLA matrix. However, it cannot be known with much certainty whether the wide range of domain sizes, i.e., an inhomogeneous distribution of anisotropy, is caused by the crystallographic grain structure of the particles or due to internal stresses. Nevertheless, this does not play a relevant role in the macroscopic magnetization of the composite filaments, which seems to be more influenced by demagnetizing effects than by anisotropy.

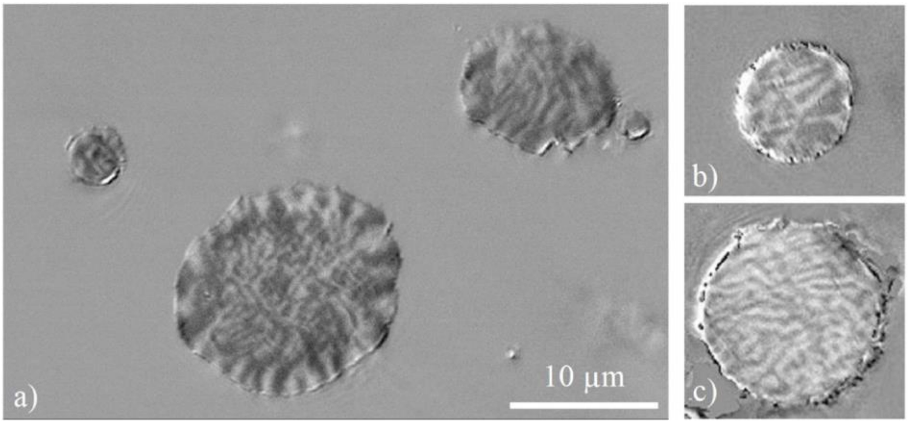

Figure 6.9. Magnetic domains present on the polished surface of maraging steel particles embedded into PLA matrix corresponding to the composite with nominal 5 vol. %: (a) group of three neighboring particles and, (b)-(c) isolated particles without any neighbor in the proximity [133].

6.2.3 Thermal analysis

Figure 6.10 shows the results of the TGA of pure PLA and composite filaments measured using a TA Instrument Q600 calorimeter under N_2 atmosphere. For the measurements, samples of ~10 mg were placed into open platinum pans. This analysis allows to evaluate the processes of mass change (loss) that take place upon the total degradation of the PLA polymer. The pure PLA sample completely degrades above 750 K (477 °C), with a mass loss of ~100 wt. % in a single step. The small remnant of ~0.5

% wt. % could be ascribed to a minor fraction of non-volatile components or ash. Samples from the composites also show the degradation process of PLA down to a final wt. % that is associated to the fraction of metallic fillers. The remaining mass in the TGA curves of the composites with nominal 5, 8, 12 vol. % results in 30, 39, and 52 wt. %, respectively. These results confirm the validity of the magnetic measurements for a good estimation of the composite filament compositions, whose values, on average, are underestimated by ~2 %. Therefore, using the magnetic measurements for estimating the compositions of magnetic filaments is a useful alternative to the analysis from TGA experiments, as it also offers other advantages such as being faster and non-destructive.

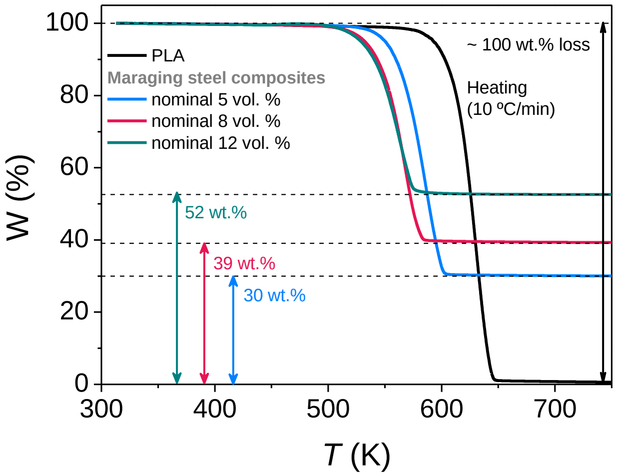

Figure 6.10. TGA curves upon heating of pure PLA and samples from the different PLA + maraging steel composites. The weight percent of fillers is indicated as the remaining weight in composites once the PLA has completely degraded.

TGA experiments can also show the kinetics of the degradation process of the polymer and reveal the effects of the filler additions to the degradation. So far, it is evident from **Figure 6.10** that the addition of fillers shifts the onset of the mass loss to lower temperatures. However, this shift does not seem to be monotonic with increasing fraction of fillers but saturates for a specific fraction, given that the onset of the mass loss for the samples with 39 and 52 wt. % of fillers coincide. To further analyze the degradation process of the PLA, the derivative with respect to temperature of the weight percent is shown in **Figure 6.11 (a)**. The peaks corresponding to the curves confirm that the degradation process occurs in a single step for the different samples. The temperature of the maximum mass loss, T_{pk}^{TGA}, shifts to lower values when increasing the filler content in the composites. For the sample labelled with 30 wt. %, the peak is shifted more than – 40 K with respect to that of pure PLA. For 39 and 52 wt. % samples, their T_{pk}^{TGA} values are separated by ~ 6 K, confirming the non-linear trend of T_{pk}^{TGA} with the fraction of fillers. Apart from the shift of the T_{pk}^{TGA} and the magnitude of the peaks, the shapes of all the different derivative curves look similar. A better comparison can be performed by normalizing the different derivative curves and using a modified temperature axis $(T - T_{pk}^{TGA})$ so that all the curves are centered at the peak. These normalized curves are shown in **Figure 6.11 (b)**, being now evident that all the peaks overlap. Therefore, the addition of the maraging steel particles just lowers the temperature at which the degradation of PLA takes place up to a certain concentration, but the kinetics of the process remains invariant once it starts. For all the studied composites, the new onset temperatures of the degradation of PLA are still far from the processing temperature for the 3D printing.

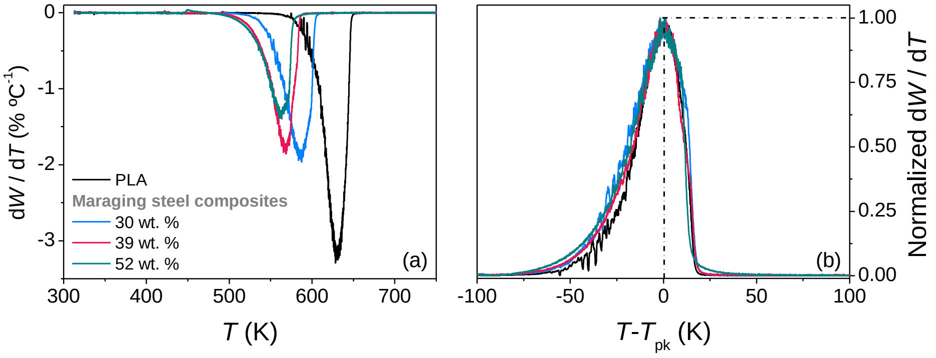

Figure 6.11. (a) Temperature derivative of TGA curves of pure PLA and PLA + maraging steel composites. **(b)** Normalized derivative curves vs. the shifted temperature axis $T - T_{pk}^{TGA}$.

Figure 6.12 shows the DSC results of pure PLA and composite samples upon heating. The heat flow axis is shown in arbitrary units as the different curves have been vertically shifted, avoiding their overlap, to enhance visualization. Samples were measured using a DSC Q20 calorimeter (TA Instruments) where samples were sealed in hermetic aluminum pans.

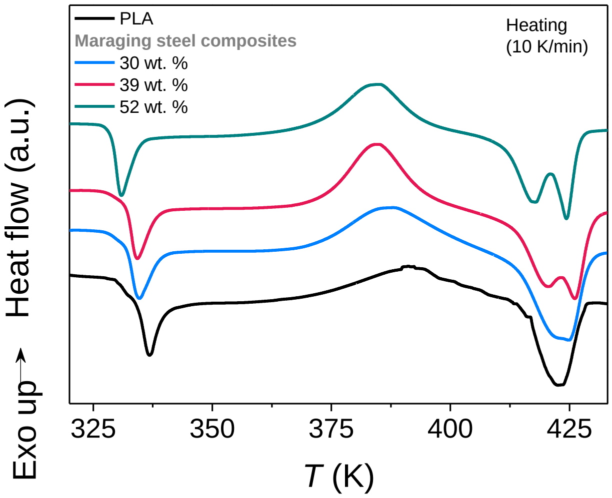

Figure 6.12. Differential scanning calorimetry curves of PLA and maraging steel composite samples upon heating.

For pure PLA, the first observed feature in its DSC results is at ~330 K due to the glass transition. This corresponds to the transformation of the amorphous polymer from a rigid to a flexible and rubbery state with the increasing molecular mobility caused by increasing temperature. This type of transition is commonly identified as a step in the DSC heat flow due to a change of the heat capacity. However, the step in this case is followed by an endothermic peak that is related to the presence of thermodynamically unstable amorphous polymer that passes to a more energetically favorable state [134–136]. The behavior at the glass transition of the PLA indicates that the polymer has been rapidly cooled down below its glass transition temperature. The following exothermic peak is due to the so-called cold crystallization process that takes place when the amorphous polymer is able to crystallize due to the increased molecular mobility below its melting point. The final endothermic peak indicates the melting of the polymer. The degree of crystallinity of the polymer, χ_c, can be estimated by comparing the difference between the enthalpies related to the melting and cold crystallization, ΔH_m and ΔH_{cc} respectively (calculated by integrating the corresponding heat flow peaks with respect to time), with the enthalpy of melting of pure crystalline polymer, ΔH_m^0:

$$\chi_c = \frac{\Delta H_m - \Delta H_{cc}}{w_p \cdot \Delta H_m^0}, \tag{6.4}$$

where w_p is the weight fraction of polymer in the sample (ranging from 1 to 0.48 in this work) [76,137,138]. For the present case of pure PLA, the difference between the cold crystallization and melting enthalpies is nearly zero (within the error margin of the measurements), implying a negligible χ_c. This should be due to the extrusion process in which the fused polymer that exits the nozzle of the extruder is rapidly cooled and solidified by the means of fan, avoiding the formation of crystals.

For the composite filaments, their DSC curves show the same qualitative features as that of pure PLA although there is some difference in their transition temperatures (obtained as the temperature at the corresponding peaks) as summarized under **Table 6.2**.

The glass transition temperature, T_g, decreases as the filler fraction increases, having a difference of 6 K between pure PLA and the composite with the highest filling fraction. The cold crystallization is also affected by the addition of fillers, with a peak that becomes sharper, at a temperature, T_{cc}, that shifts to lower temperatures as the filler fraction increases. This is in agreement with previous reports in which the addition of different types of fillers favor the crystallization of the polymer by acting as nucleation centers [76,136,139,140]. The final melting transition of the polymer shows the most evident change when increasing the filling fraction. Its peak splits into two overlapping but distinguishable components as the filler fraction increases. This can be ascribed to the formation of α' phase during the cold crystallization process, constituted by small and disordered crystalline lamellae with lower melting point than the ordered α form of PLA [136,139,140]. A possible explanation for this can be that the dispersed metallic fillers, acting as nucleation centers, favor the earlier formation of the disordered crystalline lamellae around them, while larger and ordered α phase is formed in the bulk of the polymeric matrix.

Table 6.2. Temperatures at the peaks of the different transitions that take place in pure PLA and composite samples, labeled with their wt. % obtained from the TGA measurements.

Sample	Glass transition T_g (K)	Cold crystallization T_{cc} (K)	Melting T_m (K)
PLA	336.8	391.2	422.6
30 wt. %	334.8	388.0	422.3 - 424.5
39 wt. %	334.3	384.9	400.6 - 153.0
52 wt. %	330.8	384.9	417.4 - 424.4

6.2.4 Viscoelastic characterization by shear rheology

Viscoelastic properties of the different samples were investigated by means of small amplitude oscillatory shear (SAOS) measurements using a controlled stress rheometer TA Instruments DHR-3 with 40 mm parallel-plates geometry (1 mm gap). These experiments were performed at 433 K (160 °C), which is above the melting points of all the samples. The viscoelastic properties of the polymer-based filaments in the fluid state are directly related to their extrudability and printability.

First, the elastic (G') and viscous (G'') moduli have been obtained by means of small amplitude shear rheology (SAOS) at 433 K, as shown in **Figure 6.13 (a)**. This type of measurement implies that the specimens are deformed by means of small oscillatory (sinusoidal) stress so that the oscillatory response of the material is within the linear viscoelastic region (LVR). In the LVR, the stress and strain are proportional and it ensures that the structure of the material is not affected by the measurement. Both G' and G'' exhibit a strong frequency dependence, and G'' is predominant within the whole frequency range as expected for melted thermoplastic polymers. The decrease in both viscoelastic moduli with increasing filling fraction is significant. These results indicate that the addition of these metallic fillers increases the fluid character of the melted polymer, which seems to be associated to the decrease of the melt viscosity. This could lead to the need of lowering the extrusion and printing temperatures of the composites to values below than that of PLA due to their higher flowability.

To confirm this assumption, the flow properties have been analyzed at 433 K by means of steady-state flow measurements, which provide the steady shear viscosity (or apparent viscosity) of the fused samples. The setup for such measurement is the same as for the previous technique, but the moving plate rotates without changing direction, providing a shear rate, $\dot{\gamma}$, which is continuously swept by varying the velocity of the plate:

$$\dot{\gamma} = v/h, \tag{6.5}$$

where v is the velocity of the moving plate and h the gap between the parallel plates (i.e., the thickness of the sample).

The complex viscosity obtained from the SAOS measurements ($\eta^* = G''/G'$) can be compared with the apparent viscosity (η) from the steady-state flow tests using the Cox-Merz rule:

$$\eta^*(\omega) = \eta(\dot{\gamma} = \omega), \tag{6.6}$$

Neither the pure PLA nor the composites follow this rule. However, the results for all the studied samples fit to a modified Cox-Merz rule, in which a constant dimensionless parameter A is multiplied by the complex viscosity to account for the effect of shear forces on the unperturbed microstructure of the systems [141]:

$$A \cdot \eta^*(\omega) = \eta(\dot{\gamma} = \omega). \tag{6.7}$$

Figure 6.13 (b) shows the apparent and effective complex viscosity ($A \cdot \eta^*$) as a function of the shear rate and ω, respectively. All the samples follow the modified Cox-Merz rule for a single value of $A = 0.59$, independently of the filler fraction and the type of shear stress applied (steady or oscillatory). This confirms the decrease of the viscosity with increasing filling fraction.

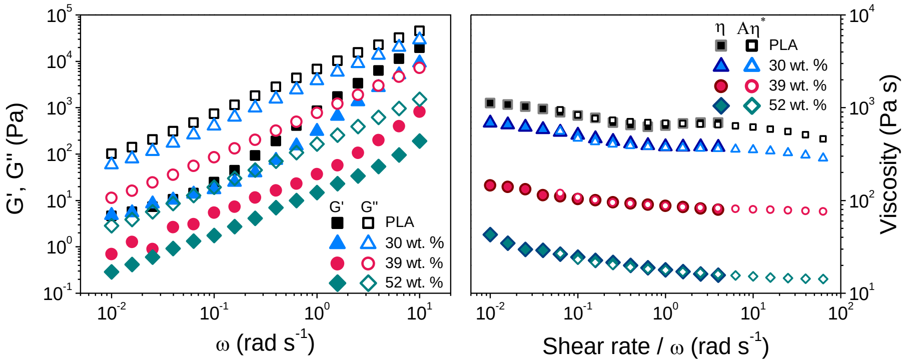

Figure 6.13. (a) Elastic (G', solid symbols) and viscous (G'', open symbols) moduli as a function of the angular frequency through SAOS measurements at 433 K. **(b)** Apparent (η) and complex ($A \cdot \eta^*$) viscosities of PLA and PLA + maraging steel composites at the same temperature.

It is usual that the viscosity of filler-containing polymers increases with increasing filling fraction [125,142–145]. However, it is found that, in some special cases, the addition of fillers can produce the opposite result [146,147]. In such cases, the reduction of the viscosity for the filled polymers is explained by the decrease in the interlayer interactions of the fused polymer or by the internal reduction of the friction between the polymer layers caused by the spherical particles, i.e., the so-called "ball-bearing" effect.

The results showing the decrease of the melt viscosity with increasing filling fraction clarify the need to lower the temperatures during the extrusion of the filaments and printing: to reduce the flowability of the composites during the process. This is also favorable to prevent nozzle clogging (that can occur when printing with composite filaments) due to the high flowability, which can be reduced to a level similar to that of PLA by lowering the temperature. The results from the viscoelastic characterization obtained in this work and previous studies in **Refs.** [146,147] suggest that further increase of the fraction of fillers will continue to reduce the viscosity to a certain point, at which it should begin to increase. This is connected to the appearance of agglomeration and aggregates of particles, which would hamper the flowability of the fused polymer.

6.3 Conclusions

A novel procedure for the manufacturing of composite filaments for the FDM additive manufacturing technique has been proposed in this chapter. The method consists of the preparation of custom-made polymer capsules filled with the functional particles. These capsules filled with soft magnetic maraging steel particles have been successfully used as the feedstock for extruding magnetic composite filaments with controllable concentration and large uniformity, retaining its magnetic behavior. The use of this type of magnetic maraging steel powder, available on an industrial scale, has served as a validation of the proposed methodology. Filaments with fractions of fillers ranging from 30 to 52 wt. % have been prepared and extensively characterized, where: (1) low fractions of metallic fillers yield filaments that preserve the characteristics of the polymer matrix with an extra magnetic behavior, useful in some scenarios, e.g., as sensors; (2) high filling fractions cause a notable change of the thermal and rheological behavior of the polymer that requires optimization to the processing and 3D printing parameters. The reliability and homogeneity as evidenced by the different characterization techniques confirms the validity of the proof-of-concept method for applying to the manufacturing of magnetocaloric composite filaments.

7 Magnetocaloric composites filaments for additive manufacturing

Additive manufacturing can provide attractive solutions for manufacturing magnetocaloric regenerators with complex and precise geometric designs, which serve the performance optimization of the devices. This is due to the shape versatility offered by AM, thus minimizing or avoiding the step of net shaping into final structures, unlike conventional manufacturing processes. In addition, this is highly appreciated when applied to magnetocaloric materials undergoing FOPT as their intrinsic brittleness (due to their intermetallic character) pose challenges in manufacturing them into the required geometrical regenerator shapes and dimensions. FDM, among the AM techniques, appears to be an excellent candidate for 3D-printing magnetocaloric parts: the combination of the processability of thermoplastic materials (whose processability shape and give consistency to the structure) with functional magnetocaloric particles. Given the promising results of the manufacturing method described in **Chapter 6**, it is applied in this chapter to produce functional magnetocaloric filaments. In this case, two examples of the promising magnetocaloric materials have been used: (1) Ni_2MnGa Heusler alloy, and (2) $La(Fe,Si)_{13}$-H. The magnetic, thermomagnetic and magnetocaloric functional behavior of the composite samples, arising from the fillers, are found to be retained while the thermal properties of the polymer are significantly affected by the metallic fillers.

7.1 PLA composite filaments with magnetocaloric Ni_2MnGa Heusler alloy fillers

PLA has been used again as the polymeric material for the composite filaments, incorporating in this case particles of Ni_2MnGa Heusler alloy. As the previously studied off-stoichiometry Ni_2MnIn Heusler alloys, the family of full Heusler alloys with stoichiometry around Ni_2MnGa can also exhibit a martensitic transformation from a parent austenitic phase (cubic $L2_1$-type) to a tetragonal martensitic structure upon cooling.

7.1.1 Filament fabrication

Composite filaments combining PLA polymer and ultrasonic-atomized Ni_2MnGa Heusler alloy were manufactured using the encapsulation method described in **Section 6.1.1**.

The powder was prepared by ultrasonic atomization by the company AMAZEMET (Poland) and the Faculty of Materials Science and Engineering of the Warsaw University of Technology (Poland). This technique consists of pouring the melted alloy onto a flat surface that is vibrating at a frequency of more than 20 kHz. The thin sheet of molten metal that is formed over the vibrating surface partitions into fine droplets due to vibration. The droplets solidify into spherical particles whose mean diameter can be controlled by varying the frequency of the vibration: higher frequencies produce lower particle size. Ultrasonic-atomization technique, like gas atomization, gives rise to highly spherical particles.

Particles were sieved to 100 µm, which is lower than the mean diameter size of the as-atomized powder. The morphological characteristics and composition of the particles of Ni-Mn-Ga Heusler alloy have been studied through SEM microscopy and EDX (FEI Teneo microscope), with results shown in **Figure 7.1 (a)**. The spherical aspect of the particles is evident, as well as the relatively uniform particle sizes. The EDX analysis was performed by scanning a large area, i.e., averaging numerous particles. The measured composition, $Ni_{49}Mn_{30.5}Ga_{20.5}$, has associated an e/a of 7.65, for which the martensitic transformation should appear close to room temperature [5,112,148], as intended. Therefore, the ultrasonic atomization is shown to be an effective technique, alternative to the more usual gas-atomization, to produce highly spherical powder which is desirable for many of the AM techniques using metals. To increase the filling fractions of the filaments with respect to the maximum one achieved in the case of maraging steel composites, the design of the capsules has been slightly modified by removing some internal layers of the original 3D model shown in **Figure 6.1.** This was possible without compromising the hermeticity of the capsules and no powder leaks were found. **Figure 7.1 (b)** shows an unpolished cross-sectional cut of the composite filament with the highest fraction of Ni_2MnGa fillers (64 wt. % according to TGA measurements). It is evident in this case that the particles are embedded in the polymer, being clear the high filling fraction achieved.

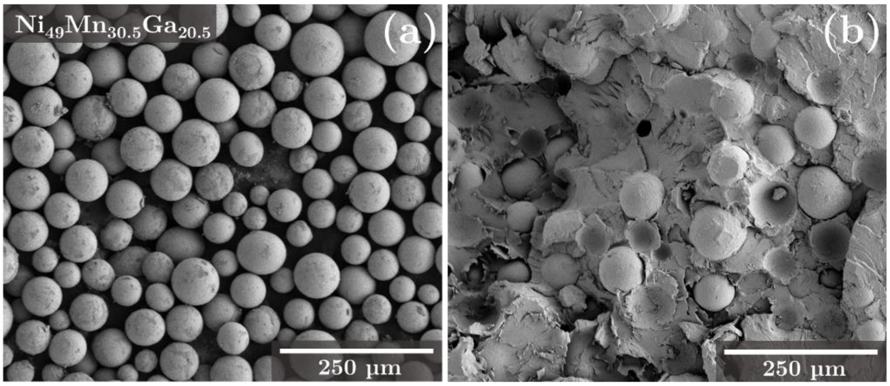

Figure 7.1. (a) SEM micrograph of the off-stoichiometry Ni_2MnGa powder with the measured chemical composition obtained by EDS. **(b)** SEM image of a sectional area of the composite filament of highest filling fraction of Ni_2MnGa powder (64 wt. %).

For this series of filaments, it was also necessary to lower the temperatures of the different heating zones of the extruder for a proper extrusion. The optimal temperatures used for the 4 different heaters (starting from the one closest to the hopper) for the highest filled filament were 438 K – 453 K – 455 K – 445 K. These temperatures are lower than those for standard PLA and slightly lower than those set for the extrusion of the PLA + maraging steel composites. The need of lowering the temperature for the proper extrusion of these composites, associated to their high flowability, indicates that the previously studied viscosity reduction with the addition of maraging steel particles (up to 52 wt. %) is also present in this case with larger particle size in which a higher filling fraction is reached.

7.1.2 Thermal analysis

Figure 7.2 shows the TGA curves of PLA and composites with embedded off-stoichiometric Ni_2MnGa particles. As previously indicated, the remaining mass after the PLA degradation in composites is used as the wt. % of the non-volatile metallic fillers. In this case, filler concentrations of 30, 39, and 64 wt. % are obtained. The thermal degradation of PLA is shifted to lower temperatures with increasing filling fraction.

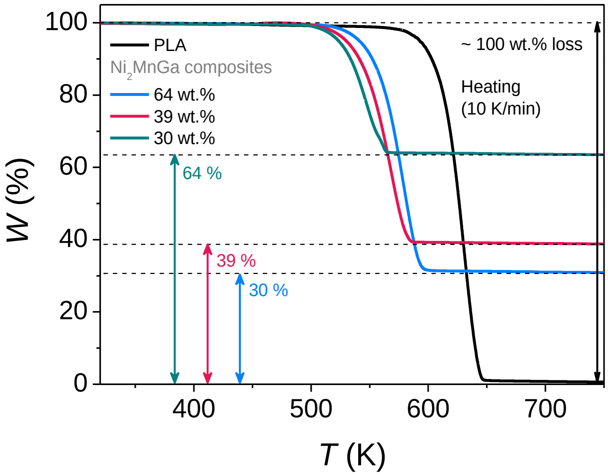

Figure 7.2. TGA curves upon heating of pure PLA and samples from the composites containing Ni-Mn-Ga fillers.

The derivative of TGA curves with respect to temperature (**Figure 7.3 (a)**) shows that the thermal degradation of PLA occurs in a single step, except for the composite with 64 wt. %, for which a minor distortion is present at the end of the peak. This additional minor peak is associated to a slowdown of the mass loss that could be ascribed to final remnants of the polymer trapped by the particles. Except for this peak distortion of the 64 wt. % sample, the normalized and temperature-shifted curves in **Figure 7.3 (b)** overlap, which indicates that the kinetics of the thermal degradation of PLA remains almost invariant by the addition of Ni_2MnGa particles in this range of mass fraction. Taking into account the densities of both components (8.20 and 1.25 g cm^{-3} for Ni_2MnGa and PLA, respectively), the filament with 64 wt. % of fillers has an associated volume fraction of fillers of 21.3 %.

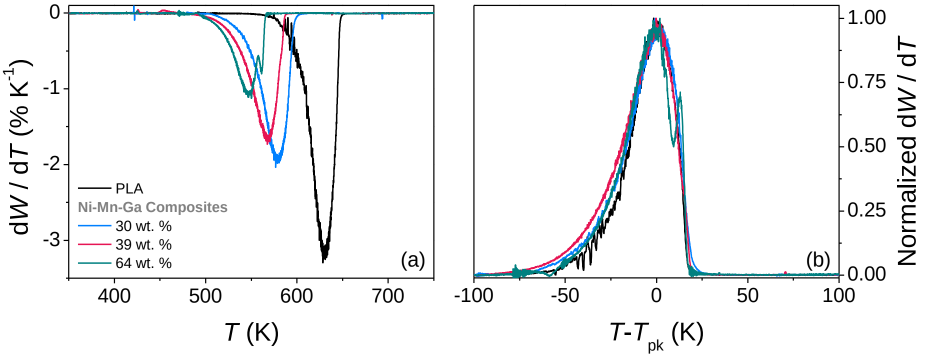

Figure 7.3. (a) Temperature derivative of TGA curves of pure PLA and Ni-Mn-Ga composites. **(b)** Normalized derivative curves vs. a rescaled temperature axis $T - T_{pk}^{TGA}$.

The DSC curves of PLA and PLA-based Ni-Mn-Ga composites are presented in **Figure 7.4**. As the filling fraction increases, the thermal behavior of PLA changes similarly to the previous case of the PLA + maraging steel composites. The observed features in are:

1. A glass transition that shifts to lower temperatures with increasing concentration of fillers, with a subsequent endothermic peak that indicates the presence of a predominant rapidly cooled amorphous phase.

2. A more prominent cold crystallization peak ascribed to the effect of the fillers acting as nucleation centers.

3. A melting transition that splits into two peaks due to the formation of the α' phase during the cold crystallization in composites.

It is worth mentioning that the DSC curve of the composite with 64 wt. % of fillers shows smoother peaks in each of the transitions in comparison with the other samples. This can be due to a smaller mass of polymer in this case.

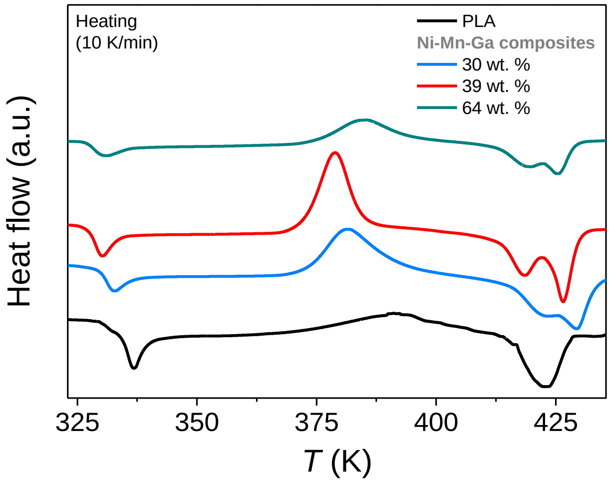

Figure 7.4. DSC curves of PLA and Ni-Mn-Ga composite samples upon heating.

Figure 7.5 shows the DSC of Ni_2MnGa fillers for cooling and heating experiments to dedicate only to its thermal profile. Both branches show a temperature difference between their peak values of 22.2 K, related to the hysteretic martensitic transformation. Furthermore, the peaks are noticeably smooth and have associated modest latent heat.

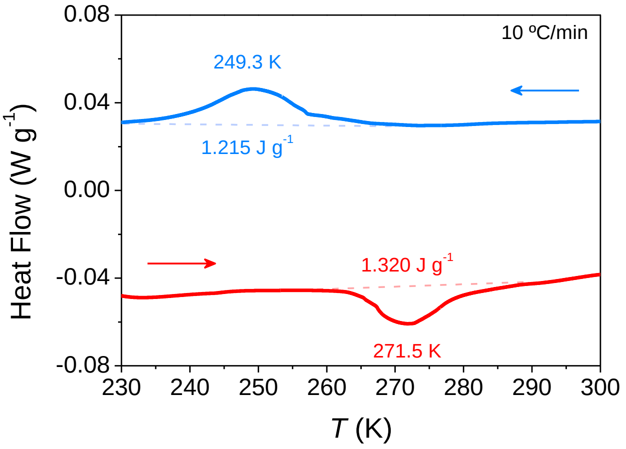

Figure 7.5. DSC curves of the Ni-Mn-Ga Heusler alloy powder.

7.1.3 Magnetic and magnetocaloric characterization

The magnetic properties of the off-stoichiometry Ni_2MnGa powder have been investigated through the analysis of the MCE. As usual, $M(H)$ curves at different isotherms were measured to obtain ΔS_{iso} by following a discontinuous heating protocol due to the possible occurrence of a FOPT. **Figure 7.6 (a)** shows the measured $M(H)$ curves, at different constant temperatures, by sweeping the magnetic field up to 5 T, while the numerically constructed $M(T)$ curves (with data extracted from $M(H)$ measurements) are shown in **Figure 7.6 (b)**.

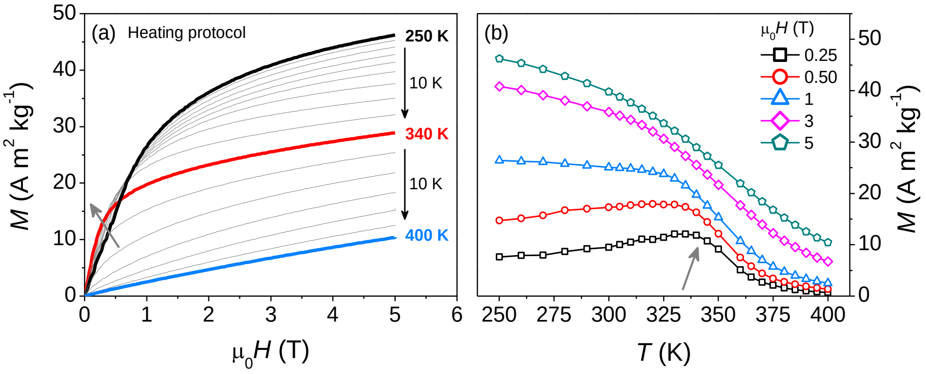

Figure 7.6. (a) Field dependence of magnetization at different temperatures of the raw Ni_2MnGa powder by applying a discontinuous measurement protocol. **(b)** Constructed $M(T)$ curves obtained by interpolation of the $M(H)$ curves of **(a)**.

In both cases, a gradual decrease of magnetization with increasing temperature is observed, similar to the response of a Curie transition. However, the features indicated with gray arrows in both panels of **Figure 7.6** suggest the presence of the martensitic transition. The low temperature phase in Ni_2MnGa has a lower crystalline symmetry compared to that of the high temperature one, which leads to a noticeable higher magnetocrystalline anisotropy [149–152]. This is reflected on the crossover of the $M(H)$ curves for low fields in the range 250 – 340 K as observed in **Figure 7.6 (a).** This crossover of the $M(H)$ curves at low fields appears as an increase of magnetization in the $M(T)$ curves for low fields as indicated in **Figure 7.6 (b)**. This feature has been also observed in high-entropy alloys undergoing a magnetostructural transformation from hexagonal to orthorhombic phase upon cooling, with lower crystalline symmetry and higher magnetocrystalline anisotropy [38,39].

Figure 7.7 (a) shows the isothermal entropy change obtained by applying the Maxwell's relation to the $M(H)$ curves of **Figure 7.6 (a)**. The typical response of a Curie transition is observed, except for the subtle hump indicated with the arrow at ~275 K. This should be related to the previously mentioned features in $M(H)$ and $M(T)$ curves, as well as to the peak observed in the DSC curves upon heating. To ascertain the character of the phase transitions in this material, the exponent n has been analyzed. The temperature dependence of exponent n for different fields is plotted in **Figure 7.7 (b)**, where the characteristic overshoot of $n > 2$ is seen. Although the overshoot gets lower with increasing fields, it is clearly present up to 3 T. After the overshoot, there is a minimum corresponding to the Curie transition of the austenite, after which n finally tends to 2 in the paramagnetic region of the material. Therefore, the occurrence of a FOPT is confirmed in this Heusler alloy powder, in which the response of the Curie transition is predominant.

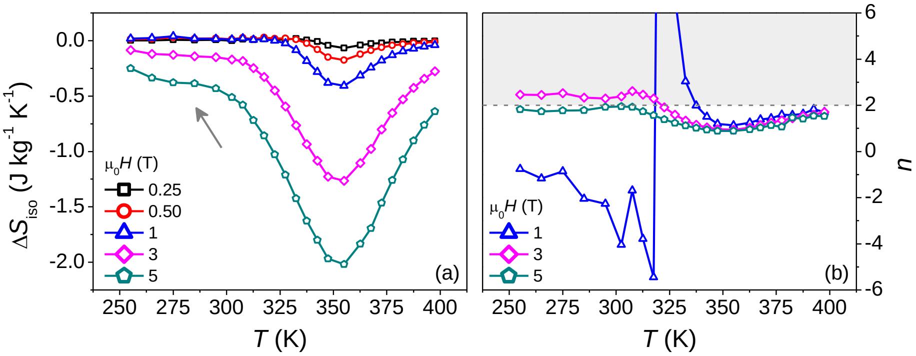

Figure 7.7. (a) Temperature dependence of the isothermal entropy change of the off-stoichiometry Ni_2MnGa powder for different applied fields. **(b)** Temperature dependence of exponent n for different applied fields.

There could be various reasons for the smooth and small response of the martensitic transition. The martensitic transformation takes place by the formation of nucleation centers of the new phase, which require a significant amount of energy, and these centers grow and propagate the transformation.

Therefore, the pulverization of the material can lead to a broader transformation, as the particles are decoupled and each of them has to transform individually, making the propagation of the new phase more gradual [37,153]. It is also reported that the characteristics of the martensitic transition in powdered Heusler alloys are affected by the particle sizes. The transition temperature can change depending on the particle size and the response of the martensitic transition can be significantly decreased or even suppressed [154–157]. Then, a distribution of particle sizes could lead to a distribution of transition temperatures that make the transition appears wider and less abrupt. Additionally, there is the possibility of compositional inhomogeneities which would require a homogenization heat treatment after the atomization process.

To check if the method previously used to obtain the wt. % of fillers based on the comparison of the $M(H)$ curves of the powder and composites is also valid in this case, $M(H)$ curves of both types of samples have been compared at a constant temperature of 300 K, as shown in **Figure 7.8**.

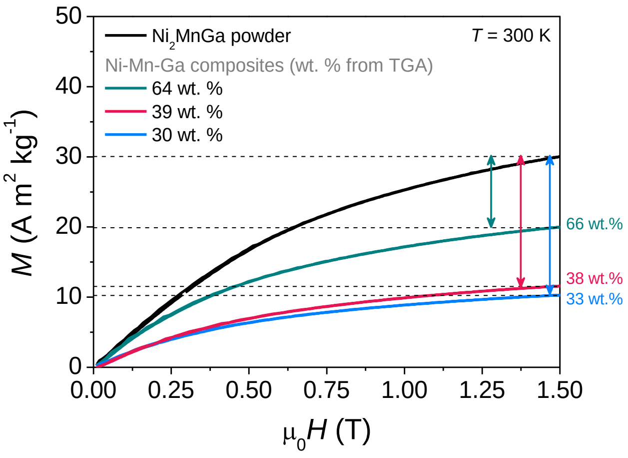

Figure 7.8. First quadrant of the $M(H)$ hysteresis loop of the raw Ni_2MnGa powder (compacted in a silver capsule) and the different composite filaments. The mass fraction of fillers in the composites is obtained by comparing their saturation magnetization per unit mass with that of the raw powder.

The wt. % obtained from the magnetic measurements are 33, 38, and 66 for the filaments with 30, 39, and 64 wt. % according to the TGA measurements, respectively. The good agreement between the results from the two techniques proves that the used Ni_2MnGa powder preserves the original magnetization at room temperature after the manufacturing of the filaments.

However, Ni_2MnGa also undergoes a magnetostructural phase transition so the MCE characterization of the composites can confirm if the thermomagnetic behavior of the fillers is preserved upon the fabrication of the composite filaments. The comparison of the MCE of raw powder and composite samples is shown in **Figure 7.9**, making evident that the magnetocaloric response of the fillers is retained.

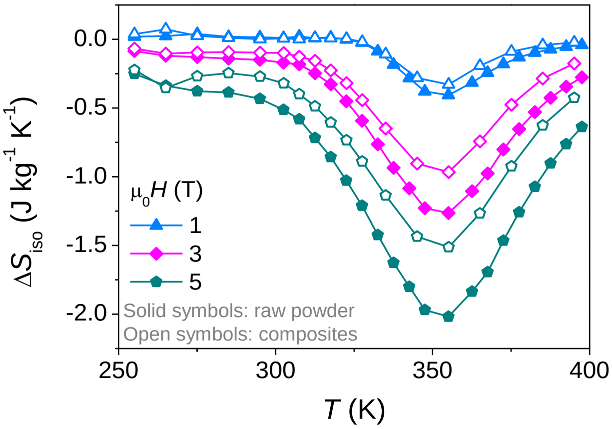

Figure 7.9. $\Delta S_{iso}(T)$ upon heating of the raw Ni_2MnGa powder (solid symbols) and composite of 64 wt. % (wt. % from TGA) (open symbols).

7.2 PLA composite filaments with magnetocaloric La(Fe,Si)$_{13}$-H fillers

A viable alternative material for magnetocaloric applications is hydrogenated La(Fe,Si)$_{13}$. Therefore, it is meaningful to validate the possibility of incorporating it in polymer-based composites.

7.2.1 Filament fabrication

Analogously to the previously presented Heusler-containing filaments, gas atomized and subsequently hydrogenated La(Fe,Si)$_{13}$-H powder, kindly provided by Erasteel (France), has constituted the fillers for the custom-made PLA capsules in the feedstock for the extruder. In this case, only one concentration has been prepared due to the limited amount of available powder material. The feedstock consisted solely of the filled capsules with the design that previously allowed to reach a filling fraction of 64 wt. % of Ni-Mn-Ga particles.

For the proper extrusion of the filament, it was also needed to lower the temperatures of the different heating zones of the extruder, using values of 438 K – 445 K – 445 K – 438 K. These are even slightly lower than those required for the extrusion of PLA + Ni$_2$MnGa composites. As in the previous cases, this is an indication of the decrease of the melt viscosity of the composite with respect to pure PLA.

Figure 7.10 (a) shows a SEM image of the hydrogenated La(Fe,Si)$_{13}$ powder. Powder particles have more irregular shapes in comparison with the powders used previously. This is due to the inclusion of interstitial H atoms, which causes the decrepitation of the material and produces its final morphology of irregular powder [158,159]. An additional effect that might influence powder shape is the fact that the FOPT of the powder occurs at room temperature, making that numerous successive phase transitions with associated volume change might happen even during storage, further contributing to the breaking of the material and its predominantly irregular final shape [160]. Particle size distribution is also comparatively broader than in the previous case. The abovementioned decrepitation, together with the intrinsic brittleness of these intermetallic compounds, make the obtention of durable bulk pieces of hydrogenated La(Fe,Si)$_{13}$ difficult. Therefore, final pieces with a desired shape are usually elaborated by combining the particles with some other material that serves as a matrix and gives consistency to the desired shape [161,162]. **Figure 7.10 (b)** presents a SEM image of the PLA+ La(Fe,Si)$_{13}$-H composite filament. In this case, the particles are also integrated within the polymer matrix, achieving a filling fraction of 55 wt. % (according to TGA measurements). However, in this case, the fillers are less evident among the PLA matrix probably due to their irregular shapes.

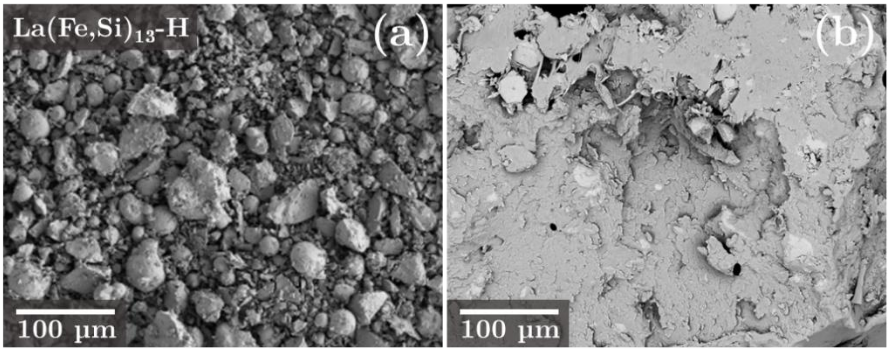

Figure 7.10. SEM micrograph of as-received La(Fe,Si)$_{13}$-H powder from Erasteel (France). **(b)** SEM micrograph of a cross sectional area of the composite filament containing La(Fe,Si)$_{13}$-H fillers.

An important factor that highly affect the performance of La(Fe,Si)$_{13}$ compounds is the presence of impurities other than 1:13 phase, usually α-Fe.

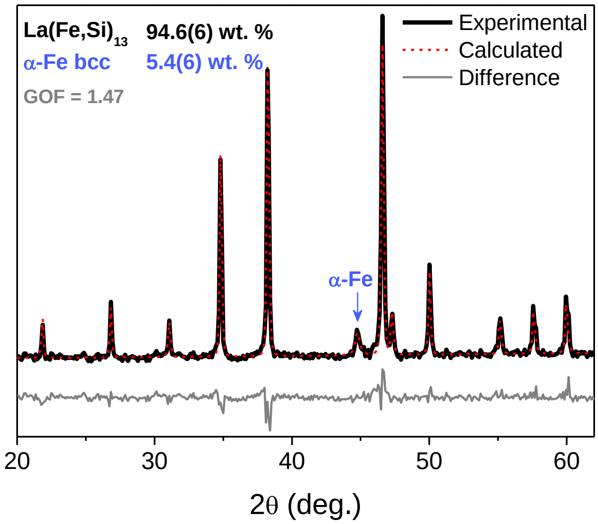

Figure 7.11. XRD spectra including the results of the Rietveld refinement of the as-received La(Fe,Si)$_{13}$-H powder.

The phase composition of the raw powder has been analyzed using XRD with results shown in **Figure 7.11.** The Rietveld refinement of the XRD spectra indicates the presence of a 5.4(6) wt. % of α-Fe (bcc).

7.2.2 Thermal analysis

Figure 7.12 shows the TGA curves of PLA and PLA + La(Fe,Si)$_{13}$-H composite. The remaining mass after the PLA degradation in this case leads to a 55 wt. % of fillers.

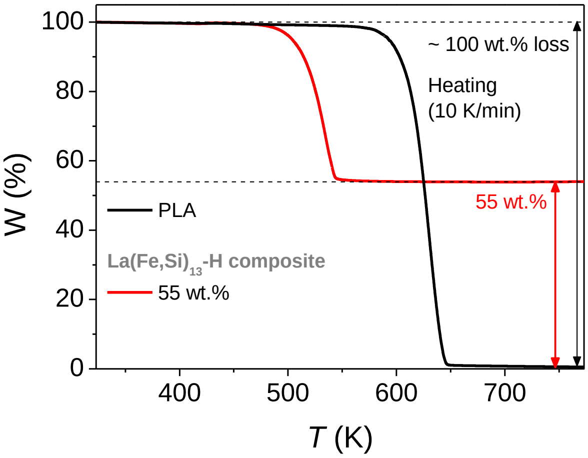

Figure 7.12. TGA curves upon heating of pure PLA and PLA-based composite containing hydrogenated La(Fe,Si)$_{13}$ powder.

Despite the same design of capsules was used, the lower filling fraction in this case (vs. 64 wt. % in the case of Ni$_2$MnGa) is due to two effects: a lower density of this material (~6.2 and ~8.2 g cm^{-3} for La(Fe,Si)$_{13}$-H and Ni$_2$MnGa, respectively) and a lower packing density of the La(Fe,Si)$_{13}$-H powder in the capsules due to their irregular particle shapes. The thermal degradation of PLA is shifted to lower temperatures, occurring in a single step. No additional alteration of the TGA curve of the composite that could be related to the de-hydrogenation of the powder is detected. The de-hydrogenation in these compounds occurs at temperatures in the range 740 – 870 K [158], much above the degradation of PLA in this composite and, therefore, above its processing temperature. This is beneficial for the production of printable magnetocaloric filaments.

Figure 7.13 shows the DSC curves upon heating of samples of PLA and PLA + La(Fe,Si)$_{13}$-H filament.

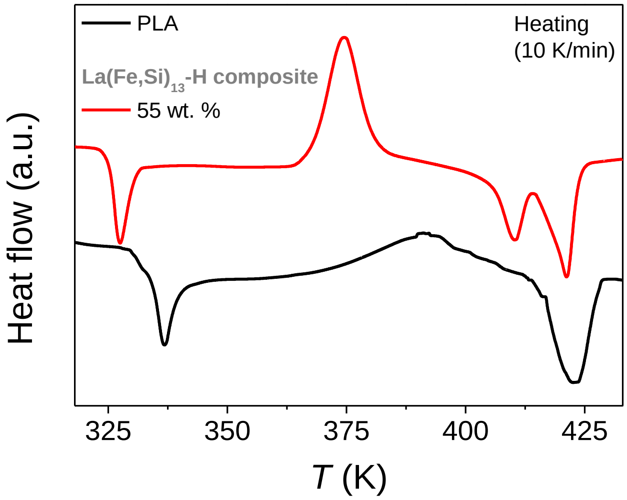

Figure 7.13. Differential scanning calorimetry curves of PLA and PLA + La(Fe,Si)$_{13}$-H composite upon heating from room temperature.

The same features of previously studied composites, especially those with the largest filling fractions of maraging steel and Ni$_2$MnGa particles, can also be enumerated in this case:

1. A glass transition that is displaced to lower temperatures (almost 10 °C).
2. A cold crystallization transition that becomes more prominent in the case of the composite.
3. A melting transition that is divided into two steps due to the melting of the α' phase formed during the cold crystallization.

The DSC curves of the raw La(Fe,Si)$_{13}$-H powder upon cooling and heating are presented in **Figure 7.14**. Both branches show relevant peaks with latent heat ~5.2 J g^{-1} that is associated to the magnetoelastic transformation of the La(Fe,Si)$_{13}$-H system. A transformation is observed at room temperature, thanks to the effect of the interstitial H atoms. The hysteresis of the transformation is small, with peaks that are separated less than 5 K.

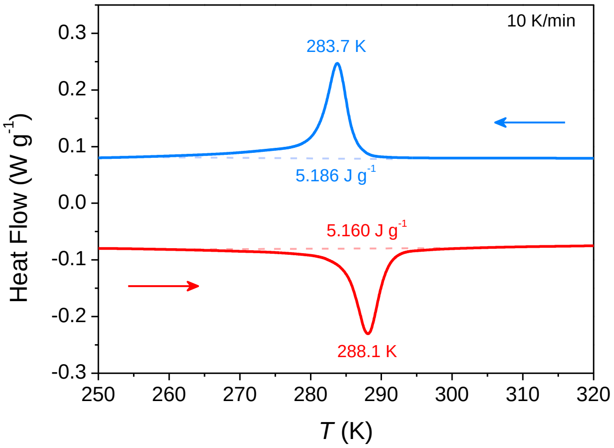

Figure 7.14. DSC curves of La(Fe,Si)-H powder upon cooling and heating.

7.2.3 Magnetic and magnetocaloric characterization

The magnetic properties of the raw La(Fe,Si)$_{13}$-H powder and composite has been studied through the ΔS_{iso} and the exponent n. The curves of $\Delta S_{iso}(T)$ and $n(T)$ for an applied magnetic field of 1.5 T are shown in **Figure 7.15 (a)-(b)**, respectively. With respect to ΔS_{iso}, an almost perfect overlap is obtained for the curves upon cooling and heating, indicating a negligible hysteresis in terms of the magnetocaloric response. The ΔS_{iso}^{pk} values of the raw La(Fe,Si)$_{13}$-H powder are -11.37 and -10.83 J kg^{-1} K^{-1} for heating and cooling, while those of the composite, when considering the total mass of the sample —PLA plus magnetocaloric powder— are -6.67 and -6.17 J kg^{-1} K^{-1} for heating and cooling, respectively. However, when the mass of active magnetocaloric powder is used (55 wt. % of the total mass as previously obtained by TGA), the composite samples have ΔS_{iso}^{pk} of -12.13 and -11.23 J kg^{-1} K^{-1} for heating and cooling, respectively. These values agree well with those of the pure powder. Additionally, the peak temperatures of the powder and composite are the same and equal to 279 K. These results confirm that the La(Fe,Si)$_{13}$-H powder remains unaltered during and after the extrusion process, without any evidence of de-hydrogenation (which would significantly alter the transition temperature).

The exponent n has been calculated using the ΔS_{iso} curves of powder and composite upon heating, as shown in **Figure 7.15 (b)**. Starting from low temperatures, exponent n equals to 1 in the ferromagnetic state of the material, after which the overshoot of $n > 2$ indicates the first-order character of the transformation. At higher temperatures, a trend to $n = 2$ is not observed, as is expected in the paramagnetic state of the material. This behavior of exponent n curves at high temperature makes evident the presence of the ferromagnetic α-Fe phase indicated previously with XRD analysis of the powder in **Figure 7.11Figure 7.11**. This phase contributes with 1 to the exponent n in the studied temperature range so that the values in the paramagnetic region of the La(Fe,Si)$_{13}$-H are still well below 2.

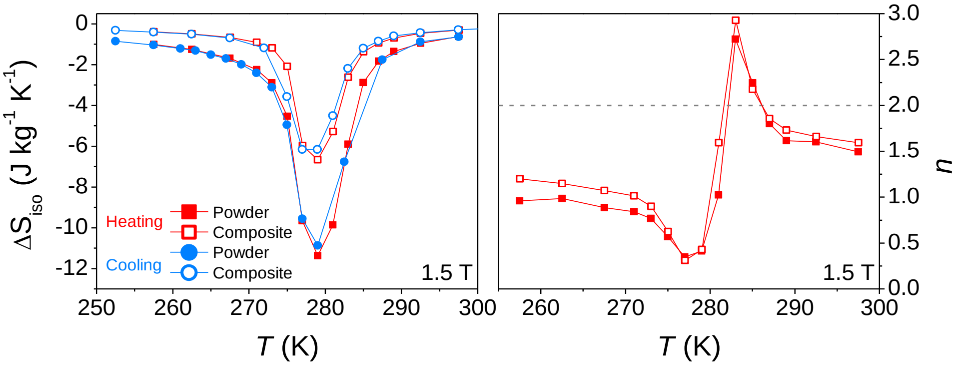

Figure 7.15. (a) $\Delta S_{iso}(T)$ upon cooling and heating of the raw La(Fe,Si)$_{13}$-H powder (solid symbols) and PLA + La(Fe,Si)$_{13}$-H composite (open symbols). **(b)** Temperature dependence of exponent n of powder and composite samples obtained from the $\Delta S_{iso}(T)$ in heating mode.

The large MCE of this La(Fe,Si)$_{13}$-H powder is due to the first-order character of the magnetic transformation (confirmed by the overshoot of exponent $n > 2$). In turn, the low values at the overshoot of n as well as its value at the minimum of ~0.34 indicate that the material stoichiometry is close to the critical composition, whose associated n value at the minimum is 0.4 [49,163,164]. This explains the negligible hysteresis in the magnetocaloric response.

7.3 Conclusions

The procedure developed for the manufacturing of composite filaments for AM has been employed to produce magnetocaloric composite filaments. These have been prepared using company-produced samples of powdered 1) off-stoichiometric Ni_2MnGa Heusler alloy and 2) $La(Fe,Si)_{13}$-H.

The comparison of the magnetocaloric responses of the powder and composite filaments reveals that the functional response is retained for both off-stoichiometric Ni_2MnGa Heusler alloy and $La(Fe,Si)_{13}$-H cases. This confirms that the manufacturing method does not alter the characteristics of the fillers, retaining the thermomagnetic phase transition unaltered with respect to both the transition temperature and the response. In the special case of the $La(Fe,Si)_{13}$-H powder, the hydrogenation, that is essential for the thermomagnetic transition to occur at room temperature, is not affected by the manufacturing of the filament, clarifying one of the main concerns about the validity of the manufacturing procedure.

8 General conclusions

This PhD thesis aims to study of thermomagnetic phase transitions of multiphase magnetocaloric materials, paying special attention to the consequences on the magnetocaloric response in the cases of overlapping phase transitions and to the analysis of the thermal hysteresis underlying FOPTs. The use of magnetic and magnetocaloric materials in the raising 3D-printing technology is also proposed. The main conclusions of the various parts are as follows:

1. Multiphase magnetocaloric materials with Curie transitions close to each other

- In such composites, the combination of phases with Curie transitions close to each other can enhance the performance of SOPT materials when used in devices working according to the Ericsson refrigeration cycle. Although the maximum MCE of the composite reduces as compared to the individual single phase, its increased temperature span in the resulting convoluted response can increase the RC.

  This occurs in the developed $Gd_{100-x}Pd_x$ (x=5, 10, 15, 20) composites that contain Gd + Gd_7Pd_3 phases with Curie transitions separated by ~40 K. A 10 % improvement of the RC with respect to pure Gd is observed for the composite $Gd_{80}Pd_{20}$, in which the higher transition temperature phase, Gd_7Pd_3, has a higher weight fraction than Gd.
- For such materials with overlapping phase transitions, the typical scaling laws of the MCE would not work and the lack of collapse of the rescaled $\Delta S_{iso}/\Delta S_{iso}^{pk}$ curves should not be misinterpreted as a signature of non-SOPT. A method based on the scaling laws has been developed and applied to the $Gd_{80}Pd_{20}$ composite to deconvolute the responses of the overlapping Curie transitions. The partial collapse of the magnetocaloric response of each of the phase transitions has been exploited to reconstruct each of them, including a procedure to take into account and correct the cross-effects between phases.

- This deconvolution allows the actual response of SOPTs to be obtained in the case of phase overlap as well as other cases when the multiple phases in the composites are unintentional but due to inhomogeneities.

2. Magnetocaloric materials undergoing a magnetostructural transformation (FOPT) that occurs close to the Curie transitions of the structural phases (SOPT)

- This is another commonly found case of magnetocaloric materials showing various thermomagnetic phase transitions. The vicinity of these multiple phase transitions is highly dependent on the material composition in the studied case of $Ni_{49+x}Mn_{36-x}In_{15}$ (x = 0, 0.5, 1, 1.5 and 2) Heusler alloys. They undergo a magnetostructural transformation from low temperature martensitic phase to higher temperature austenite of higher magnetization. As the temperature of the FOPT increases with the e/a ratio while the Curie transitions of the martensitic and austenitic phases remain almost invariant, varying phase overlap is obtained in the alloy series.
- For the sample with e/a = 7.874, its magnetocaloric response shows a positive artifact-like spike embedded into the conventional MCE of the Curie transition of the austenite. The occurrence of the structural transformation in this case is experimentally evidenced by means of XRD at different temperatures and AC susceptibility experiments. These later reveal that for low fields the FOPT occurs when both phases are paramagnetic. Using the recent exponent n method for the determination of the order of thermomagnetic phase transitions in this complex case, a clear observation of the FOPT fingerprint further confirms that the MCE spike is not an artifact. The results of the application of this recent exponent n method have been compared to those from the usual Banerjee's criterion. It has been shown that the exponent n criterion possesses higher sensitivity as much lower fields are required to unequivocally determine the FOPT character of the overlapping FOPT.
- Furthermore, the earlier-mentioned deconvolution procedure when applied to the case of overlapping FOPT and SOPT in one of the alloys of the series (with $e/a = 7.826$) allows the separation of the Curie transition from the FOPT. This helps to obtain the appropriate

magnitude of the inverse MCE arising from the FOPT, which was formerly seen decreasing with increasing magnetic fields above 3T in this sample. It is therefore proven that such behavior is due to the competition between inverse and conventional MCE (the latter arises from the Curie transition of the austenite).

- Despite materials undergoing magnetic FOPT can show a significantly higher MCE than those showing SOPT, the thermal hysteresis present in FOPTs is a detrimental characteristic for the applicability of these materials in cyclic operations. The thermal hysteresis in two Heusler alloys with compositions slightly different and close to the stoichiometry $Ni_{50}Mn_{34}In_{16}$ has been investigated by means of the TFORC technique. Similar to previous Ni-Mn-In series, samples of this new one also presents the hysteretic martensitic transformation producing an inverse MCE with the Curie transition of the austenite located nearby. The combination of experimental results and a simulation model to replicate the behavior of the material made possible the identification and association of the features of the TFORC distributions to the characteristics of thermomagnetic behavior of the samples. The model allows the separation of the structural transformation by only considering the function for the phase fractions and the total magnetic response. It is shown that the main features of the TFORC distributions are related to the characteristics of the structural transformation, reflecting its asymmetry and the different transformation rates. Additionally, the non-hysteretic thermomagnetic behavior of the phases also contributes to the TFORC distribution by adding extra asymmetry to the transformation.

3. Fabrication of magnetocaloric composite filaments for additive manufacturing

- The poor processability of most of the relevant magnetocaloric materials can be overcome through AM. FDM is a good choice among the AM methods as it can resolve the issues related to the rapid degradation under cyclic thermal conditions in FOPT systems as the functional material is embedded in a polymer matrix that serves as structural support.

- A lab-scale method consisting of custom-made polymer capsules to contain the functional powder has been proposed for the extrusion of the composite filaments with good homogeneity. The proportions of both polymer and functional powder remain constant along the entire extrusion process, allowing the obtention of homogeneous filaments in one single extrusion process. The method has been first validated using soft magnetic maraging steel powder, resulting in an interesting option given the limited possibilities on the market in this sector. The functionality of the fillers is preserved while the characteristics of the polymer are noticeably affected. It is shown that the viscosity of the composite is reduced with the addition of fillers.

The validated procedure is subsequently used for the manufacturing of composite filaments containing powder of 1) Ni-Mn-Ga Heusler alloy and 2) $La(Fe,Si)_{13}$-H. The magnetocaloric responses as well as the various thermomagnetic phase transitions are all maintained in the magnetocaloric filament composites as compared to those of the pristine powder. It has to be noted that the unaltered functional behavior and thermomagnetic phase transition temperatures of $La(Fe,Si)_{13}$-H composite filaments further indicate the remarkability of the customized encapsulation feedstock methodology.

List of publications

1. **Á. Díaz-García**, J.Y. Law, L. Żrodowski, B. Morończyk, R. Wróblewski, V. Franco, Polymer-based composites containing magnetocaloric NiMnGa Heusler alloy fillers for additive manufacturing, *In Preparation* (2022).

2. **Á. Díaz-García**, L.M. Moreno-Ramírez, J.Y. Law, C. Mayer, V. Franco, Use of La(Fe,Si)$_{13}$-H powder for the manufacturing of magnetocaloric composite filaments for fused deposition modeling, *In Preparation* (2022).

3. **Á. Díaz-García**, J. Y. Law, M. Félix, A. Guerrero, V. Franco, Functional, thermal, and rheological properties of polymer-based magnetic composite filaments for additive manufacturing, *Submitted Mater. Des.* (2021).

4. **Á. Díaz-García**, J. Y. Law, A. K. Giri, V. Franco, Deconvolution of overlapping first and second order phase transitions in a NiMnIn Heusler alloy using the scaling laws of the magnetocaloric effect, *J. Alloys Compd.*, 871 (2021) 159621.

5. **Á. Díaz-García**, L.M. Moreno-Ramírez, J. Y. Law, F. Albertini, S. Fabbrici, V. Franco, Characterization of thermal hysteresis in magnetocaloric NiMnIn Heusler alloys by Temperature First Order Reversal Curves (TFORC), *J. Alloys Compd.*, 867 (2021) 159184.

6. **Á. Díaz-García**, P. Gębara, J. Y. Law, V. Franco, Phase Deconvolution of Multiphasic Materials by the Universal Scaling of the Magnetocaloric Effect, *JOM*, 72 (2020) 2845–2852.

7. **Á. Díaz-García**, J. Y. Law, A. Cota, A. Bellido-Correa, J. Ramírez-Rico, R. Schäfer, V. Franco, Novel procedure for laboratory scale production of composite functional filaments for additive manufacturing, *Mater. Today Commun.*, 24 (2020) 101049.

8. P. Gębara, **Á. Díaz-García**, J. Y. Law, V. Franco, Magnetocaloric response of binary Gd-Pd and ternary Gd-(Mn,Pd) alloys, *J. Magn. Magn. Mater.*, 500 (2020) 166175.

9. J. Y. Law, **Á. Díaz-García**, L. M. Moreno-Ramírez, V. Franco, A. Conde, A. K. Giri, How concurrent thermomagnetic transitions can affect magnetocaloric effect: the $Ni_{49+x}Mn_{36-x}In_{15}$ Heusler alloy case, *Acta Mater.*, 166 (2019) 459-465.

The contents of the following co-authored publications are not included in this thesis:

1. J. Y. Law, **Á. Díaz-García**, L.M. Moreno-Ramírez, V. Franco, Increased magnetocaloric response of FeMnNiGeSi high-entropy alloys, *Acta Mater.,* 212 (2021) 116931.

2. J.Y. Law, L.M. Moreno-Ramírez, **Á. Díaz-García**, A. Martín-Cid, S. Kobayashi, S. Kawaguchi, T. Nakamura, V. Franco, MnFeNiGeSi High-Entropy Alloy with Large Magnetocaloric Effect, *J. Alloys Compd.,* 855 (2021) 157424.

3. L.M. Moreno-Ramírez, **Á. Díaz-García**, J. Y. Law, A. K. Giri, V. Franco, Hysteresis, latent heat and cycling effects on the magnetocaloric response of $(NiMnSi)_{0.66}(Fe2Ge)_{0.34}$ alloy, *Intermetallics*, 131 (2021) 107083.

International activities

1. **Á. Díaz-García**, J. Y. Law, L. M. Moreno-Ramírez, R. Schäfer, V. Franco, Low temperature annealing enhancing the magnetocaloric response of FeMnNiGeSi HEAs, *25th Soft Magnetic Materials Conference (SMM25),* Grenoble, France, May 2 – 5 (2022). *Oral communication*

2. V. Franco, L.M. Moreno-Ramírez, **Á. Díaz-García**, J.Y. Law, Thermal hysteresis of magnetocaloric materials studied by TFORC, *Magnet 2022 Conference*, Florence, Italy, April 11 – 13 (2022). *Oral communication*

3. J.Y. Law, **Á. Díaz-García**, L.M. Moreno-Ramírez, V. Franco**,** Optimization of rare earth free High Entropy Alloys for enhanced magnetocaloric response, *Magnet 2022 Conference*, Florence, Italy, April 11 – 13 (2022). *Oral communication*

4. **Á. Díaz-García**, J. Y. Law, M. Félix, A. Guerrero, V. Franco, Functional and processing-related properties of polymer-based magnetic composite filaments for additive manufacturing, *Annual European Rheology Conference 2022 (AERC22),* Seville, Spain, April 26 – 28 (2022). *Poster presentation*

5. **Á. Díaz-García**, J. Y. Law, M. Félix, A. Guerrero, V. Franco, Manufacturing and characterization of soft magnetic composite filaments for additive manufacturing, *2022 Joint MMM-INTERMAG Conference*, New Orleans, USA, January 10 – 14 (2022). *Oral communication*

6. **Á. Díaz-García**, J. Y. Law, L. Żrodowski, B. Morończyk, R. Wróblewski, V. Franco, Magnetocaloric Heusler Alloy Composites for Fused

Deposition Modeling, *2022 Joint MMM-INTERMAG Conference*, New Orleans, USA, January 10 – 14 (2022). *Oral communication*

7. **Á. Díaz-García**, J. Y. Law, A.K. Giri, V. Franco, Deconvolution of first and second order phase transitions using the scaling laws of the magnetocaloric effect, *The International Magnetic Conference 2021 (INTERMAG 2021)*, Virtual conference, April 26 – 30 (2021). *Oral communication*

8. J.Y. Law, **Á. Díaz-García**, L.M. Moreno-Ramírez, V. Franco, One order of magnitude improvement of the magnetocaloric effect of rare-earth-free HEAs*, 2nd World Congress on High-Entropy Alloys (HEA2021)*, Charlotte, USA, Dec 5 - 8 (2021). *Oral communication*

9. V. Franco, **Á. Díaz-García**, L.M. Moreno-Ramírez, J. Y. Law, S. Fabbrici, F. Albertini, T-FORC as a tool for the characterization of magnetocaloric materials: from experiments to models, *The International Magnetic Conference 2021 (INTERMAG 2021)*, Virtual conference, April 26 – 30 (2021). *Oral communication*

10. J. Y. Law, **Á. Díaz-García**, L.M. Moreno-Ramírez, V. Franco, Overcoming the Limitations of Magnetocaloric Rare-Earth-Free High-Entropy Alloys, *The International Magnetic Conference 2021 (INTERMAG 2021)*, Virtual conference, April 26 – 30 (2021). *Invited oral communication*

11. **Á. Díaz-García**, P. Gębara, J. Y. Law, V. Franco, Deconvolution of overlapping phase transitions in composites using the universal scaling of the magnetocaloric effect, *The European Magnetic Symposia (JEMS 2020)*, Virtual conference, December 7– 11 (2020). *Oral communication*

12. J. Y. Law, **Á. Díaz-García**, A. Cota, J. Ramírez-Rico, Rudolf Schaefer, V. Franco, New lab-made feedstock for magnetic composite filaments for

additive manufacturing, *The European Magnetic Symposia (JEMS 2020)*, Virtual conference, December 7 – 11 (2020). *Poster presentation*

13. **Á. Díaz-García**, P. Gębara, J. Y. Law, V. Franco, Use of the Scaling Laws of the Magnetocaloric Effect to Deconvolute Overlapping Phase Transitions in Biphasic Composites, *The 65th Annual Conference of Magnetism and Magnetic Materials (MMM 2020)*, Virtual conference, November 2 – 6 (2020). *Oral communication*

14. **Á. Díaz-García**, J. Y. Law, L. M. Moreno-Ramírez, V. Franco, A. Conde, A. K. Giri, Ni-Mn-In Heusler alloys with artifact-like magnetocaloric effect due to overlapped thermomagnetic phase transitions, *The 2020 Around-the-Clock Around-the-Globe Magnetics Conference (AtC-AtG 2020)*, Virtual conference, September 27 (2020). *Oral communication*

15. V. Franco, **Á. Díaz-García**, A. Bellido-Correa, A. Cota, J. Ramírez-Rico, J. Y. Law, Composite magnetic filaments for additive manufacturing: a novel procedure for laboratory scale production, *2020 TMS Annual Meeting & Exhibition*, San Diego, USA, February 23 – 27 (2020). *Invited oral communication*

16. **Á. Díaz-García**, J. Y. Law, L. M. Moreno-Ramírez, V. Franco, A. Conde, A. K. Giri, When actual effects look like artifacts: Deconvolution of the concurrent transitions in Ni-Mn-In Heusler alloys, *2019 Delft Days on Magnetocalorics*, Delft, The Netherlands, November 18 – 19 (2019). *Oral communication*

17. **Á. Díaz-García**, A. Bellido-Correa, A. Cota, J. Ramírez-Rico, J. Y. Law, V. Franco, Novel procedure for fabricating composite filaments with embedded magnetic particles for additive manufacturing, *24th Soft Magnetic Materials Conference (SMM 2019)*, Poznan, Poland, September 04 – 07 (2019). *Oral communication*

18. P. Gębara, **Á. Díaz-García**, J. Y. Law, V. Franco, Magnetocaloric response of biphasic GdPd alloys, *24th Soft Magnetic Materials Conference (SMM 2019)*, Poznan, Poland, September 04 – 07 (2019). *Poster presentation*

19. **Á. Díaz-García**, J. Y. Law, V. Franco, A. Conde, A. K. Giri, The AC susceptibility of the overlapping thermomagnetic phase transitions in Ni-Mn-In Heusler alloys, *2019 IEEE Magnetics Summer School*, Richmond, USA, June 02 – 07 (2019). *Poster presentation*

20. **Á. Díaz-García**, J. Y. Law, V. Franco, A. Conde, AC Susceptibility study of overlapping thermomagnetic transitions in NiMnIn Heusler alloy, *2019 Joint MMM-INTERMAG Conference*, Washington DC, USA, January 14 – 18 (2019). *Oral communication*

References

[1] V.K. Pecharsky, K.A. Gschneidner, Magnetocaloric effect and magnetic refrigeration, *J. Magn. Magn. Mater.* 200 (1999) 44–56.

[2] E. Brück, Magnetocaloric Refrigeration at Ambient Temperature, in: Handb. Magn. Mater., Volume 17, 2007: pp. 235–291.

[3] O. Gutfleisch, M.A. Willard, E. Brück, C.H. Chen, S.G. Sankar, J.P. Liu, Magnetic materials and devices for the 21st century: Stronger, lighter, and more energy efficient, *Adv. Mater.* 23 (2011) 821–842.

[4] V. Franco, J.S. Blázquez, B. Ingale, A. Conde, The Magnetocaloric Effect and Magnetic Refrigeration Near Room Temperature: Materials and Models, *Annu. Rev. Mater. Res.* 42 (2012) 305–342.

[5] V. Franco, J.S. Blázquez, J.J. Ipus, J.Y. Law, L.M. Moreno-Ramírez, A. Conde, Magnetocaloric effect: From materials research to refrigeration devices, *Prog. Mater. Sci.* 93 (2018) 112–232.

[6] B. Yu, M. Liu, P.W. Egolf, A. Kitanovski, A review of magnetic refrigerator and heat pump prototypes built before the year 2010, *Int. J. Refrig.* 33 (2010) 1029–1060.

[7] C. Zimm, A. Jastrab, A. Sternberg, V. Pecharsky, K. Gschneidner, M. Osborne, I. Anderson, Description and Performance of a Near-Room Temperature Magnetic Refrigerator, in: Adv. Cryog. Eng., Springer US, Boston, MA, MA, 1998: pp. 1759–1766.

[8] Global electricity consumption continues to rise faster than population: <https://www.eia.gov/todayinenergy/detail.php?id=44095>, (2020).

[9] https://flowcharts.llnl.gov/commodities/energy, (2019).

[10] https://www.eia.gov/totalenergy/data/monthly/, (2022).

[11] G. Venkatarathnam, Cooling and liquefaction of air and its constituents, in: 2008: pp. 221–249.

[12] M.S. Khan, I.A. Karimi, D.A. Wood, Retrospective and future perspective of natural gas liquefaction and optimization technologies contributing to efficient LNG supply: A review, *J. Nat. Gas Sci. Eng.* 45 (2017) 165–188.

[13] A.M. Tishin, Y.I. Spichkin, V.I. Zverev, P.W. Egolf, A review and new perspectives for the magnetocaloric effect: New materials and local heating and cooling inside the human body, *Int. J. Refrig.* 68 (2016) 177–186.

[14] M. Barbic, S.J. Dodd, H.D. Morris, N. Dilley, B. Marcheschi, A. Huston, T.D. Harris, A.P. Koretsky, Magnetocaloric materials as switchable high contrast ratio MRI labels, *Magn. Reson. Med.* 81 (2019) 2238–2246.

[15] P.W. Egolf, A. Kitanovski, M. Diebold, C. Gonin, D. Vuarnoz, Magnetic power conversion with machines containing full or porous wheel heat exchangers, *J. Magn. Magn. Mater.* 321 (2009) 758–762.

[16] A. Kitanovski, Applications on Magnetocaloric Materials, in: Encycl. Smart Mater., Elsevier, 2022: pp. 418–432.

[17] V. Franco, Magnetocaloric Characterization of Materials, in: Magn. Meas. Tech. Mater. Charact., Springer International Publishing, Cham, 2021: pp. 697–726.

[18] M.E. Wood, W.H. Potter, General analysis of magnetic refrigeration and its optimization using a new concept: maximization of refrigerant capacity, *Cryogenics (Guildf).* 25 (1985) 667–683.

[19] W.F. Giauque, A thermodynamic treatment of certain magnetic effects. A proposed method of producing temperatures considerably below 1^o absolute, *J. Am. Chem. Soc.* 49 (1927) 1864–1870.

[20] W.F. Giauque, D.P. MacDougall, Attainment of Temperatures Below 1^o Absolute by Demagnetization of Gd2(SO4)3 H2O, *Phys. Rev.* 43 (1933) 768.

[21] G. Jaeger, The Ehrenfest Classification of Phase Transitions: Introduction and Evolution, *Arch. Hist. Exact Sci.* 53 (1998) 51–81.

[22] S.Y. Dan'kov, A.M. Tishin, V.K. Pecharsky, K.A. Gschneidner,

Magnetic phase transitions and the magnetothermal properties of gadolinium, *Phys. Rev. B*. 57 (1998) 3478–3490.

[23] K.A. GschneidnerJr, V.K. Pecharsky, A.O. Tsokol, Recent developments in magnetocaloric materials, *Reports Prog. Phys.* 68 (2005) 1479–1539.

[24] G. V. Brown, Magnetic heat pumping near room temperature, *J. Appl. Phys.* 47 (1976) 3673–3680.

[25] A. Smaili, R. Chahine, Composite materials for Ericsson-like magnetic refrigeration cycle, *J. Appl. Phys.* 81 (1997) 824–829.

[26] J.Y. Law, L.M. Moreno-Ramírez, J.S. Blázquez, V. Franco, A. Conde, Gd+GdZn biphasic magnetic composites synthesized in a single preparation step: Increasing refrigerant capacity without decreasing magnetic entropy change, *J. Alloys Compd.* 675 (2016) 244–247.

[27] J.Y. Law, V. Franco, Magnetocaloric Composite Materials, in: Encycl. Mater. Compos., Elsevier, 2021: pp. 461–472.

[28] Z.C. Xu, G.X. Lin, J.C. Chen, A GdxHo1-x-based composite and its performance characteristics in a regenerative Ericsson refrigeration cycle, *J. Alloys Compd.* 639 (2015) 520–525.

[29] R. Caballero-Flores, V. Franco, A. Conde, K.E. Knipling, M.A. Willard, Optimization of the refrigerant capacity in multiphase magnetocaloric materials, *Appl. Phys. Lett.* 98 (2011) 102505.

[30] V.K. Pecharsky, K.A. Gschneidner, Jr., Giant magnetocaloric effect in Gd5 (Si2 Ge2), *Phys. Rev. Lett.* 78 (1997) 4494–4497.

[31] W. Ito, Y. Imano, R. Kainuma, Y. Sutou, K. Oikawa, K. Ishida, Martensitic and magnetic transformation behaviors in Heusler-type NiMnIn and NiCoMnIn metamagnetic shape memory alloys, *Metall. Mater. Trans. A Phys. Metall. Mater. Sci.* 38 (2007) 759–766.

[32] A. Planes, L. Mañosa, M. Acet, Magnetocaloric effect and its relation to shape-memory properties in ferromagnetic Heusler alloys, *J. Phys. Condens. Matter*. 21 (2009) 233201.

[33] T. Gottschall, K.P. Skokov, B. Frincu, O. Gutfleisch, Large reversible

magnetocaloric effect in Ni-Mn-In-Co, *Appl. Phys. Lett.* 106 (2015) 021901.

[34] S. Fujieda, A. Fujita, K. Fukamichi, Large magnetocaloric effect in La(FexSi1-x) 13 itinerant-electron metamagnetic compounds, *Appl. Phys. Lett.* 81 (2002) 1276–1278.

[35] F. Guillou, H. Yibole, A. Kamantsev, G. Porcari, J. Cwik, V. Koledov, N.H. Van Dijk, E. Brück, Field Dependence of the Magnetocaloric Effect in MnFe(P,Si) Materials, *IEEE Trans. Magn.* 51 (2015) 51–54.

[36] C.L. Zhang, H.F. Shi, E.J. Ye, Y.G. Nie, Z.D. Han, B. Qian, D.H. Wang, Magnetostructural transition and magnetocaloric effect in MnNiSi-Fe 2 Ge system, *Appl. Phys. Lett.* 107 (2015) 212403.

[37] L.M. Moreno-Ramírez, Díaz-García, J.Y. Law, A.K. Giri, V. Franco, Hysteresis, latent heat and cycling effects on the magnetocaloric response of (NiMnSi)0.66(Fe2Ge)0.34 alloy, *Intermetallics*. 131 (2021) 107083.

[38] J.Y. Law, L.M. Moreno-Ramírez, Á. Díaz-García, A. Martín-Cid, S. Kobayashi, S. Kawaguchi, T. Nakamura, V. Franco, MnFeNiGeSi high-entropy alloy with large magnetocaloric effect, *J. Alloys Compd.* 855 (2021) 157424.

[39] J.Y. Law, Á. Díaz-García, L.M. Moreno-Ramírez, V. Franco, Increased magnetocaloric response of FeMnNiGeSi high-entropy alloys, *Acta Mater.* 212 (2021) 116931.

[40] S. Singh, L. Caron, S.W. D'Souza, T. Fichtner, G. Porcari, S. Fabbrici, C. Shekhar, S. Chadov, M. Solzi, C. Felser, Large Magnetization and Reversible Magnetocaloric Effect at the Second-Order Magnetic Transition in Heusler Materials, *Adv. Mater.* 28 (2016) 3321–3325.

[41] T. Krenke, E. Duman, M. Acet, E.F. Wassermann, X. Moya, L. Mañosa, A. Planes, E. Suard, B. Ouladdiaf, Magnetic superelasticity and inverse magnetocaloric effect in Ni-Mn-In, *Phys. Rev. B*. 75 (2007) 104414.

[42] B. Lu, J. Liu, Elastocaloric effect and superelastic stability in Ni–Mn–In–Co polycrystalline Heusler alloys: hysteresis and strain-rate effects, *Sci. Rep.* 7 (2017) 2084.

[43] L. Mañosa, D. González-Alonso, A. Planes, E. Bonnot, M. Barrio, J.L. Tamarit, S. Aksoy, M. Acet, Giant solid-state barocaloric effect in the Ni-Mn-In magnetic shape-memory alloy, *Nat. Mater.* 9 (2010) 478–481.

[44] E. Stern-Taulats, A. Planes, P. Lloveras, M. Barrio, J. Tamarit, S. Pramanick, S. Majumdar, S. Yüce, B. Emre, C. Frontera, L. Mañosa, Tailoring barocaloric and magnetocaloric properties in low-hysteresis magnetic shape memory alloys, *Acta Mater.* 96 (2015) 324–332.

[45] A. Gràcia-Condal, T. Gottschall, L. Pfeuffer, O. Gutfleisch, A. Planes, L. Mañosa, Multicaloric effects in metamagnetic Heusler Ni-Mn-In under uniaxial stress and magnetic field, *Appl. Phys. Rev.* 7 (2020) 041406.

[46] O. Gutfleisch, T. Gottschall, M. Fries, D. Benke, I. Radulov, K.P. Skokov, H. Wende, M. Gruner, M. Acet, P. Entel, M. Farle, Mastering hysteresis in magnetocaloric materials, *Philos. Trans. R. Soc. A Math. Phys. Eng. Sci.* 374 (2016).

[47] T. Gottschall, E. Stern-Taulats, L. Mañosa, A. Planes, K.P. Skokov, O. Gutfleisch, Reversibility of minor hysteresis loops in magnetocaloric Heusler alloys, *Appl. Phys. Lett.* 110 (2017) 223904.

[48] A. Diestel, R. Niemann, B. Schleicher, K. Nielsch, S. Fähler, Reducing Hysteresis Losses by Heating Minor Loops in Magnetocaloric Ni-Mn-Ga-Co Films, *Energy Technol.* 6 (2018) 1463–1469.

[49] V. Franco, J.Y. Law, A. Conde, V. Brabander, D.Y. Karpenkov, I. Radulov, K. Skokov, O. Gutfleisch, Predicting the tricritical point composition of a series of LaFeSi magnetocaloric alloys via universal scaling, *J. Phys. D. Appl. Phys.* 50 (2017) 414004.

[50] A. Fujita, S. Fujieda, Y. Hasegawa, K. Fukamichi, Itinerant-electron metamagnetic transition and large magnetocaloric effects in La(FexSi1-x)13 compounds and their hydrides, *Phys. Rev. B - Condens. Matter Mater. Phys.* 67 (2003) 1044161–10441612.

[51] A. Smith, C.R.H. Bahl, R. Bjørk, K. Engelbrecht, K.K. Nielsen, N. Pryds, Materials Challenges for High Performance Magnetocaloric Refrigeration Devices, *Adv. Energy Mater.* 2 (2012) 1288–1318.

[52] M.S. Kamran, J. Sun, Y.B. Tang, Y.G. Chen, J.H. Wu, H.S. Wang, Numerical investigation of room temperature magnetic refrigerator using microchannel regenerators, *Appl. Therm. Eng.* 102 (2016) 1126–1140.

[53] T. Lei, K. Engelbrecht, K.K. Nielsen, C.T. Veje, Study of geometries of active magnetic regenerators for room temperature magnetocaloric refrigeration, *Appl. Therm. Eng.* 111 (2017) 1232–1243.

[54] T.D. Ngo, A. Kashani, G. Imbalzano, K.T.Q. Nguyen, D. Hui, Additive manufacturing (3D printing): A review of materials, methods, applications and challenges, *Compos. Part B Eng.* 143 (2018) 172–196.

[55] S.A.M. Tofail, E.P. Koumoulos, A. Bandyopadhyay, S. Bose, L. O'Donoghue, C. Charitidis, Additive manufacturing: scientific and technological challenges, market uptake and opportunities, *Mater. Today.* 21 (2018) 22–37.

[56] S.K. Parupelli, S. Desai, A Comprehensive Review of Additive Manufacturing (3D Printing): Processes, Applications and Future Potential, *Am. J. Appl. Sci.* 16 (2019) 244–272.

[57] W.E. Frazier, Metal Additive Manufacturing: A Review, *J. Mater. Eng. Perform.* 23 (2014) 1917–1928.

[58] J.J. Lewandowski, M. Seifi, Metal Additive Manufacturing: A Review of Mechanical Properties, *Annu. Rev. Mater. Res.* 46 (2016) 151–186.

[59] J.D. Moore, D. Klemm, D. Lindackers, S. Grasemann, R. Träger, J. Eckert, L. Löber, S. Scudino, M. Katter, A. Barcza, K.P. Skokov, O. Gutfleisch, Selective laser melting of La(Fe,Co,Si) 13 geometries for magnetic refrigeration, *J. Appl. Phys.* 114 (2013) 043907.

[60] J. Toman, P. Müllner, M. Chmielus, Properties of as-deposited and heat-treated Ni-Mn-Ga magnetic shape memory alloy processed by directed energy deposition, *J. Alloys Compd.* 752 (2018) 455–463.

[61] V. Laitinen, A. Sozinov, A. Saren, A. Salminen, K. Ullakko, Laser powder bed fusion of Ni-Mn-Ga magnetic shape memory alloy, *Addit. Manuf.* 30 (2019) 100891.

[62] F. Nilsén, I.F. Ituarte, M. Salmi, J. Partanen, S.-P. Hannula, Effect of process parameters on non-modulated Ni-Mn-Ga alloy manufactured using powder bed fusion, *Addit. Manuf.* 28 (2019) 464–474.

[63] X. Wang, M. Jiang, Z. Zhou, J. Gou, D. Hui, 3D printing of polymer matrix composites: A review and prospective, *Compos. Part B Eng.* 110 (2017) 442–458.

[64] P.M. Angelopoulos, M. Samouhos, M. Taxiarchou, Functional fillers in composite filaments for fused filament fabrication: A review, *Mater. Today Proc.* 37 (2019) 4031–4043.

[65] A. El Moumen, M. Tarfaoui, K. Lafdi, Additive manufacturing of polymer composites: Processing and modeling approaches, *Compos. Part B Eng.* 171 (2019) 166–182.

[66] C. Huber, C. Abert, F. Bruckner, M. Groenefeld, O. Muthsam, S. Schuschnigg, K. Sirak, R. Thanhoffer, I. Teliban, C. Vogler, R. Windl, D. Suess, 3D print of polymer bonded rare-earth magnets, and 3D magnetic field scanning with an end-user 3D printer, *Appl. Phys. Lett.* 109 (2016).

[67] A.P. Taylor, C. Velez Cuervo, D.P. Arnold, L.F. Velasquez-Garcia, Fully 3D-printed, monolithic, mini magnetic actuators for low-cost, compact systems, *J. Microelectromechanical Syst.* 28 (2019) 481–493.

[68] R.P. Magisetty, N.S. Cheekuramelli, Additive manufacturing technology empowered complex electromechanical energy conversion devices and transformers, *Appl. Mater. Today*. 14 (2019) 35–50.

[69] D. Khanna, V. Alarcos, V. Callardo, J.I. Pérez-Landazábal, Multifunctional magnetic composites based in meta-magnetic shape memory alloys for 3D printing applications, in: 2022 Joint MMM-INTERMAG Conference, doi: 10.48448/71md-q477, 2022.

[70] S.W. Kwok, K.H.H. Goh, Z.D. Tan, S.T.M. Tan, W.W. Tjiu, J.Y.

Soh, Z.J.G. Ng, Y.Z. Chan, H.K. Hui, K.E.J. Goh, Electrically conductive filament for 3D-printed circuits and sensors, *Appl. Mater. Today*. 9 (2017) 167–175.

[71] A. Dorigato, V. Moretti, S. Dul, S.H. Unterberger, A. Pegoretti, Electrically conductive nanocomposites for fused deposition modelling, *Synth. Met.* 226 (2017) 7–14.

[72] K. Gnanasekaran, T. Heijmans, S. van Bennekom, H. Woldhuis, S. Wijnia, G. de With, H. Friedrich, 3D printing of CNT- and graphene-based conductive polymer nanocomposites by fused deposition modeling, *Appl. Mater. Today*. 9 (2017) 21–28.

[73] T. Rimpongpisarn, W. Wattanathana, K. Sukthavorn, N. Nootsuwan, Y. Hanlumyuang, C. Veranitisagul, A. Laobuthee, Novel luminescent PLA/MgAl2O4:Sm3+ composite filaments for 3D printing application, *Mater. Lett.* 237 (2019) 270–273.

[74] M. Wan, X. Jiang, J. Nie, Q. Cao, W. Zheng, X. Dong, Z.H. Fan, W. Zhou, Phosphor powders-incorporated polylactic acid polymeric composite used as 3D printing filaments with green luminescence properties, *J. Appl. Polym. Sci.* 137 (2020) 1–10.

[75] J.M. Chacón, M.A. Caminero, E. García-Plaza, P.J. Núñez, Additive manufacturing of PLA structures using fused deposition modelling: Effect of process parameters on mechanical properties and their optimal selection, *Mater. Des.* 124 (2017) 143–157.

[76] L. Sang, S. Han, X. Peng, X. Jian, J. Wang, Development of 3D-printed basalt fiber reinforced thermoplastic honeycombs with enhanced compressive mechanical properties, *Compos. Part A Appl. Sci. Manuf.* 125 (2019) 105518.

[77] L. Tocado, E. Palacios, R. Burriel, Entropy determinations and magnetocaloric parameters in systems with first-order transitions: Study of MnAs, *J. Appl. Phys.* 105 (2009) 093918.

[78] L. Caron, Z.Q. Ou, T.T. Nguyen, D.T. Cam Thanh, O. Tegus, E. Brück, On the determination of the magnetic entropy change in materials with first-order transitions, *J. Magn. Magn. Mater.* 321 (2009) 3559–3566.

[79] B. Kaeswurm, V. Franco, K.P. Skokov, O. Gutfleisch, Assessment of the magnetocaloric effect in La,Pr(Fe,Si) under cycling, *J. Magn. Magn. Mater.* 406 (2016) 259–265.

[80] J.H. Chen, A. Us Saleheen, P.W. Adams, D.P. Young, N. Ali, S. Stadler, On entropy determination from magnetic and calorimetric experiments in conventional giant magnetocaloric materials, *J. Appl. Phys.* 123 (2018) 0–7.

[81] V. Franco, J.S. Blázquez, A. Conde, Field dependence of the magnetocaloric effect in materials with a second order phase transition: A master curve for the magnetic entropy change, *Appl. Phys. Lett.* 89 (2006) 4–7.

[82] V. Franco, J.S. Blázquez, M. Millán, J.M. Borrego, C.F. Conde, A. Conde, The magnetocaloric effect in soft magnetic amorphous alloys, *J. Appl. Phys.* 101 (2007) 09C503.

[83] V. Franco, A. Conde, Scaling laws for the magnetocaloric effect in second order phase transitions: From physics to applications for the characterization of materials, *Int. J. Refrig.* 33 (2010) 465–473.

[84] A. Arrott, J.E. Noakes, Approximate Equation of State For Nickel Near its Critical Temperature, *Phys. Rev. Lett.* 19 (1967) 786–789.

[85] B.K. Banerjee, On a generalised approach to first and second order magnetic transitions, *Phys. Lett.* 12 (1964) 16–17.

[86] V. Franco, A. Conde, V.K. Pecharsky, K.A. Gschneidner, Field dependence of the magnetocaloric effect in Gd and (Er 1−x Dy x)Al 2 : Does a universal curve exist?, *Europhys. Lett.* 79 (2007) 47009.

[87] V. Franco, R. Caballero-Flores, A. Conde, Q.Y. Dong, H.W. Zhang, The influence of a minority magnetic phase on the field dependence of the magnetocaloric effect, *J. Magn. Magn. Mater.* 321 (2009) 1115–1120.

[88] V. Franco, A. Conde, J.M. Romero-Enrique, J.S. Blázquez, A universal curve for the magnetocaloric effect: an analysis based on scaling relations, *J. Phys. Condens. Matter*. 20 (2008) 285207.

[89] J.Y. Law, V. Franco, L.M. Moreno-Ramírez, A. Conde, D.Y.

Karpenkov, I. Radulov, K.P. Skokov, O. Gutfleisch, A quantitative criterion for determining the order of magnetic phase transitions using the magnetocaloric effect, *Nat. Commun.* 9 (2018) 2680.

[90] F. Preisach, Über die magnetische Nachwirkung, *Zeitschrift Für Phys.* 94 (1935) 277–302.

[91] I. Mayergoyz, Mathematical models of hysteresis, *IEEE Trans. Magn.* 22 (1986) 603–608.

[92] C.R. Pike, A.P. Roberts, K.L. Verosub, Characterizing interactions in fine magnetic particle systems using first order reversal curves, *J. Appl. Phys.* 85 (1999) 6660–6667.

[93] M. Winklhofer, G.T. Zimanyi, Extracting the intrinsic switching field distribution in perpendicular media: A comparative analysis, *J. Appl. Phys.* 99 (2006).

[94] T. Schrefl, T. Shoji, M. Winklhofer, H. Oezelt, M. Yano, G. Zimanyi, First order reversal curve studies of permanent magnets, *J. Appl. Phys.* 111 (2012).

[95] L. Spinu, A. Stancu, C. Radu, F. Li, J.B. Wiley, Method for magnetic characterization of nanowire structures, *IEEE Trans. Magn.* 40 (2004) 2116–2118.

[96] J. Garcia, V.M. Prida, V. Vega, W.O. Rosa, R. Caballero-Flores, L. Iglesias, B. Hernando, 2D and 3D ordered arrays of Co magnetic nanowires, *J. Magn. Magn. Mater.* 383 (2015) 88–93.

[97] A.S. Samardak, A. V. Ognev, A.Y. Samardak, E. V. Stebliy, E.B. Modin, L.A. Chebotkevich, S. V. Komogortsev, A. Stancu, E. Panahi-Danaei, A. Fardi-Ilkhichy, F. Nasirpouri, Variation of magnetic anisotropy and temperature-dependent FORC probing of compositionally tuned Co-Ni alloy nanowires, *J. Alloys Compd.* 732 (2018) 683–693.

[98] V. Franco, F. Béron, K.R. Pirota, M. Knobel, M.A. Willard, Characterization of the magnetic interactions of multiphase magnetocaloric materials using first-order reversal curve analysis, *J. Appl. Phys.* 117 (2015) 17C124.

[99] C. Enachescu, R. Tanasa, A. Stancu, F. Varret, J. Linares, E. Codjovi, First-order reversal curves analysis of rate-dependent hysteresis: The example of light-induced thermal hysteresis in a spin-crossover solid, *Phys. Rev. B - Condens. Matter Mater. Phys.* 72 (2005) 1–7.

[100] A. Atitoaie, R. Tanasa, A. Stancu, C. Enachescu, Study of spin crossover nanoparticles thermal hysteresis using FORC diagrams on an Ising-like model, *J. Magn. Magn. Mater.* 368 (2014) 12–18.

[101] V. Franco, T. Gottschall, K.P. Skokov, O. Gutfleisch, First-Order Reversal Curve (FORC) Analysis of Magnetocaloric Heusler-Type Alloys, *IEEE Magn. Lett.* 7 (2016) 1–4.

[102] V. Franco, Temperature-FORC analysis of a magnetocaloric Heusler alloy using a unified driving force approach (T*FORC), *J. Appl. Phys.* 127 (2020).

[103] L.M. Moreno-Ramírez, V. Franco, Setting the Basis for the Interpretation of Temperature First Order Reversal Curve (TFORC) Distributions of Magnetocaloric Materials, *Metals (Basel).* 10 (2020) 1039.

[104] Á. Díaz-García, L.M. Moreno-Ramírez, J.Y. Law, F. Albertini, S. Fabbrici, V. Franco, Characterization of thermal hysteresis in magnetocaloric NiMnIn Heusler alloys by Temperature First Order Reversal Curves (TFORC), *J. Alloys Compd.* 867 (2021) 159184.

[105] M. Varga, L. Galdun, B. Kunca, V. Vega, J. García, V.M. Prida, E.D. Barriga-Castro, C. Luna, P. Diko, K. Saksl, R. Varga, FORC and TFORC analysis of electrodeposited magnetic shape memory nanowires array, *J. Alloys Compd.* 897 (2022) 163211.

[106] P. Gębara, Á. Díaz-García, J.Y. Law, V. Franco, Magnetocaloric response of binary Gd-Pd and ternary Gd-(Mn,Pd) alloys, *J. Magn. Magn. Mater.* 500 (2020) 166175.

[107] Z. Du, H. Yang, Thermodynamic assessment of the Gd–Pd system, *J. Alloys Compd.* 312 (2000) 181–188.

[108] H. Okamoto, Gd-Pd (gadolinium-palladium), *J. Phase Equilibria*. 23

(2002) 283–284.

[109] C. Romero-Muñiz, J.J. Ipus, J.S. Blázquez, V. Franco, A. Conde, Influence of the demagnetizing factor on the magnetocaloric effect: Critical scaling and numerical simulations, *Appl. Phys. Lett.* 104 (2014) 252405.

[110] L.M. Moreno-Ramírez, J.J. Ipus, V. Franco, J.S. Blázquez, A. Conde, Analysis of magnetocaloric effect of ball milled amorphous alloys: Demagnetizing factor and Curie temperature distribution, *J. Alloys Compd.* 622 (2015) 606–609.

[111] Á. Díaz-García, J.Y. Law, P. Gębara, V. Franco, Phase Deconvolution of Multiphasic Materials by the Universal Scaling of the Magnetocaloric Effect, *Jom*. 72 (2020) 2845–2852.

[112] T. Krenke, M. Acet, E.F. Wassermann, X. Moya, L. Mañosa, A. Planes, Ferromagnetism in the austenitic and martensitic states of Ni-Mn-In alloys, *Phys. Rev. B - Condens. Matter Mater. Phys.* 73 (2006) 1–10.

[113] B. Gao, F.X. Hu, J. Shen, J. Wang, J.R. Sun, B.G. Shen, Tuning the magnetic entropy change of Ni50−xMn35+xIn15 alloys by varying the Mn content, *J. Appl. Phys.* 105 (2009) 083902.

[114] J.Y. Law, Á. Díaz-García, L.M. Moreno-Ramírez, V. Franco, A. Conde, A.K. Giri, How concurrent thermomagnetic transitions can affect magnetocaloric effect: The Ni49+xMn36-xIn15 Heusler alloy case, *Acta Mater.* 166 (2019) 459–465.

[115] L.M. Moreno-Ramírez, A. Delgado-Matarín, J.Y. Law, V. Franco, A. Conde, A.K. Giri, Influence of Thermal and Magnetic History on Direct ΔTad Measurements of Ni49+xMn36−xIn15 Heusler Alloys, *Metals (Basel).* 9 (2019) 1144.

[116] V. Franco, A. Conde, M.D. Kuz'Min, J.M. Romero-Enrique, The magnetocaloric effect in materials with a second order phase transition: Are TC and Tpeak necessarily coincident?, *J. Appl. Phys.* 105 (2009) 103–106.

[117] Á. Díaz-García, J.Y. Law, L.M. Moreno-Ramírez, A.K. Giri, V.

Franco, Deconvolution of overlapping first and second order phase transitions in a NiMnIn Heusler alloy using the scaling laws of the magnetocaloric effect, *J. Alloys Compd.* 871 (2021) 159621.

[118] D.A. Gilbert, P.D. Murray, J. De Rojas, R.K. Dumas, J.E. Davies, K. Liu, Reconstructing phase-resolved hysteresis loops from first-order reversal curves, *Sci. Rep.* 11 (2021) 4018.

[119] R. Pike, First-order reversal-curve diagrams and reversible magnetization, *Phys. Rev. B - Condens. Matter Mater. Phys.* 68 (2003) 1–5.

[120] A. Azzalini, The Skew-Normal and Related Families, Cambridge University Press, Cambridge, 2013.

[121] J.S. Smart, Effective Field Theories of Magnetism, Philadelphia, PA: Saunders, 1966.

[122] C. Kittel, Introduction to Solid State Physics, New York: Wiley, 2013.

[123] J. Wang, J. Bai, J. Gu, H. Yan, Y. Zhang, C. Esling, X. Zhao, L. Zuo, Investigation of martensitic transformation behavior in Ni-Mn-In Heusler alloy from a first-principles study, *J. Mater. Sci. Technol.* 58 (2020) 100–106.

[124] I. Dubenko, T. Samanta, A. Kumar Pathak, A. Kazakov, V. Prudnikov, S. Stadler, A. Granovsky, A. Zhukov, N. Ali, Magnetocaloric effect and multifunctional properties of Ni–Mn-based Heusler alloys, *J. Magn. Magn. Mater.* 324 (2012) 3530–3534.

[125] B. Khatri, K. Lappe, D. Noetzel, K. Pursche, T. Hanemann, A 3D-Printable Polymer-Metal Soft-Magnetic Functional Composite—Development and Characterization, *Materials (Basel).* 11 (2018) 189.

[126] I. Antoniac, D. Popescu, A. Zapciu, A. Antoniac, F. Miculescu, H. Moldovan, Magnesium filled polylactic acid (PLA) material for filament based 3D printing, *Materials (Basel).* 12 (2019) 1–13.

[127] A. Qureshi, A. Mergen, M.S. Eroğlu, N.L. Singh, A. Güllüoğlu, Dielectric Properties of Polymer Composites Filled with Different Metals, *J. Macromol. Sci. Part A*. 45 (2008) 462–469.

[128] S. Waheed, J.M. Cabot, P. Smejkal, S. Farajikhah, S. Sayyar, P.C. Innis, S. Beirne, G. Barnsley, T.W. Lewis, M.C. Breadmore, B. Paull, Three-Dimensional Printing of Abrasive, Hard, and Thermally Conductive Synthetic Microdiamond-Polymer Composite Using Low-Cost Fused Deposition Modeling Printer, *ACS Appl. Mater. Interfaces*. 11 (2019) 4353–4363.

[129] S. Fafenrot, N. Grimmelsmann, M. Wortmann, A. Ehrmann, Three-dimensional (3D) printing of polymer-metal hybrid materials by fused deposition modeling, *Materials (Basel).* 10 (2017) 1199.

[130] D. Legland, I. Arganda-Carreras, P. Andrey, MorphoLibJ: integrated library and plugins for mathematical morphology with ImageJ, *Bioinformatics*. 32 (2016) btw413.

[131] J. Schindelin, I. Arganda-Carreras, E. Frise, V. Kaynig, M. Longair, T. Pietzsch, S. Preibisch, C. Rueden, S. Saalfeld, B. Schmid, J.-Y. Tinevez, D.J. White, V. Hartenstein, K. Eliceiri, P. Tomancak, A. Cardona, Fiji: an open-source platform for biological-image analysis, *Nat. Methods*. 9 (2012) 676–682.

[132] A. Hubert, R. Schäfer, Magnetic Domains, Springer Berlin Heidelberg, Berlin, Heidelberg, 1998.

[133] Á. Díaz-García, J.Y. Law, A. Cota, A. Bellido-Correa, J. Ramírez-Rico, R. Schäfer, V. Franco, Novel procedure for laboratory scale production of composite functional filaments for additive manufacturing, *Mater. Today Commun.* 24 (2020) 101049.

[134] P. Pan, B. Zhu, Y. Inoue, Enthalpy relaxation and embrittlement of poly(L-lactide) during physical aging, *Macromolecules*. 40 (2007) 9664–9671.

[135] M. Kwon, S.C. Lee, Y.G. Jeong, Influences of physical aging on enthalpy relaxation behavior, gas permeability, and dynamic mechanical property of polylactide films with various D-isomer contents, *Macromol. Res.* 18 (2010) 346–351.

[136] B. Coppola, N. Cappetti, L. Di Maio, P. Scarfato, L. Incarnato, 3D printing of PLA/clay nanocomposites: Influence of printing temperature on printed samples properties, *Materials (Basel).* 11

(2018) 1–17.

[137] Y. Kong, J.N. Hay, The measurement of the crystallinity of polymers by DSC, *Polymer (Guildf).* 43 (2002) 3873–3878.

[138] Y. Song, Y. Li, W. Song, K. Yee, K.-Y. Lee, V.L. Tagarielli, Measurements of the mechanical response of unidirectional 3D-printed PLA, *Mater. Des.* 123 (2017) 154–164.

[139] F.S. Senatov, K. V. Niaza, M.Y. Zadorozhnyy, A. V. Maksimkin, S.D. Kaloshkin, Y.Z. Estrin, Mechanical properties and shape memory effect of 3D-printed PLA-based porous scaffolds, *J. Mech. Behav. Biomed. Mater.* 57 (2016) 139–148.

[140] A. Karakoç, V.K. Rastogi, T. Isoaho, B. Tardy, J. Paltakari, O.J. Rojas, Comparative Screening of the Structural and Thermomechanical Properties of FDM Filaments Comprising Thermoplastics Loaded with Cellulose, Carbon and Glass Fibers, *Materials (Basel).* 13 (2020) 422.

[141] K.C. Tam, C. Tiu, Modified cox-merz rule for charged polymer systems in solution, *J. Macromol. Sci. Part B.* 33 (1994) 173–184.

[142] A. V. Shenoy, Rheology of Filled Polymer Systems, 1st ed., Springer Netherlands, Dordrecht, 1999.

[143] L.A. Faitel'son, A.I. Alekseenko, Effect of fillers on the viscosity and viscoelasticity of low-density polyethylene melts. Communication 1, *Polym. Mech.* 12 (1976) 430–438.

[144] L.A. Utracki, The Shear and Elongational Flow of Polymer Melts Containing Anisometric Filler Particles; Part I, *Rubber Chem. Technol.* 57 (1984) 507–522.

[145] G. Akay, Flow induced polymer-filler interactions: Bound polymer properties and bound polymer-free polymer phase separation and subsequent phase inversion during mixing, *Polym. Eng. Sci.* 30 (1990) 1361–1372.

[146] X.-L. Xie, Q.-X. Liu, R.K.-Y. Li, X.-P. Zhou, Q.-X. Zhang, Z.-Z. Yu, Y.-W. Mai, Rheological and mechanical properties of PVC/CaCO3 nanocomposites prepared by in situ polymerization, *Polymer (Guildf).*

45 (2004) 6665–6673.

[147] P. Chen, J. Zhang, J. He, Increased flow property of polycarbonate by adding hollow glass beads, *Polym. Eng. Sci.* 45 (2005) 1119–1131.

[148] A. Planes, L. Mañosa, M. Acet, Magnetocaloric effect and its relation to shape-memory properties in ferromagnetic Heusler alloys, *J. Phys. Condens. Matter*. 21 (2009).

[149] F. Hu, B. Shen, J. Sun, Magnetic entropy change in Ni51.5Mn22.7Ga25.8 alloy, *Appl. Phys. Lett.* 76 (2000) 3460–3462.

[150] D. Kikuchi, T. Kanomata, Y. Yamaguchi, H. Nishihara, K. Koyama, K. Watanabe, Magnetic properties of ferromagnetic shape memory $\mathrm{alloys\ Ni2Mn1-Fe\ Ga}$, *J. Alloys Compd.* 383 (2004) 184–188.

[151] J. Duan, P. Huang, H. Zhang, Y. Long, G. Wu, Rongchang Ye, Y. Chang, Farong Wan, Negative and positive magnetocaloric effect in Ni–Fe–Mn–Ga alloy, *J. Magn. Magn. Mater.* 309 (2007) 96–99.

[152] F.-X. Hu, B.-G. Shen, J.-R. Sun, Magnetic entropy change involving martensitic transition in NiMn-based Heusler alloys, *Chinese Phys. B*. 22 (2013) 037505.

[153] T. Gottschall, D. Benke, M. Fries, A. Taubel, I.A. Radulov, K.P. Skokov, O. Gutfleisch, A Matter of Size and Stress: Understanding the First-Order Transition in Materials for Solid-State Refrigeration, *Adv. Funct. Mater.* 27 (2017) 1606735.

[154] R. Das, A. Perumal, A. Srinivasan, Effect of particle size on the magneto-caloric properties of Ni51Mn34In14Si1 alloy, *J. Alloys Compd.* 572 (2013) 192–198.

[155] J. López-García, V. Sánchez-Alarcos, V. Recarte, J.A. Rodríguez-Velamazán, I. Unzueta, J.A. García, F. Plazaola, P. La Roca, J.I. Pérez-Landazábal, Effect of high-energy ball-milling on the magnetostructural properties of a Ni45Co5Mn35Sn15 alloy, *J. Alloys Compd.* 858 (2021) 158350.

[156] W. Wolf, E.M. Mazzer, The influence of particle size and heat treatments on the transformation energies of a gas atomized Cu-Al-Ni-Mn shape memory alloy, *Thermochim. Acta*. 707 (2022) 179107.

[157] G. Cavazzini, F. Cugini, F. Puglielli, S. Fabbrici, D. Delmonte, G. Trevisi, L. Nasi, L. Righi, S. Ener, L. Pfeuffer, D. Koch, O. Gutfleisch, F. Albertini, M. Solzi, Effect of size and disorder on martensitic phase transition and thermal hysteresis in milled Ni-Mn-In-Co microparticles, *J. Alloys Compd.* 906 (2022) 164377.

[158] J. Liu, J.D. Moore, K.P. Skokov, M. Krautz, K. Löwe, A. Barcza, M. Katter, O. Gutfleisch, Exploring La(Fe,Si)13-based magnetic refrigerants towards application, *Scr. Mater.* 67 (2012) 584–589.

[159] M. Krautz, K. Skokov, T. Gottschall, C.S. Teixeira, A. Waske, J. Liu, L. Schultz, O. Gutfleisch, Systematic investigation of Mn substituted La(Fe,Si)13 alloys and their hydrides for room-temperature magnetocaloric application, *J. Alloys Compd.* 598 (2014) 27–32.

[160] J. Lai, H. Sepehri-Amin, X. Tang, J. Li, Y. Matsushita, T. Ohkubo, A.T. Saito, K. Hono, Reduction of hysteresis in (La1-Ce) (Mn Fe11.4-)Si1.6 magnetocaloric compounds for cryogenic magnetic refrigeration, *Acta Mater.* 220 (2021) 117286.

[161] C. Mayer, A. Dubrez, M. Pierronnet, P. Vikner, Towards the large scale production of (La1-zCez)(Fe1-x-yMnySix)13Hn products for room temperature refrigeration, *Phys. Status Solidi Curr. Top. Solid State Phys.* 11 (2014) 1059–1063.

[162] I.A. Radulov, K.P. Skokov, D.Y. Karpenkov, T. Gottschall, O. Gutfleisch, On the preparation of La(Fe,Mn,Si)13H polymer-composites with optimized magnetocaloric properties, *J. Magn. Magn. Mater.* 396 (2015) 228–236.

[163] L.M. Moreno-Ramírez, C. Romero-Muñiz, J.Y. Law, V. Franco, A. Conde, I.A. Radulov, F. Maccari, K.P. Skokov, O. Gutfleisch, The role of Ni in modifying the order of the phase transition of La(Fe,Ni,Si)13, *Acta Mater.* 160 (2018) 137–146.

[164] L.M. Moreno-Ramírez, C. Romero-Muñiz, J.Y. Law, V. Franco, A. Conde, I.A. Radulov, F. Maccari, K.P. Skokov, O. Gutfleisch, Tunable first order transition in La(Fe,Cr,Si)13 compounds: Retaining magnetocaloric response despite a magnetic moment reduction, *Acta Mater.* 175 (2019) 406–414.